Fully Differential Photo-Electron Spectra of Hydrogen and Helium Atoms

Alejandro Zielinski

PhD Thesis
Department of Physics
Ludwig–Maximilians–Universität

Munich, December 2015

Supervisor: Prof. Dr. Armin Scrinzi
Second referee: Prof. Dr. Ulrich Schollwöck
Date of defense: January 26, 2016

Zusammenfassung

Die Messung und Manipulation der Dynamik und Korrelation von Elektronen auf ihren charakteristischen Zeitskalen ist von großer technologischer und wissenschaftlicher Bedeutung. Während moderne Lasertechnologie dies zumindest im Prinzip bereits erlaubt, ist noch viel theoretische Grundlagenarbeit erforderlich. Die hier vorliegende Arbeit konzentriert sich auf den grundlegenden Effekt der Ionisation von Wasserstoff- und Heliumatomen durch starke Laserfelder. Zu diesem Zweck wird die zeitabhängige Schrödingergleichung numerisch gelöst, und Photoelektronspektren werden mit der hoch effizienten tSurff Methode extrahiert.

Die Ein-Teilchen und Zwei-Teilchen Versionen der tSurff Methode wurden neben vielen anderen numerischen Verfahren in einem neuen parallelisierbaren C++ Code implementiert. Die Algorithmen und Methoden werden hier detailliert präsentiert und die numerische Effizienz diskutiert. Für die korrekte und effiziente Implementierung eines gekoppelte-Kanäle-Ansatzes, welcher Einfachionisationsspektren auch von Molekülen berechnen kann, wird eine Mischung aus Längen- und Geschwindigkeitseichung verwendet.

Von uns berechnete numerische Daten dienten als Grundlage für eine detaillierte Studie des sogenannten Attoclock-Experiments mit Wasserstoffatomen. Der dabei auftretende Tunnelionisationsprozess wurde als verzögerungsfrei identifiziert, was verwendet werden kann, um Attoclock-Experimente mit komplizierteren Untersuchungsobjekten als Wasserstoff zu kalibrieren.

Ebenso wurde untersucht, ob Diskrepanzen zwischen theoretischen Vorhersagen und experimentellen Daten für die Breite der Photoelektron-Impulsverteilungen von Helium in elliptisch polarisierten Laserfeldern durch nicht-adiabatische Effekte erklärt werden können. Auf ein damit verwandtes Konsistenzproblem bei der Eichung von Laserintensitäten in Experimenten wird hingewiesen.

Es wird gezeigt, dass die Linienformen von Fano-Resonanzen doppelt angeregter Zustände im Heliumatom, welche in Einfachionisationsspektren - erzeugt durch kurzwellige Laserpulse - zu sehen sind, mittels langwelliger Kontrollfelder manipuliert werden können. Die resultierenden Linienformen werden weiterhin durch die allgemeine Fano-Situation beschrieben, allerdings nun mit einem komplexen (statt reellem) Fano-Parameter, für den ein analytischer Ausdruck gegeben wird. Es wird numerisch gezeigt, dass die ganze Reihe doppelt angeregter Zustände synchronisierte Linienformmodifikationen durchführt, weil die genauen Eigenschaften der involvierten Zustände nicht von Relevanz sind.

Zuletzt werden Doppelionisationsspektren präsentiert, und ein direkt auf experimentelle Daten anwendbares Korrelationsmaß vorgeschlagen. Es werden Ergebnisse aus der Literatur bei kurzen Wellenlängen bestätigt, und winkel- und energieaufgelöste Spektren bei Infrarotwellenlängen für das Heliumatom berechnet. Dabei wird die experimentell beobachtete um viele Größenordnungen erhöhte Doppelionisationseffizienz im Vergleich zu einfachen theoretischen Vorhersagen reproduziert.

Abstract

The ability to probe and manipulate electron dynamics and correlations on their characteristic time scales would open up many technological and scientific possibilities. While modern laser technology already allows to do that in principle, a lot of theoretical ground work is still missing. This thesis focuses on the elementary effect of laser strong field ionization of the two simplest systems: The Hydrogen and Helium atoms. To that end, the time-dependent Schrödinger equation is solved numerically, and photo-electron spectra are extracted using the highly efficient tSurff technique.

We implemented both the one and two particle versions of tSurff together with several other numerical techniques in a new parallelizable C++ code. We provide details on the employed methods and algorithms, and study numerical efficiency properties of various approaches. We propose a description of the electric field interaction in a mixture of length and velocity gauge for the correct and most efficient implementation of a coupled channels approach, which can be used to compute accurate single ionization photo-electron spectra from true multi-electron systems, even molecules.

We provide extensive numerical data for a detailed study of the Hydrogen atom in an Attoclock experimental setup, where it is found that the involved strong field tunnel ionization processes can be considered instantaneous. In particular, there appear no tunneling delays, which can be used as a calibration for experiments with more complicated targets.

Similarly, it is investigated whether discrepancies between theory and experimental data for the longitudinal photo-electron momentum spread, resulting from photo-ionization of Helium in elliptically polarized laser pulses, can be explained by non-adiabatic effects, and a related consistency problem in current laser intensity calibration methods is pointed out.

We further show that Fano resonance line shapes of doubly excited states in the Helium atom, prominently appearing in single ionization spectra generated by short wavelength laser pulses, can be controlled by an external long wavelength streaking field. The resulting line shapes are still characterized by the general Fano situation, but with a complex - rather than real - Fano parameter. We provide a theoretical description of this two color process and prove numerically that the entire doubly excited state series exhibits synchronized line shape modifications as the specifics of the involved states are unimportant.

Finally, we compute fully differential double ionization spectra and suggest a measure of correlation that is directly applicable to experimental data. We confirm literature results at short wavelengths, and achieve to compute five-fold differential double ionization photo-electron spectra at infrared wavelengths from the Helium atom, thereby reproducing a characteristic several orders of magnitude enhancement of double emission due to correlation effects.

List of Publications

The text of this thesis is to large parts based on the following publications:

- [1] C. Hofmann, A. S. Landsman, A. Zielinski, C. Cirelli, T. Zimmermann, A. Scrinzi, and U. Keller. Interpreting electron-momentum distributions and non-adiabaticity in strong-field ionization. *Phys. Rev. A*, 90(4):043406, 2014.

- [2] L. Torlina, F. Morales, J. Kaushal, I. Ivanov, A. Kheifets, A. Zielinski, A. Scrinzi, H. G. Muller, S. Sukiasyan, M. Ivanov, and O. Smirnova. Interpreting Attoclock measurements of tunneling times. *Nat Phys*, 11(6):503508, 2015.

- [3] V. P. Majety, A. Zielinski, and A. Scrinzi. Mixed gauge in strong laser-matter interaction. *Journal of Physics B: Atomic, Molecular and Optical Physics*, 48(2):025601, 2015.

- [4] V. P. Majety, A. Zielinski, and A. Scrinzi. Photo-ionization of few electron systems: a hybrid coupled channels approach. *New Journal of Physics*, 17(6):063002, 2015.

- [5] A. Zielinski, V. P. Majety, S. Nagele, R. Pazourek, J. Burgdöfer, and A. Scrinzi. Anomalous Fano profiles in external fields. *Phys. Rev. Lett*, 115:243001, 2015.

- [6] A. Zielinski, V. P. Majety, and A. Scrinzi. Double ionization spectra of Helium at infrared wavelength. *arXiv*:1511.06655 (accepted for publication in Phys. Rev. A), 2015.

Contents

Chapter 1

Introduction

1.1 Motivation

Technological breakthroughs ahead?

Modern laser sources are able to produce pulses which are so short and so strong, that they can be used to monitor and steer dynamics of electrons on their natural time and length scales. The motion of atoms in molecules, including those during chemical reactions, happens on time scales of tens to hundreds of femtoseconds ($1\,\mathrm{fs} = 10^{-15}\,\mathrm{s}$) [7]. The electronic dynamics in molecular orbitals unfold within single femtoseconds, inner shell atoms evolve on the attosecond ($1\,\mathrm{as} = 10^{-18}\,\mathrm{s}$) time scale [8].

The ability to observe and manipulate electronic motion and correlation on these scales is of high relevance, both from a scientific and a technological point of view. For example, in biological systems information is transported by molecular scale electron dynamics, which may initiate changes in chemical composition and function. Charge and energy transfer in photosynthesis occurs by electronic transitions. Can these processes be manipulated, optimized or adapted for more efficient solar energy generation? Likewise, modern computer components are built up with ever smaller nanometer scale circuitry in which electronic currents are switched on ever faster time scales, but what are the limits for this kind of electronic information processing and how can they be approached? These are just two of many possible questions the research field of attosecond science ultimately wants to answer. The field is however still in its infancy.

Ultrafast measurements

High intensity laser sources with controlled spatial and temporal profiles still pose a certain technological challenge. Only recent advances in laser technology towards so-called lightwave electronics [9] at the beginning of this millennium have opened up the possibility to produce controlled pulses with attosecond resolution of the electric fields. In 2004 the first completely characterized light wave was published [10], and already in the two following years single cycle pulses could be produced both in the short [11] and

long [12] wavelength regimes.

Meanwhile, experimental techniques such as the attosecond streak camera [13], high-harmonic spectroscopy [14], laser induced electron diffraction (LIED) [15], attosecond transient absorption spectroscopy (TAS) [16], or the Attoclock [17] are now able to provide the spatio-temporal resolution needed to initiate, probe or control electron dynamics with such laser pulses.

A couple of examples for recent applications include:

The differences in the electronic responses of chiral pairs of molecules (i.e. non-superimposable mirror images of each other) to external laser fields were time resolved on sub-femtosecond timescales by analyzing the high harmonic emission [18]. The time-dependent bond length of N_2 and O_2 molecules was measured with sub-angstrom and few femtosecond precision using LIED [19]. In TAS experiments on Helium, the time evolution of a correlated two-electron wavepacket could be reconstructed with sub-femtosecond time resolution, using doubly excited states as phase sensitive quantum interferometers [20]. Combining an ionizing short wavelength pulse with a duration of less than 300 as with a waveform controlled near infrared few femtosecond streaking pulse for probing, ultra fast charge migration dynamics after ionization but preceding nuclear rearrangement could be directly measured in the amino acid phenylalanine [21]. Recent Attoclock experiments on Argon were conducted with sub-femtosecond precision, and tried to get a grasp on conceptually and experimentally challenging concepts like ionization release times and tunneling times [22], and in similar experiments on Helium adiabaticity assumptions on tunnel ionization processes were put to the test [23].

Theory follows painstakingly

Likewise, the calibration and interpretation of experimental data heavily relies on the theoretical understanding of the underlying processes. Without the theoretical groundwork, for example for reading diffraction images in LIED [24] or the high harmonic spectroscopy technique [25], these types of experiments would not be of much use. Several simple models explaining a wide range of phenomena have been developed, some of which will be summarized below. However, with growing complexity of the considered systems, and aspiring for also quantitatively correct descriptions, theoretical understanding has increasingly relied on numerical studies with an ever larger demand on computing power. The main goal is to obtain reliable benchmark data which is not obscured by experimental limitations, and to provide access also to non-measurable quantities (like the wavefunction itself) to help with model building.

As of today, the full simulation of more than two electrons in laser matter interaction remains intractable. Most computations were thus performed on effective single-electron systems, low dimensional approximations, or in some other way restricted models, where in all cases results had always to be treated with the caveat of maybe not having captured an essential multi-electron effect. For example, there was a discrepancy between experimental observation and numerical predictions stemming from single-electron models for the peak

emission angle in strong field ionization of CO_2, which could be attributed to exchange interaction, a dynamical effect exclusive to multi-electron systems [26]. And even single-electron systems in high intensity laser fields can pose a significant computational challenge. Theory is lagging behind the experimental achievements since the advent of the research field.

Only in the last ~ 10 years have computations with a full treatment of two electrons become possible, although in some cases only by utilizing supercomputing facilities with power consumptions in the megawatt regime. At short laser wavelengths, where dynamics are initiated by the absorption of only few photons, many numerical *ab initio* studies of two-electron systems could be performed. For example, in 2008 highly accurate triply differential double ionization cross sections in the non-sequential regime were computed for the Helium atom [27]. At longer wavelengths such computations remain daunting. The reason is the inapplicability of perturbative approaches, which only allows for time-dependent non-perturbative methods, combined with a rather unfavorable scaling of the necessary computational power with the wavelength λ and intensity I of the laser pulse. Depending on the observable of interest, it can be as bad as proportional to $\lambda^{13} I^4$, which is detailed below.

In particular double ionization processes are numerically demanding, as both electrons participate in the full range of possible dynamics. There, already at the near visible wavelength of $\lambda \sim 400\,\mathrm{nm}$ full dimensional numerical computations are scarce [28–30]. Progress at longer wavelengths like the experimentally relevant Ti:sapphire wavelength of 780 nm has only been made very recently: In 2013, a numerical study showed that a precisely timed XUV pulse can be used to enhance double emission efficiency from a single cycle 780 nm streaking field of moderate intensity utilizing over 4000 cores of a Supercomputer for each numerical computation [31].

A recently developed technique does however significantly reduce the computational effort of such calculations. By reducing the phase space which needs to be covered by the numeric computation, the tSurff method [32, 33] (see chapter 2) for computing photo-electron spectra allows for studies of photo-emission in single-electron systems with now marginal effort. Also fully simulating two-electron systems is now manageable, even their complete fragmentation at 780 nm.

1.2 Scope of work

In this thesis we employ the tSurff method to examine electron dynamics within elementary systems when subjecting them to a strong external laser field, mainly the Hydrogen and Helium atoms. Analyzing the electronic processes in these atoms is a first step for understanding more complex many-body phenomena. The three body Coulomb problem in particular is of fundamental importance. Understanding the breakup process of Helium initiated by a laser pulse is indispensable for progress towards technologically relevant systems.

The thesis is organized as follows:

We start by summarizing the theoretical description of laser atom interaction, which for the experimentally relevant laser parameters is given by the time-dependent Schrödinger equation (TDSE). We also list a selection of important simplifications and models that have successfully explained a multitude of observed effects.

Efficient numerical treatment

In chapter 2 we then describe in detail the tSurff method for efficient extraction of photo-electron spectra. We estimate the reduction of the computational effort compared to the standard approach and discuss limitations of the method.

In chapter 3 we summarize the numerical techniques which are implemented in our tRecX code and employed for solving the TDSE. In particular we describe the discretization and how absorbing boundary conditions are realized, and also gauge questions [3] are discussed.

Electron tunneling

Chapter 4 is then devoted to single electron systems subjected to long wavelength laser pulses.

Before interacting with the pulse, the electron is bound by the nuclear Coulomb potential. In the presence of the long wavelength pulse, the electric field of the laser and the attractive force of the core together form a potential barrier through which the electron may tunnel. Time resolved measurements allow to study this process in detail, possibly determining exact ionization times and tunneling delays [34]. The Attoclock is one such experimental setup. It uses the rotating electric field vector of a nearly circularly polarized few cycle infrared pulse to extract temporal information of the ionization processes on a sub-cycle scale. Electrons detaching from their parent atom by tunneling through the rotating barrier at different times result in different emission angles, from which the instance of ionization can be reconstructed. It was suggested recently that tunneling delays appear for the Helium atom [35], which we could not verify within a single-electron approximation, as described in Sec. 4.2.3.

We performed numerical studies on the Hydrogen atom to interpret results in Attoclock [17] type experiments, summarized in Sec. 4.1.3. Based on this data, it is shown in Ref. [2] that in the case of Hydrogen vanishing tunneling times can be inferred if the attractive force of the core is correctly included in the reconstruction. The results allow to calibrate the Attoclock for experiments with more complicated targets.

In Sec. 4.2.2 we employ a single-electron model for the Helium atom exposed to elliptically polarized infrared pulses, to study non-adiabatic effects on photo-electron momentum spreads. In Ref. [1] it is shown that discrepancies between adiabatic theories [36, 37] and experimental data [38] can not be resolved when dropping the adiabaticity assumption both for the theory and the experimental laser intensity calibration technique. If however non-adiabaticity is assumed for the theory while the calibration of the experiment is based on adiabatic assumptions, then better agreement is

achieved. This highlights a consistency problem in currently employed calibration techniques, which is not resolved within this thesis.

Anomalous Fano line shapes

Chapter 5 then treats single ionization of multi-electron systems.

We present a coupled channels approach in Sec. 5.1, which is able to tackle true multi-electron systems, including molecules [4]. Thereby the motion of all electrons but one is heavily restricted. We verify the applicability of this ansatz to single emission of two-electron systems by comparing with results employing a fully flexible basis. We can identify physical aspects which require a multi-electron treatment as opposed to features which can already be correctly described within single-electron models. In particular single emission spectra around resonance line shapes of doubly excited states are correctly reproduced only if both electrons have at least a minimum number of dynamical degrees of freedom.

In Sec. 5.2 we demonstrate how an infrared steering field can be used to control such resonance lines in the Helium atom. Manipulation of these so-called Fano profiles [39] has been of recent interest and schemes for control by external fields and interactions were experimentally realized in diverse fields of physics [40]. In standard Fano theory the profiles are described by a real Fano parameter q. In Ref. [5] we show that an external electric control field leads to complex q parameters and thus anomalous Fano profiles. The appearance of complex q has been discussed in several contexts, for example as a consequence of time-reversal symmetry breaking [41] or as a signature of dephasing and decoherence in atoms [42, 43] as well as in quantum dots [44] and microwave cavities [45]. By generalizing Fano theory to include a weak infrared streaking field we provide a full theoretical description whose validity is verified by comparing with extensive *ab initio* numerical studies. We observe synchronized line shape modifications within the entire doubly excited resonance series and identify continuum electron streaking as the primary effect.

Double ionization

Finally, in chapter 6 we study double ionization of the Helium atom by strong external laser pulses and propose a measure of correlation which is directly applicable to experimental data. Helium is the simplest system to exhibit electron correlation effects and several experiments have been conducted in various wavelength regimes.

In 1993 the triply differential cross section for Helium in a short wavelength laser pulse was measured for the first time [46], and many experiments and theoretical studies have followed since then. Of central importance was the measurement of the single to double ionization ratio over a wide range of intensities in the long wavelength regime in 1994 [47]. They found a many orders of magnitude enhancement of double ionization efficiency compared to simple expectations, and linked it to field induced recollisions [48], a process which is not unique to Helium [49]. As of today this so-called non-sequential double ionization is of high interest and various mechanisms have been proposed [50–52],

all based on the recollision scenario.

In our numerical computations [6] we confirm recent literature results [27] at short wavelengths. We further achieve to compute five-fold differential double ionization photoelectron spectra at large wavelengths, and quantitatively reproduce the ratio of single to double ionization yield at low intensities. Due to the scaling of the computational effort mentioned above, this was only made possible due to the high efficiency of the tSurff method.

1.3 Time-dependent Schrödinger equation

This thesis focuses on the interaction of electrons in the atomic shell with a strong external laser field. Independently of all laser parameters and the specific target, the electronic shell will evolve from its initial bound state to a superposition of all its bound states and all possible ionized states (including multiple ionization and ionization with the residual ion in an excited bound state). The accelerated charges will exchange energy with the laser field via a multitude of effects, for example stimulated emission and absorption or Larmor radiation. A comprehensive review can be found in Ref. [8].

The most general description, valid for all experimentally relevant parameters (wavelengths above $\sim 10\,\mathrm{nm}$ at intensities below $\sim 10^{16}\,\mathrm{W/cm^2}$), is given by the time-dependent Schrödinger equation (TDSE). Thereby several well fulfilled approximations are employed.

Low energy approximation: The maximum energies achieved by the target charges considered here are $\lesssim$ keV, which implies that all possible relativistic effects are negligible. This includes corrections to the motion of masses which are below 1%, and also all magnetic fields. Also, the interaction between charges, which in principle requires the quantization of the electromagnetic field, is well described by the effective potential $V(r) \propto r^{-1}$. For the bound states of the field free system this implies omitting effects like spin-orbit coupling or the Lamb shift.

High intensity limit: Concerning the interaction with the photons of the laser field, we note that the coherent radiation of the laser pulses considered here consists of on the order of $n = 10^{15}$ photons. At such high occupation numbers the quantum nature is negligible. In particular, the creation and annihilation operators on the corresponding Fock space approximately commute: $a^\dagger a|n\rangle = n|n\rangle \approx (n+1)|n\rangle = aa^\dagger|n\rangle$. Thus, also the interaction with the laser field can be treated classically. Photons need not be included in the description.

The laser atom interaction does in principle not only change the state of the atom, but also the state of the laser field. On the one hand, the field loses energy to the atom, an effect which is experimentally observable in the form of transient absorption spectra. On the other hand the accelerated charges of the atom radiate and thus input energy into the field, one incarnation of this effect being the experimentally accessible high harmonic generation. Both effects are however small compared to the external laser field, at least if only a single atom is considered. Therefore, the laser field is treated as a fixed entity, and

observables like transient absorption spectra or high harmonic spectra are deduced from the time-dependent electronic configuration.

The TDSE

$$\mathrm{i}\partial_t\psi(t) = H(t)\psi(t) \tag{1.1}$$

with Hamilton operator $H(t)$ is therefore appropriate for the description of the entire laser-atom interaction at experimentally relevant laser parameters. The wavefunction ψ describes the state of the system, where the initial condition $\psi(t_0) = \psi_0$ is typically given by the ground state.

We further employ the dipole approximation, appropriate when spatial dependencies of the field are small on the order of the extension of the target atom. In particular, separating the full electric field $\vec{E}(\vec{r},t)$ into an envelope factor $\vec{E}_0(\vec{r},t)$ and a phase factor $\mathrm{e}^{\mathrm{i}(\vec{k}\vec{r}-\omega t)}$ we can approximate: The variation of $\vec{E}_0(\vec{r},t)$ in space is given by the focal spot size of the laser, which is orders of magnitude larger than the target atom. The spatial dependence of the phase factor is approximately $\mathrm{e}^{\mathrm{i}\vec{k}\vec{r}} \approx 1$ for $|\vec{k}|^{-1} \sim \lambda \gtrsim 10\,\mathrm{nm}$, which is known as the dipole approximation. Thereby we automatically neglect the magnetic field, which is consistent with above low energy approximation.

Finally, the motion of the atomic nucleus is neglected, as already for the lightest possible core of the Hydrogen atom the mass ratio is $\frac{m_{\mathrm{proton}}}{m_e} \sim 10^3$.

Therefore, for a system consisting of N_e electrons in a potential V generated by the nuclei, the Hamiltonian in length gauge is given by

$$H(\vec{r},t) = \sum_{i=1}^{N_e}\Big(-\frac{\Delta_i}{2} + V(\vec{r}_i) + \vec{r}_i\cdot\vec{E}(t)\Big) + \sum_{i>j}\frac{1}{|\vec{r}_i-\vec{r}_j|} \tag{1.2}$$

with the electric field $\vec{E}(t)$ of the external laser pulse. Any other gauge is equally appropriate, and for numerical reasons we will indeed prefer velocity gauge, which will be discussed below. For an atomic target, $V(\vec{r}_i) \propto |\vec{r}_i|^{-1}$. Here and throughout the thesis atomic units $\hbar = e^2 = m_e = 4\pi\epsilon_0 \equiv 1$ are used unless indicated otherwise, see appendix 8.3 for some conversions.

Knowledge of the wavefunction is required for the computation of any observable. For example, the computation of photo-electron spectra $P(k_1k_2...,C)$ with photo-electron momenta $k_1, k_2\ldots$ and residual ionic bound state configuration C require the transition amplitudes of the initial state ψ_0 into the scattering states $\chi_{k_1k_2...,C}$ with respective outgoing boundary conditions:

$$P(k_1k_2...,C) = |\langle\chi_{k_1k_2...,C}|\lim_{t\to\infty}\psi(t)\rangle|^2 \tag{1.3}$$

with

$$|\psi(t)\rangle = U(t,t_0)|\psi_0\rangle \tag{1.4}$$

where

$$U(t,t_0) = \mathbb{T}\left[\mathrm{e}^{-\mathrm{i}\int_{t_0}^{t}\mathrm{d}\tau\,H(\tau)}\right] \tag{1.5}$$

is the time evolution operator ($\mathbb{T}$ is the time-ordering operator). The computation of observables like transient absorption spectra or high harmonic spectra requires evaluation of time-dependent matrix elements like $\langle\psi(t)|\vec{r}|\psi(t)\rangle$ or $\langle\psi(t)|\nabla|\psi(t)\rangle$.

Solving the TDSE without further approximations is only possible using numerical techniques and may represent a formidable task, which is the main topic of this thesis. First we introduce some simple but very useful models.

1.4 Approximations and models

Several additional approximations can be employed, whose scope of applicability depend on the physical regime (determined by the laser parameters and the target atom). Stripping away effects may result in simple but still accurate models, which can provide deep understanding of the underlying physics. Such models do however need accurate benchmark data for comparison. These can come both from experiment and numerical solutions of the TDSE. Where accessible, numerical data is typically preferable, as it is not plagued by the many possible experimental disturbances and error sources, and also provides access to the wavefunction itself.

1.4.1 Perturbation theory

For laser parameters where the target atom mainly remains in its initial state, we may successfully apply perturbation theory. This is in general the case for laser pulses with wavelengths in the ultra violet (UV) regime and below (and not excessively high intensities $\lesssim 10^{15}\,\mathrm{W/cm^2}$). The time evolution by the full Hamiltonian $H(t)$ is thereby approximated by the time evolution with the field free Hamiltonian H_0 and a perturbative correction $H_L(t) = \vec{r}\cdot\vec{E}(t)$ for the laser field. The resulting perturbative series, also called Dyson series, is given by:

$$\begin{aligned} U(t,t_0) \;\approx\; & U_0(t,t_0) \\ & -\mathrm{i}\int_{t_0}^{t}\mathrm{d}t'\,U_0(t,t')H_L(t')U_0(t',t_0) \\ & -\int_{t_0}^{t}\mathrm{d}t'\int_{t_0}^{t'}\mathrm{d}t''\,U_0(t,t')H_L(t')U_0(t',t'')H_L(t'')U_0(t'',t_0) \\ & +\mathcal{O}(H_L^3) \end{aligned} \tag{1.6}$$

with $U_0(t,t_0) = \mathrm{e}^{-\mathrm{i}(t-t_0)H_0}$. In so-called n-th order perturbation theory the series is truncated after the n-th correction term. In first order perturbation theory the transition amplitude for a single-electron system hit by a linearly polarized pulse (starting after

$t = t_0$) in $\hat{e}_1$-direction $\vec{E}(t) = \mathcal{E}(t)\hat{e}_1$ is thus given by

$$\begin{aligned}\langle\chi_k| \lim_{t\to\infty} U(t,t_0)|\psi_0\rangle &\approx \lim_{t\to\infty}\langle\chi_k| \int_{t_0}^{t} \mathrm{d}t'\, U_0(t,t')H_L(t')U_0(t',t_0)|\psi_0\rangle \\ &= \langle\chi_k|\vec{r}\cdot\hat{e}_1|\psi_0\rangle \int_{-\infty}^{\infty} \mathrm{d}t'\, \mathcal{E}(t')\mathrm{e}^{-\mathrm{i}(E_0-E_k)t'} \qquad (1.7)\end{aligned}$$

where E_0 and E_k are the energies of the initial state ψ_0 and the scattering state χ_k respectively.

If the electric field of the laser pulse has the carrier frequency ω and a Gaussian envelope of width α, i.e. $\mathcal{E}(t) \propto \mathcal{E}_0\mathrm{e}^{-t^2/\alpha}\mathrm{e}^{-\mathrm{i}\omega t}$, then

$$\int \mathrm{d}t'\, \mathcal{E}(t')\mathrm{e}^{-\mathrm{i}(E_0-E_k)t'} = \mathcal{E}_0\mathrm{e}^{-\alpha(E_0-E_k+\omega)^2/4}\sqrt{\alpha\pi} \overset{\alpha\to\infty}{\longrightarrow} \mathcal{E}_0\delta(E_k - E_0 - \omega) \qquad (1.8)$$

implying a peak of width $\propto 1/\alpha$ and height $\propto \mathcal{E}_0^2$ at $E_k = E_0 + \omega$. Similarly, the second order correction gives a peak of same width but height $\propto \mathcal{E}_0^4$ at $E_k = E_0 + 2\omega$, and the n-th order correction produces a peak of height $\propto \mathcal{E}_0^{2n}$ at $E_k = E_0 + n\omega$.

If some n-th peak is the first that actually lies above the ionization threshold, then this process is called multi-photon ionization. The higher peaks ($n+1$, $n+2$ ...) are then called above threshold ionization (ATI) peaks.

1.4.1.1 A comment on photons

Although our description of the physics explicitly neglects the quantization of the electromagnetic field, and therefore does not contain photons, we do see peaks separated by the photon energy ω. The reason was shown above: The perturbative contribution enters via the Fourier transform of the electric field, which has a peak at the carrier frequency ω. While the accuracy of the solely perturbative treatment depends on the laser parameters, there will always be signatures of photon peaks as long as the carrier frequency is defined sharp enough in the pulse, which depends on the width of the envelope function.

Whenever photons are mentioned in this thesis, it is meant in this sense.

Also other experimental observations like the photo-electric effect are perfectly reproduced within our description: For the Hydrogen atom, below the frequency threshold $\omega_{\mathrm{crit}} = |E_0| = 0.5\,\mathrm{a.u.}$ (groundstate energy) no single-photon ionization occurs, and the kinetic energy of photo-electrons above that threshold increases linearly with the photon energy ω. This effect does not require any form of quantization of the laser field, although that is often falsely conjectured. Figure 1.1 shows the ionization yield and the mean kinetic energy of liberated electrons as a function of the carrier frequency ω of the laser field. It can be seen that at $\omega = \omega_{\mathrm{crit}}$ the ionization efficiency increases dramatically. For $\omega < \omega_{\mathrm{crit}}$ only two (or more) photon ionization is possible, which has significantly lower efficiency. At frequencies which resonantly connect the groundstate with an excited state $\omega_n = E_n - E_0 = (-\frac{1}{2n^2} + \frac{1}{2})$ the ionization probability is slightly increased.

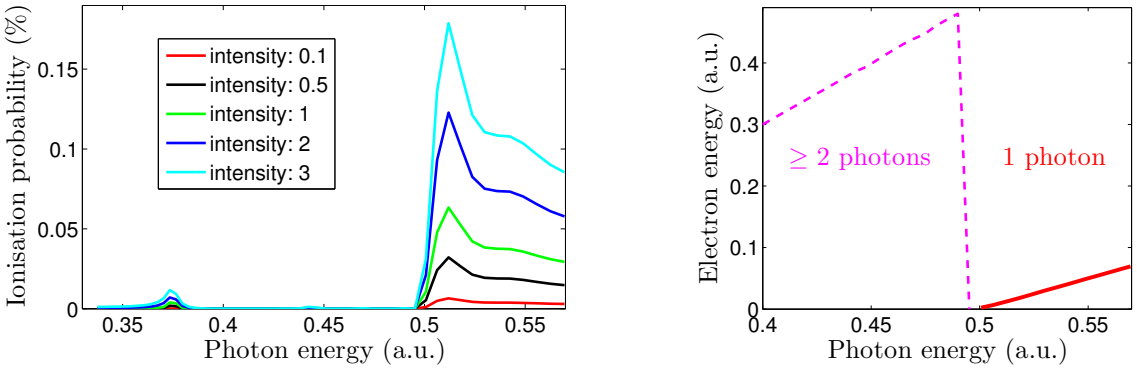

Figure 1.1: Left: Numerically computed total ionization probability (yield) of Hydrogen as a function of the photon energy $\hbar\omega$ for various intensities in units of $10^{12}\,\mathrm{W/cm^2}$. Apart from the cutoff at $\omega = \omega_{\mathrm{crit}} = \frac{1}{2}\,\mathrm{a.u.}$ also resonant peaks at $\omega_2 = \frac{3}{8}\,\mathrm{a.u.} = 0.375\,\mathrm{a.u.}$ and $\omega_3 = \frac{4}{9}\,\mathrm{a.u.} \approx 0.44\,\mathrm{a.u.}$ are discernible. Right: The mean kinetic energy of photo-electrons is independent of the laser intensity but dependent on the photon energy. Below ω_{crit} it is dominated by photo-electrons having absorbed two (or even more) photons (dashed magenta). Only for photon energies above ω_{crit} one-photon ionization with large experimental signals is possible, and the mean kinetic energy then increases linearly with ω (solid red). Such results are often used to falsely conclude the existence of photons.

1.4.1.2 A comment on pulse shapes (envelopes)

As can be seen in Eq. (1.8), perturbation theory predicts photo-electron peaks at positions $E_0 + n\omega$, where the shape of these peaks is determined by the spectral content of the pulse, i.e. its Fourier transform. In numerical computations often experimentally unrealistic pulse shapes are used, in particular the $\cos^2$ envelope has been popular. These kind of non-smooth pulse shapes have strong sidebands in their spectral decomposition which lead to spurious artificial structures in the results, see for example Ref. [53].

We show how the usage of a $\cos^8$ pulse envelope, which has a narrower spectral width, removes such artifacts in the context of tunnel ionization in elliptically polarized fields (Sec. 4.2.3), and in the context of double ionization by ultra violet laser pulses (Sec. 6.3).

In the appendix 8.4 we summarize the pulse shapes predominantly used in this thesis.

1.4.2 ADK formula

The above perturbative treatment of the laser field applies when its frequency is so large, that the electrons have no time to adjust to an instantaneous field strength. In the other limit, where the electrons can follow the field strength evolution adiabatically, a formula developed by Ammosov, Delone and Krainov (ADK) [36] can be useful. The relevant property is that the static field ionization rate for an atom in an electric field strength $\mathcal{E}$

has an exponential dependence of the form

$$\Gamma \sim \mathrm{e}^{-I_p^{3/2}/\mathcal{E}}, \tag{1.9}$$

where I_p is the ionization potential. This stands in stark contrast to the power law behavior in the perturbative regime.

In our context this formula is valid when the laser field strength $\mathcal{E}(t)$ varies only slowly, which is the case for long laser wavelengths. In this quasi-static situation the dominant contribution to ionization comes from times of maximal field strength due to the strong exponential dependence.

1.4.3 Strong Field Approximation and Keldysh parameter

Another widely used model is the Strong Field Approximation (SFA), first described in Ref. [54], where the influence of the Coulomb potential is neglected for the electron continuum states. The time evolution of an ionized electron is thus solely driven by the external laser field, which allows for a closed analytical description using Volkov states (see Sec. 2.1.2.2). This is justified if the force an electron experiences from the electric field is much larger than the force exerted by the nucleus, which is of course never satisfied at short distances. Far away from the nucleus, and in particular at large laser intensities and long wavelengths, this is however a good approximation.

An important conclusion of this work was the separation of the dynamics into two qualitatively different regimes: The tunneling regime and the multi-photon regime. The Keldysh parameter was introduced as the ratio of an equivalent classical time of flight τ_T through the potential barrier build up by the Coulomb potential and the electric field together (compare Fig. 1.2 a), and the time in which the electric field changes, i.e. the period of laser field oscillation τ_L: $\gamma := 2\frac{\tau_T}{\tau_L}$.

At short laser wavelengths (implying small laser periods) and small intensities (thus large τ_T), with $\gamma \gg 1$, the perturbative treatment (section 1.4.1) is accurate. Photo electron probability peaks of size $\propto I^n$ appear (I being the peak intensity of the laser pulse) separated by the photon energy $\hbar\omega$, which is why this regime is called the multi-photon regime. At large wavelengths and high intensities the Keldysh parameter is small $\gamma \ll 1$ and the exponential dependence of tunnel ionization, Eq. (1.9), is recovered.

Introducing the cycle averaged kinetic energy of a charge in the laser field (without any other potential)

$$U_p := \frac{I}{4\omega_L^2}, \tag{1.10}$$

which is also called the ponderomotive energy, the Keldysh parameter may also be written as

$$\gamma = \sqrt{\frac{I_p}{2U_p}}. \tag{1.11}$$

Note that many experiments are performed in the intermediate regime $\gamma \approx 1$, where ionization is a combination of these mechanisms [55].

1.4.4 Three Step Model

In the tunneling regime $\gamma \ll 1$, photo-ionization and also high harmonic generation can be explained by the so called three-step-model [48, 56], which is depicted in Fig. 1.2. In the first step, the electron is liberated from the atom. In the second step, the electron is accelerated by the laser field such that it may recollide in the third step with its parent ion. The recollision may trigger a multitude of effects, from recombination (inducing high harmonic generation) over self-interference to double ionization.

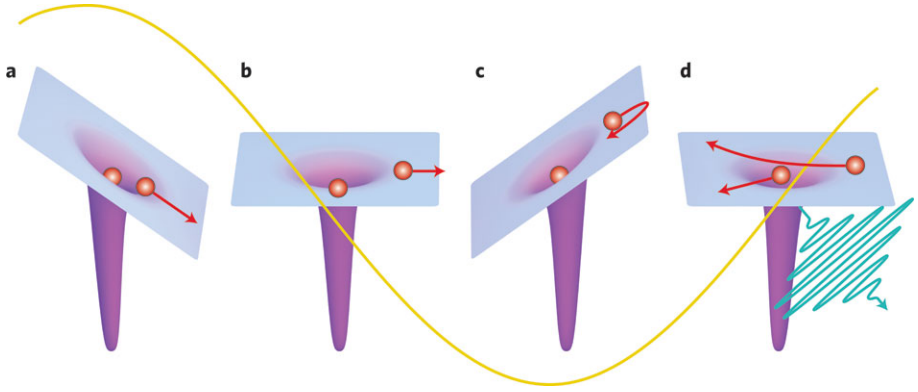

Figure 1.2: Schematic description of the three step model. The yellow curve illustrates the driving laser electric field. In the first step the electron is emitted at the peak of the electric field (a) and driven away from the parent system (b). When the electric field reverses, the ionized electron is redirected (c, second step) and recollides in the third step with the parent system thereby possibly recombining (emitting radiation) or further ionizing the system (d). Figure reproduced from Ref. [57].

A multitude of published more sophisticated models build up on this picture. For example, in Ref. [58] a full quantal recollision model is used and Ref. [59] employs electron impact cross sections for the third step. In Ref. [50] a classical ensemble method is used for step two, while Ref. [51] uses a semi-analytic version of SFA. Low dimensional models are developed for example in Refs. [60, 61]. Refinements in all steps lead to more and more accurate descriptions and help identify the critical ingredients for a quantitatively correct modeling of the ionization process.

1.4.5 Classical estimates

Using classical mechanics one can estimate energy thresholds for the three-step-model. Employing the SFA for steps b) and c) of Fig. 1.2 one can compute the maximum kinetic energy an electron can obtain without recollision, which is twice the ponderomotive energy: $2\,U_p$. Similarly, the maximum kinetic energy at the instant of recollision is found to be $\approx 3.17\,U_p$, while after a fully elastic recollision process energies may reach up to $\approx 10\,U_p$

at the end of the laser pulse. The $2\,U_p$ and $10\,U_p$ thresholds can be observed in single ionization photo-electron spectra, as will be shown in Sec. 4.1.1. The $3.17\,U_p$ can be observed as a cutoff in high harmonic spectra at $3.17\,U_p + I_p$, which are therefore associated with recombination processes.

Another useful quantity is the excursion amplitude of a free electron in the field, also called quiver radius:

$$r_q = \frac{\mathcal{E}_0}{\omega^2} \tag{1.12}$$

with peak electric field $\mathcal{E}_0$ and laser frequency ω.

Chapter 2

Computing photo-electron spectra - the tSurff method

Photo-electron spectra are among the most directly accessible observables in laser-matter interaction experiments. Their full non-perturbative computation is only possible employing numerical techniques and may represent a formidable computational task, as described below. In this section we describe the tSurff method, which allows for a drastic reduction of the computational effort.

2.1 Single-electron systems

We start by summarizing the single particle version, originally described in Ref. [32]. It has been applied to Hydrogen [2], a single-electron Helium model [1], as well as the dissociative ionization of H_2^+ [62]. In Ref. [4] the method was extended to single ionization of atoms and molecules in a coupled channels formalism and used to study CO_2 [26]. The method has also been adapted for usage within the time-dependent configuration-interaction singles scheme [63].

2.1.1 The straight forward approach and its weaknesses

For single-electron systems the Hamiltonian in velocity gauge is

$$H(t) = -\frac{\Delta}{2} - \mathrm{i}\vec{A}(t)\vec{\nabla} + V, \tag{2.1}$$

where in case of the Hydrogen atom $V(\vec{r}) = -1/r$ (with $r := |\vec{r}|$). The photo-electron spectrum is given by

$$P(\vec{k}) = |\langle\chi_{\vec{k}}| \lim_{t\to\infty} \psi(t)\rangle|^2, \tag{2.2}$$

where $\chi_{\vec{k}}$ are the field free scattering states with outgoing momenta $\vec{k}$: $H\chi_{\vec{k}} = \frac{k^2}{2}\chi_{\vec{k}}$. The numeric solution of Eq. (2.2) implies the propagation of the initial state $\psi_0 = \psi(t_0)$

before the start of the pulse until some time t_f after the end of the pulse, and subsequent projection onto the scattering states $\chi_{\vec{k}}$.

This approach can become numerically challenging. The reason is that ψ may extend to very large distances during the interaction with the laser pulse, which necessitates numerical solution in huge phase space volumes. Consider a laser pulse with wavelength $\lambda \equiv c \cdot \tau$, peak intensity I and total pulse length $n \cdot \tau$ (we call n the number of cycles in the pulse). The maximum momentum $p_{\max}$ electrons can achieve in the ionization process is dominated by the ponderomotive energy in the case of the computationally demanding long wavelength regime:

$$p_{\max} = \sqrt{2E_{\max}} \approx \sqrt{2 \cdot 10\, U_p} \propto \lambda\sqrt{I}, \tag{2.3}$$

see Eq. (1.10). The maximum distance an electron covers during the laser pulse is $r_{\max} \sim n\tau \cdot p_{\max}$. Thus, the radial part of the phase space volume V_r can be estimated to

$$V_r \sim r_{\max} \cdot p_{\max} \propto n\lambda^3 I. \tag{2.4}$$

Also the phase space volumes of the other spatial dimensions depend on the laser parameters, see the estimate in Sec. 3.1.1.1. In spherical coordinates (r, θ, φ) both V_θ and V_φ grow as $\propto\lambda^3 I$, although in case of linearly polarization one factor $\lambda^3 I$ is canceled due to symmetry.

Thus the computational effort for electron spectra from an arbitrarily polarized laser pulse grows as

$$V_r \cdot V_\theta \cdot V_\varphi \cdot n\tau \propto n\lambda^3 I \cdot \lambda^3 I \cdot \lambda^3 I \cdot n\lambda = n^2\lambda^{10} I^3 \tag{2.5}$$

which is a generous estimate as it ignores the effects on the time step size. The tSurff method allows to reduce this scaling by a factor of approximately $10n$ (see Sec. 2.1.3 for details), which for experimentally often relevant long pulses ($n \gtrsim 100$) significantly simplifies the problem.

Furthermore, except for the atomic case of a single centered potential $V(\vec{r})$, the scattering solutions may not be known analytically. The numerical computation of the scattering solutions may thus represent a challenge in itself. Using tSurff, their form is only required at large distances, where controllable approximations can be employed.

2.1.2 tSurff for a single particle

2.1.2.1 Idea

There are two central ideas for the tSurff method. We start from the simple fact that the wavefunction after the pulse has split into bound and scattering parts

$$\psi = \psi_{\mathrm{b}} + \psi_{\mathrm{s}}. \tag{2.6}$$

The first main idea is that this distinction can be done also in coordinate space. Explicitly, for large times T long after the pulse, the scattering parts of the wavefunction

will have approximately (low energy components need arbitrarily long times) zero mass near the core as they will have flown out to large distances. The bound parts on the other hand will have approximately (bound states have tails extending to infinity) zero mass at large distances. Choosing some large radius R_c we can therefore write

$$\psi_\mathrm{b}(\vec{r}, T) \approx 0 \qquad \text{for } r > R_c \tag{2.7}$$
$$\psi_\mathrm{s}(\vec{r}, T) \approx 0 \qquad \text{for } r < R_c. \tag{2.8}$$

This is good because it allows to project onto the scattering solutions of the Hamiltonian much easier, since we need to know their shape only for $r > R_c$.

Now the second main idea: If R_c is also large enough that for $r > R_c$ the Hamiltonian is (approximately) analytically solvable, then we can restrict the numerical approach to the region $r < R_c$ and use the analytic solution outside. This is good because we may reduce the phase space that we need to represent numerically by absorbing the wavefunction for $r > R_c$, saving computational resources.

2.1.2.2 Computing the scattering amplitude

The momentum spectrum P is given by

$$P(\vec{k}) = |b(\vec{k})|^2 \tag{2.9}$$

where $b(\vec{k})$ are the scattering amplitudes, i.e. the projections of the wavefunction on the scattering solutions at time t_f after the end of the pulse

$$b(\vec{k}) = \langle \chi_{\vec{k}} | \psi(t_f) \rangle. \tag{2.10}$$

By the first main idea from above we can approximate this as

$$b(\vec{k}) \approx \langle \chi_{\vec{k}} | \mathbb{1}_{r>R_c} | \psi(T) \rangle, \tag{2.11}$$

since we assume that for $t = T$ the scattering components of ψ have accumulated in the region $r > R_c$. $\mathbb{1}_{r>R_c}$ is the characteristic function of the domain $[R_c, \infty)$, i.e.

$$\mathbb{1}_{r>R_c}(r) = \begin{cases} 1 & r \geq R_c \\ 0 & r < R_c. \end{cases} \tag{2.12}$$

Concerning the assumption for the second main idea: Assume that for $r > R_c$ the potential $V(\vec{r})$ vanishes, i.e.

$$V(\vec{r}) = 0 \qquad \text{for} \qquad r > R_c. \tag{2.13}$$

Then the scattering solutions $\chi_{\vec{k}}$ in $r > R_c$ are given by plane waves $\chi_{\vec{k}}(\vec{r}) = (2\pi)^{-\frac{3}{2}} \mathrm{e}^{\mathrm{i}\vec{k}\vec{r}}$ for which we know the time evolution. It is determined by the Volkov Hamiltonian

$$H_V = -\frac{\Delta}{2} - \mathrm{i}\vec{A}(t)\vec{\nabla} \tag{2.14}$$

with analytically known solutions

$$\chi_{\vec{k}}(\vec{r},t) = (2\pi)^{-\frac{3}{2}} \mathrm{e}^{\mathrm{i}\vec{k}\vec{r}} \mathrm{e}^{-\mathrm{i}\Phi(\vec{k},t)} \qquad \Phi(\vec{k},t) = \int^t \mathrm{d}\tilde{t}\,\big(\frac{\vec{k}^2}{2} + \vec{k}\vec{A}(\tilde{t})\big). \tag{2.15}$$

If equation (2.13) does not hold exactly, an additional approximation is required, see next section.

Now comes the key mathematical manipulation which unfolds the might of tSurff: Transform the volume integral in Eq. (2.11) into a time integral and a surface integral.

$$\begin{aligned} b(\vec{k}) &\approx \langle\chi_{\vec{k}}|\mathbb{1}_{r>R_c}|\psi(T)\rangle \\ &= \langle\chi_{\vec{k}}(T)|\mathbb{1}_{r>R_c}|\psi(T)\rangle \qquad \text{(up to an irrelevant phase factor)} \\ &= \int_{t_0}^{T} \mathrm{d}t\,\partial_t \langle\chi_{\vec{k}}(t)|\mathbb{1}_{r>R_c}|\psi(t)\rangle \\ &= \mathrm{i}\int_{t_0}^{T} \mathrm{d}t\,\langle\chi_{\vec{k}}(t)|\Big[H_V(t),\mathbb{1}_{r>R_c}\Big]|\psi(t)\rangle. \end{aligned} \tag{2.16}$$

We used that $H_V(t) = H(t)$ for $r \geq R_c$ due to assumption 2.13. The commutator gives Dirac-deltas at the surface, which is most easily seen in spherical coordinates (r,φ,η) with $\eta := \cos\theta$

$$\begin{aligned} &\Big[-\frac{\Delta}{2} - \mathrm{i}\vec{A}\vec{\nabla}, \mathbb{1}_{r>R_c}\Big](r,\varphi,\eta) = \\ &= -\frac{1}{2}\frac{1}{r^2}\partial_r r^2 \delta(r-R_c) - \frac{1}{2}\delta(r-R_c)\partial_r \\ &\quad -\mathrm{i}\Big(A_x\sqrt{1-\eta^2}\cos\varphi + A_y\sqrt{1-\eta^2}\sin\varphi + A_z\eta\Big)\delta(r-R_c). \end{aligned} \tag{2.17}$$

The evaluation of expression (2.16) therefore requires knowledge of ψ and its derivative at the surface $r = R_c$ for all times $t \in [t_0, T]$. The intuitive interpretation is that one sums up (integral over time) the flux through the surface at R_c to find the total mass getting ionized with specific final momentum $\vec{k}$, which is the motivation for the name tSurff: time-dependent surface flux.

In appendix 8.5.1 we explicitly compute the integrand of Eq. (2.16) for our specific choice of basis, which is described in chapter 3.

2.1.3 Gain

For the computation of spectra, ψ only needs to be known at the surface $r = R_c$. If an absorbing boundary condition beyond R_c does not modify the surface values, the tSurff method reduced the maximum extend of the phase space volume where a numerical solution needs to be computed from the maximum extension $r_{max} \propto n\tau p_{\max}$ to R_c, which for large wavelengths is determined by the quiver amplitude r_q of electrons in the field. Assuming, that the maximum momentum $p_{\max}$ is determined by the electron's maximum kinetic

energy of $10\,U_p$, then the radial extensions of the computation box is reduced by a factor of

$$\frac{r_{\max}}{r_q} \approx \frac{n\tau\sqrt{2\cdot 10U_p}}{r_q} \approx 10n \tag{2.18}$$

which was already advertised above. The factor 10 is the ratio for a single cycle pulse, the scaling with n is due to the pulse length independence of the quiver radius r_q. In section 4.1.1 we demonstrate for an exemplary pulse that one can indeed choose $R_c \approx r_q$.

2.1.4 Limitations

There are several limitations of the method.

2.1.4.1 Low energy photo-electrons

First, contributions to the photo-electron spectrum are only taken into account from those parts of the wavefunction which passed through the tSurff surface at radius R_c until time T. In order to capture low energetic contributions correctly, time propagation must continue until long after the end of the pulse.

2.1.4.2 Neglecting long range tails

Second, for non-short-range potentials we do not have access to the time-dependent continuum functions in the external laser field. A controllable approximation for such potentials is by explicitly truncating the long range behavior:

$$V(\vec{r}) \to f_{a,b}(r)V(\vec{r}) \tag{2.19}$$

with

$$f_{a,b}(r) := \begin{cases} 1 & r < a \\ \frac{2}{(b-a)^3}\big(r-b\big)^2\Big(r-\frac{3a-b}{2}\Big) & a < r < b \\ 0 & b < r \end{cases} \tag{2.20}$$

where $b \leq R_c$, and the expression for $a < r < b$ is a third order polynomial with continuous derivatives at $r = a$ and $r = b$. Then, the time-dependent scattering states are again given by Volkov waves (2.15) for $r > R_c$. The missing long range behavior obviously modifies ionized electron trajectories. Often more important, the potential does not support an arbitrary number of Rydberg states which may be relevant for processes involving near threshold photo-electrons or resonances involving highly excited states. At the moment, these errors can only be controlled by increasing the truncation radius R_c. It may also be possible to introduce corrections to the used scattering wavefunction $\chi_{\vec{k}}(\vec{r},t)$ and thereby dispose of the truncation completely (e.g. by use of Eikonal Volkov waves [64]), which is the goal for future works.

The upper boundary $b \leq R_c$ of the truncation interval should usually be chosen as

$$b = R_c \tag{2.21}$$

because this is the least intrusive choice. Any $b < R_c$ implies an unnecessary modification of the Coulomb potential. An analogous general statement for a can not be given. In Sec. 4.1.1 we demonstrate explicitly the most efficient choice for $[a, b]$ in case of a long wavelength linearly polarized laser pulse.

2.1.4.3 Absorption of rescattering paths

Third, the absorption of the wavefunction beyond the tSurff radius R_c may modify the physical processes if dynamics would move mass back to $r < R_c$. In particular, absorption could suppress possible recollisions of field ionized electrons with the ion, implying that all rescattering dynamics must unfold before absorption, which sets a lower limit as to how close to the nucleus the start of absorption may be pushed. This is roughly given by the quiver radius r_q, as electrons further away can not come back close enough to the core potential for recollision. Details on our choice of absorber are given in Sec. 3.2, and in Sec. 4.1.1 we describe convergence behavior with the starting point of absorption explicitly.

2.1.4.4 Rydberg states reaching into R_c

Fourth, highly excited bound states of large extent with non-negligible probability densities at the tSurff radius R_c violate the assertion that arbitrarily long after the pulse the wavefunction components beyond R_c belong to ionized parts. The tails of these states lead to artificial oscillating contributions in the photo-electron spectra. The detailed nature of these artifacts and how they can be removed is elaborated in this section.

Consider the Hydrogen atom, with its bound states $\psi_{nlm}(\vec{r}) \propto R_{nl}(r)Y_l^m(\Omega)$, where $R_{nl}(r) \propto \mathrm{e}^{-r/n} r^l L_{n-l-1}^{2l+1}(r/n)$. Assume that a Rydberg state on the n-th shell with maximal probability density at large distances (i.e. with $l = n-1$) is populated at some time T_0 after the end of the pulse. Then its contribution to the spectrum is

$$b_n(k, T_0) \;=\; \langle \chi_{\vec{k}} | \mathbb{1}_{r>R_c} | \psi_{n,n-1,0} \rangle. \tag{2.22}$$

Expanding the plane wave $\chi_{\vec{k}}$ into spherical harmonics and inserting the asymptotic form of the appearing spherical Bessel functions $j_{n-1}(kr) \overset{kr\gg 1}{\sim} \frac{\cos(kr)}{kr}$ we get

$$b_n(k, T_0) \;\sim\; \int_{R_c}^{\infty} r^2 \mathrm{d}r \, \frac{\cos(kr)}{kr} \mathrm{e}^{-r/n} r^{n-1} \tag{2.23}$$

$$\sim\; \frac{\sin(kR_c)}{k^2} + \mathcal{O}\left(n^{-1}, k^{-3}\right). \tag{2.24}$$

The contribution from the Rydberg state $\psi_{n,n-1,0}$ results in oscillatory artifacts with n-independent scaling (but n-dependent prefactor) in the photo-electron spectrum

$$P_n(k, T_0) \propto \frac{\sin^2(kR_c)}{k^4} \tag{2.25}$$

as shown in figure 2.1 for a pulse with frequency tuned to efficiently excite Rydberg states.

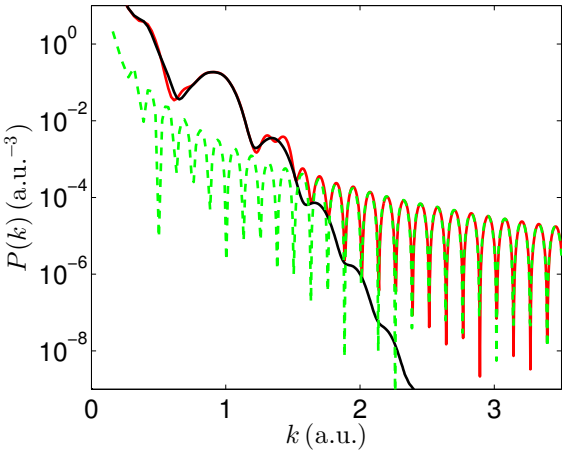

Figure 2.1: Red: Numerically computed angle integrated spectrum $P(k)$ of Hydrogen from an $\hbar\omega = 0.5$ a.u. pulse without treatment of Rydberg state artifacts. Black: Correct spectrum $P(k)$. Green: $P_n(k, T_0)$, Eq. (2.25). The coinciding decay $\propto k^{-4}$ and oscillating behavior shows that the artificial contributions (dominating at large momenta: $k \gtrsim 1.5$ a.u. at the given parameters) do indeed originate in Rydberg states.

These artifacts do not vanish with longer propagation time, as they only accumulate phases:

$$b_n(k, T) = b_n(k, T_0)\mathrm{e}^{\mathrm{i}(E_n - E_k)(T - T_0)}. \tag{2.26}$$

Increasing R_c does reduce these errors, but never cures them completely and comes at large computational cost.

If there is a second populated Rydberg state with energy $E_{n'}$, then we find an oscillating amplitude of the artifacts with the propagation time T, as

$$\langle \chi_{\vec{k}} | \mathbb{1}_{r>R_c} | \psi_{n,n-1,0} + \psi_{n',n'-1,0} \rangle \sim b_n(k, T) + b_{n'}(k, T) \tag{2.27}$$

and consequently

$$\begin{aligned} P_{n+n'}(k, T) &\sim |b_n(k, T) + b_{n'}(k, T)|^2 && (2.28) \\ &\sim b_n(k, T) b_{n'}(k, T) \cos\big((E_n - E_{n'})(T - T_0)\big). && (2.29) \end{aligned}$$

The problem can be handled explicitly by projecting out these Rydberg states $|n\rangle$ at the end of the pulse

$$\begin{aligned} b(\vec{k}) &= \langle \chi_{\vec{k}} | \mathbb{1}_{r>R_c} Q | \psi(T) \rangle && (2.30) \\ Q &:= \mathbb{1} - \sum_n |n\rangle\langle n|. && (2.31) \end{aligned}$$

This approach is only favorable for the simplest systems where the computation of all the $|n\rangle$ comes with little computational cost.

There is also the pragmatic option to time average over these oscillating artifacts in the photo-electron spectra, which leads to quick convergence. This requires to extend time propagation until after the end of the pulse, but since this is already needed due to the low energy continuum electrons, this approach comes with little extra cost. The oscillatory behavior of equation (2.26) with T around 0 indicates that averaging over T in $b_n(k,T)$ should eliminate the artifact. Indeed,

$$\int_{T_0}^{T_1} \frac{\mathrm{d}T}{T_1 - T_0} b_n(k,T) \sim \frac{b_n(k,T_0)k^{-2}}{T_1 - T_0} \tag{2.32}$$

which leaves

$$P_n(k,T_1,T_0) \sim \frac{1}{(T_1-T_0)^2} \frac{\sin^2(kR_c)}{k^8} \overset{T_1\to\infty}{\longrightarrow} 0. \tag{2.33}$$

Both the asymptotic behavior at large k and the convergence behavior with T_1 can be seen in figure 2.2.

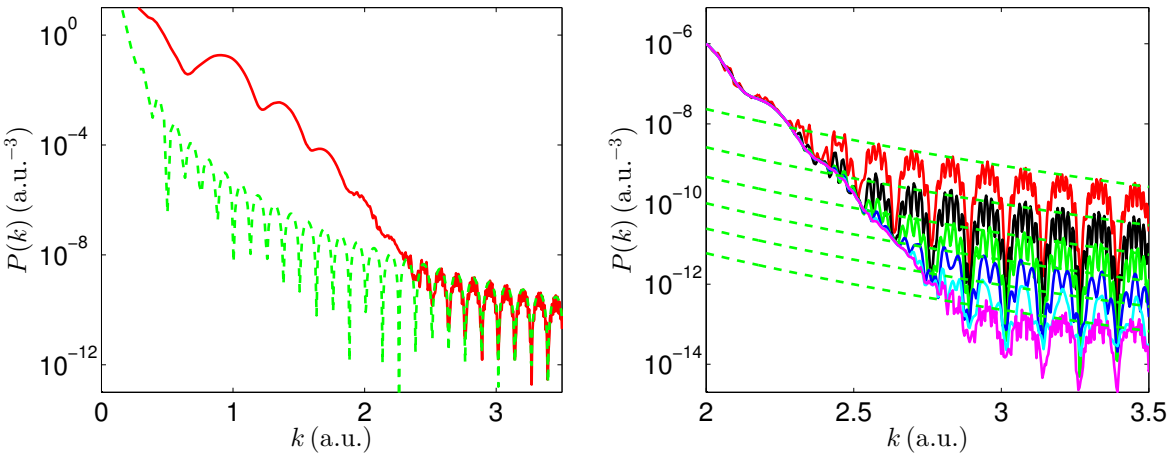

Figure 2.2: Left: Red: Numerically computed angle integrated photo-electron spectrum $P(k)$ of Hydrogen from an $\hbar\omega = 0.5$ a.u. pulse with averaging over $T_1 - T_0 = 100$ a.u.. Green: $P_n(k,T_1,T_0)$ of Eq. (2.33). We observe coinciding decay $\propto k^{-8}$ and oscillatory behavior. Right: Solid lines are numerically computed spectra for various $T_1 - T_0$, converging to the true spectrum as $T_1 - T_0$ increases (from red to magenta). Green dashed lines are the corresponding $P_n(k,T_1,T_0)$ without the $\sin^2(kR_c)$-factor, i.e. $(T_1-T_0)^{-2}k^{-8}$.

2.2 Two-electron systems

We now continue with the two particle version of tSurff [33], which is also described in Ref. [6].

2.2.1 The straight forward approach and its weaknesses

The Hamiltonian in velocity gauge is given by

$$H(t) = \left(-\frac{\Delta}{2} - \mathrm{i}\vec{A}(t)\vec{\nabla} + V(\vec{r}_1)\right) \otimes \mathbb{1} + \mathbb{1} \otimes \left(-\frac{\Delta}{2} - \mathrm{i}\vec{A}(t)\vec{\nabla} + V(\vec{r}_2)\right) + V_{ee}(\vec{r}_1, \vec{r}_2) \quad (2.34)$$

where $V_{ee}(\vec{r}_1, \vec{r}_2) = \frac{1}{|\vec{r}_1 - \vec{r}_2|}$. In the case of the helium atom the core potential is $V(\vec{r}_{1/2}) = -\frac{2}{r_{1/2}}$. The photo-electron spectrum consists of a double ionization part

$$P(\vec{k}_1, \vec{k}_2) \;=\; \left|\langle\!\langle \chi_{\vec{k}_1\vec{k}_2} | \lim_{t\to\infty} \Psi(t) \rangle\!\rangle\right|^2 \quad (2.35)$$

with outgoing final momenta $\vec{k}_1$ and $\vec{k}_2$, and a single ionization part

$$P_c(\vec{k}) = \left|\langle\!\langle \chi_{c,\vec{k}} | \lim_{t\to\infty} \Psi(t) \rangle\!\rangle\right|^2 \quad (2.36)$$

with outgoing final momentum $\vec{k}$ and residual ion configuration c (c thus indexes the bound states of He^+). Here double brackets indicate a two particle wavefunction (and single brackets will be used for single particle wavefunctions). The $\chi_{\vec{k}_1\vec{k}_2}$ and $\chi_{c,\vec{k}}$ are the fully correlated continuum wavefunctions with asymptotic outgoing momenta $\vec{k}_{1/2}$ and $\vec{k}$ respectively.

The direct approach to this problem consists of two steps, both of which are numerically challenging.

First, the multichannel wavefunction Ψ including single- and double-continuum contributions needs to be computed at the end of the pulse, a task whose complexity depends on the laser parameters. In particular, it scales very unfavorably with the laser wavelength due to a simultaneous expansion in momentum, space, and time. As in the single particle case (Sec. 2.1.1), the radial phase space volume V_r which needs to be covered by the numerical integration scales as $V_r \propto n\lambda^3 I$, only this time it applies for both electrons independently. Analogously, also the phase space volumes of the other spatial dimensions all grow as $\propto \lambda^3 I$ (V_φ and V_θ in case of spherical coordinates). The total computational effort for a linearly polarized laser pulse of length $n \cdot \tau$ then scales as

$$\propto V_r^2 \cdot V_\theta^2 \cdot n\tau \propto n^3\lambda^{13} I^4. \quad (2.37)$$

(The effort for an arbitrarily polarized pulse would scale as $\propto V_r^2 \cdot V_\theta^2 \cdot V_\varphi^2 \cdot n\tau \propto n^3\lambda^{19} I^6$, which is outside the scope of this thesis.) Except for recent studies making use of massive

computational resources, all two-electron computations have therefore been performed in the short wavelength regime $\lambda \leq 200\,\mathrm{nm}$, and only for linear polarization.

The second difficulty arises in the analysis of the wavefunction Ψ after the end of the pulse. For extracting the double emission amplitudes one would need to know the two particle stationary scattering solutions $\chi_{\vec{k}_1\vec{k}_2}(\vec{r}_1,\vec{r}_2)$ for asymptotic outgoing single particle momenta $\vec{k}_{1/2}$. These are simply unknown and analysis would involve additional, hard to control approximations. A widely used strategy to bypass this problem is to propagate Ψ, not just until the end of the pulse, but to sufficiently long times later, and then extract the relevant dynamical information entirely from the asymptotic region. Here the full scattering solutions can be approximated by products of single-particle scattering wavefunctions $\chi_{\vec{k}_1\vec{k}_2}(\vec{r}_1,\vec{r}_2) \approx \chi_{\vec{k}_1}(\vec{r}_1)\chi_{\vec{k}_2}(\vec{r}_2)$, where popular choices for $\chi_{\vec{k}}$ are Coulomb waves or even simple plane waves. In either case electron-electron interaction is neglected. The effect of this approximation can be systematically controlled by varying the propagation time. Various other strategies for the analysis of the multichannel wavefunction have been proposed, which all incur some form of inconvenience, ranging from large computational costs to inability to extract differential information. Discussions can be found in Refs. [65] or [66] and the references therein.

The direct approach has been implemented by several groups using various combinations of strategies to tackle both steps. A particularly convincing example can be found in Ref. [27], where the time-dependent close-coupling scheme (TDCC) [67] was implemented in a finite element discrete variable representation (FE-DVR) [68, 69] to compute differential two-photon cross sections. Box sizes of up to 800 a.u. were used to propagate up to 21 fs after the XUV laser pulse in order for the projection onto products of energy-normalized coulomb waves to be accurate. The exact same numerical methods were used by various other groups to study DI by few photons [70–72], and the effects of an assisting IR streaking field [73]. In Ref. [53] spatial discretization was by B-splines and analysis by projection onto products of uncorrelated numerical single-electron continuum states. In Ref. [74] spectra were computed using surface integrals involving the asymptotic form of the wavefunction and Coulomb functions, which required a box size of 130 a.u.. A strategy employing a finite differences discretization and extraction of DI spectra using masks was used to study DI processes at 390 nm [29]. In Ref. [30] the same method was used to analyze the relative importance of various DI pathways at this wavelength, which required box sizes of up to 1200 a.u.. In Ref. [31] an XUV pulse was used to enhance photo-absorption from a very short IR pulse of moderate intensity. The computations employed similar numerical techniques as Ref. [27], and were conducted on a grid with over 300 a.u. radial extension.

2.2.2 tSurff double emission

As in the single-electron case, the key step is the separation of the final wavefunction in coordinate space. For times T long after the end of the pulse and large R_c we have a separation into its bound parts Ψ_b, its singly ionized parts $\Psi_{s/\bar{s}}$ and its doubly ionized

parts Ψ_d. Apart from Rydberg states and low energetic free electrons, we may write

$$\Psi_b(\vec{r}_1,\vec{r}_2,T) \approx 0 \qquad \text{for } r_1 > R_c \text{ or } r_2 > R_c \tag{2.38}$$
$$\Psi_s(\vec{r}_1,\vec{r}_2,T) \approx 0 \qquad \text{for } r_1 < R_c \text{ or } r_2 > R_c \tag{2.39}$$
$$\Psi_{\overline{s}}(\vec{r}_1,\vec{r}_2,T) \approx 0 \qquad \text{for } r_1 > R_c \text{ or } r_2 < R_c \tag{2.40}$$
$$\Psi_d(\vec{r}_1,\vec{r}_2,T) \approx 0 \qquad \text{for } r_1 < R_c \text{ or } r_2 < R_c \tag{2.41}$$

In other words, at time T their supports are given by: $\mathrm{supp}(\Psi_b) = B := [0,R_c]\times[0,R_c]$, $\mathrm{supp}(\Psi_s) = S := [R_c,\infty)\times[0,R_c]$, $\mathrm{supp}(\Psi_{\overline{s}}) = \overline{S} := [0,R_c]\times[R_c,\infty)$ and $\mathrm{supp}(\Psi_d) = D := [R_c,\infty)\times[R_c,\infty)$, see Fig. 2.3.

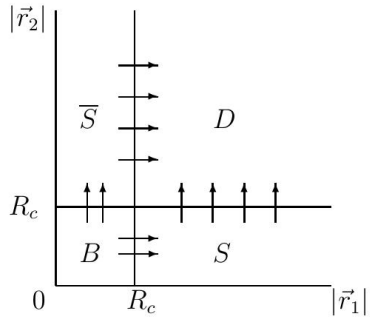

Figure 2.3: Spatial separation of bound (B), singly ionized (S and $\overline{S}$) and doubly ionized (D) wavefunction portions. Arrows indicate wave function flux contributing to ionization. Figure taken from Ref. [33].

Again we assume that outside the scaling radius R_c, the respective potentials vanish or rather we turn them off explicitly using (2.19):

$$V(\vec{r}_1) = 0 \qquad r_1 > R_c \tag{2.42}$$
$$V(\vec{r}_2) = 0 \qquad r_2 > R_c \tag{2.43}$$
$$V_{ee}(\vec{r}_1,\vec{r}_2) = 0 \qquad r_1 > R_c \text{ or } r_2 > R_c \tag{2.44}$$

which allows to use the analytically known Volkov waves.

Now we can approximate the DI spectrum by the part of the wavefunction which entered domain D at some finite time T:

$$P(\vec{k}_1,\vec{k}_2) \approx |b(\vec{k}_1,\vec{k}_2,T)|^2, \tag{2.45}$$

where the DI scattering amplitude is given by

$$b(\vec{k}_1,\vec{k}_2,T) = \langle\!\langle \chi_{\vec{k}_1,\vec{k}_2} | \psi(T) \rangle\!\rangle, \tag{2.46}$$

with the fully correlated scattering wavefunctions $\chi_{\vec{k}_1,\vec{k}_2}$. Approximating $\chi_{\vec{k}_1,\vec{k}_2}$ by scattering wavefunctions with support only on domain D, we have

$$b(\vec{k}_1,\vec{k}_2,T) \approx \langle\!\langle \chi_{\vec{k}_1,\vec{k}_2} | \mathbb{1}_{r_1>R_c}\mathbb{1}_{r_2>R_c} | \psi(T) \rangle\!\rangle. \tag{2.47}$$

This kind of approximation is not specific to tSurff. Any asymptotic analysis where the two-particle scattering functions are approximated as a product of single-particle functions implies that interparticle interactions are neglected in the asymptotic region. This is the case for all direct methods discussed above. Here we make this approximation manifest by suppressing the electron repulsion outside R_c: Rather than having a built-in error in the asymptotic analysis, we make a consistent spectral analysis of the approximate system.

We would like to point out that the approximation may possibly be avoided in tSurff [33]. An exact solution for two electrons in a laser field can be given in relative and center-of-mass coordinates $(\vec{r}_1 + \vec{r}_2)/2, \vec{r}_1 - \vec{r}_2$ if nuclear potentials can be neglected. In practice, this involves rather complicated transformations of the surfaces which we have not attempted to implement.

The scattering states are known analytically, even in the presence of the laser pulse, which is due to the simple structure of the Hamiltonian on D. It consists of two single particle Volkov Hamiltonians $H_V := -\frac{\Delta}{2} - \mathrm{i}\vec{A}(t)\vec{\nabla}$:

$$H^{(D)}(t) = H_V(t) \otimes \mathbb{1} + \mathbb{1} \otimes H_V(t), \tag{2.48}$$

and its fully analytic solutions are given by products of Volkov waves $\chi_{\vec{k}_1} \otimes \chi_{\vec{k}_2}$. In particular, the scattering states decompose into products of single particle scattering states $|\mathbb{1}_{r_1>R_c}\mathbb{1}_{r_2>R_c}\chi_{\vec{k}_1,\vec{k}_2}\rangle\!\rangle = |\mathbb{1}_{r_1>R_c}\chi_{\vec{k}_1}\rangle \otimes |\mathbb{1}_{r_2>R_c}\chi_{\vec{k}_2}\rangle$. Using tSurff, this is a consequence of the truncated Coulomb potentials, in standard approaches this is an explicit approximation.

Repeating the transformation shown in Eq. (2.16), we can write the projection (2.46) as the time integrated fluxes from regions S and $\overline{S}$ into D:

$$b(\vec{k}_1, \vec{k}_2, T) = \int_{-\infty}^{T} \mathrm{d}t \, \big(\underbrace{F(\vec{k}_1, \vec{k}_2, t)}_{S\to D} + \underbrace{F(\vec{k}_2, \vec{k}_1, t)}_{\overline{S}\to D} \big). \tag{2.49}$$

with

$$F(\vec{k}_1, \vec{k}_2, t) = \Big(\langle \chi_{\vec{k}_1}(t)\mathbb{1}_{r_1>R_c}| \otimes \langle \chi_{\vec{k}_2}(t)|[H_V(t), \mathbb{1}_{r_2>R_c}] \Big) |\Psi(t)\rangle\!\rangle. \tag{2.50}$$

The flux is determined by the time evolution on S where the Hamiltonian is given by

$$H^{(S)}(t) = H_V(t) \otimes \mathbb{1} + \mathbb{1} \otimes H_{\mathrm{ion}}(t) \tag{2.51}$$

with $H_{\mathrm{ion}} = -\frac{\Delta}{2} - \mathrm{i}\vec{A}(t)\vec{\nabla} + V(\vec{r})$. The Hamiltonian on S retains the tensor product structure which separates the problem on S into two independent single particle problems, where for one the solution is again given by Volkov waves. Solutions $\Psi^{(S)}$ of $H^{(S)}(t)$ can thus be written as products of Volkov waves $\chi_{\vec{k}_1}(\vec{r}_1, t)$ and solutions of the ionic problem $\varphi_{\vec{k}_1}(\vec{r}_2, t)$ on $r_2 < R_c$. There is a slight complication with the orthogonality of plane waves, as

$$\langle \chi_{\vec{k}}|\mathbb{1}_{r>R_c}|\chi_{\vec{k}'}\rangle = S_{\vec{k}\vec{k}'} \neq \delta(\vec{k} - \vec{k}'). \tag{2.52}$$

We assume there exists an inverse $S^{-1}_{\vec{k}\vec{k}'}$ such that $\int \mathrm{d}\vec{k}' \, S_{\vec{k}\vec{k}'} S^{-1}_{\vec{k}'\vec{k}''} = \delta(\vec{k} - \vec{k}'')$ and define

$$\Psi^{(S)}(\vec{r}_1, \vec{r}_2, t) = \int \mathrm{d}\vec{k}'_1 \, \varphi_{\vec{k}'_1}(\vec{r}_2, t) \int \mathrm{d}\vec{k}''_1 \, \chi_{\vec{k}''_1}(\vec{r}_1, t) S^{-1}_{\vec{k}''_1\vec{k}'_1}. \tag{2.53}$$

Inserting this into Eq. (2.50) gives the flux from S into D as

$$\begin{aligned} & F(\vec{k}_1, \vec{k}_2, t) \\ = & \int \mathrm{d}\vec{k}_1' \int \mathrm{d}\vec{k}_1'' \langle \chi_{\vec{k}_1}(t) \mathbb{1}_{r_1>R_c} | \chi_{\vec{k}_1''}(t) \rangle S^{-1}_{\vec{k}_1''\vec{k}_1'} \langle \chi_{\vec{k}_2}(t) | [H_V(t), \mathbb{1}_{r_2>R_c}] | \varphi_{\vec{k}_1'}(t) \rangle \\ = & \langle \chi_{\vec{k}_2}(t) | [H_V(\vec{r}_2, t), \mathbb{1}_{r_2>R_c}] | \varphi_{\vec{k}_1}(t) \rangle. \end{aligned} \tag{2.54}$$

It is important to note that the ionic factor $\varphi_{\vec{k}_1}(\vec{r}_2, t)$ depends on the asymptotic momentum $\vec{k}_1$. This coupling occurs, as $\varphi_{\vec{k}_1}$ is determined by an *inhomogeneous* TDSE, where the inhomogeneity accounts for the flux from region B into S, see Fig. 2.3. The flux $B \to S$ is correlated, such that each momentum component $\vec{k}_1$ contributes differently to the wavefunction in $\vec{r}_2$ direction. The inhomogeneous equation for $\varphi_{\vec{k}_1}(\vec{r}_2, t)$ is given by

$$\begin{aligned} \mathrm{i}\partial_t |\varphi_{\vec{k}_1}(\vec{r}_2, t)\rangle &= \mathrm{i}\partial_t \langle \chi_{\vec{k}_1}(\vec{r}_1, t) | \Psi^{(S)}(\vec{r}_1, \vec{r}_2, t) \rangle\!\rangle \\ &= H_{\mathrm{ion}}(t) |\varphi_{\vec{k}_1}(\vec{r}_2, t)\rangle - |J_{\vec{k}_1}(\vec{r}_2, t)\rangle \end{aligned} \tag{2.55}$$

obtained by inserting Eq. (2.53). The inhomogeneous source term is

$$|J_{\vec{k}_1}(\vec{r}_2, t)\rangle = \langle \chi_{\vec{k}_1}(\vec{r}_1, t) | \big[H_V(\vec{r}_1, t), \mathbb{1}_{r_1>R_c} \big] | \Psi(\vec{r}_1, \vec{r}_2, t) \rangle\!\rangle \tag{2.56}$$

and the initial condition is

$$\varphi_{\vec{k}_1}(\vec{r}_2, -\infty) = 0. \tag{2.57}$$

For evaluating (2.55) we need the values and derivatives of the $\Psi(\vec{r}_1, \vec{r}_2, t)$ on the boundary $r_1 = R_c$ between domains B and S. This requires the solution of the full 6-dimensional (in case of linearly polarized pulses 5-dimensional) two-electron TDSE on B governed by the full Hamiltonian (2.34) which has no tensor product structure. Beyond R_c the two particle wavefunction Ψ can be disposed off by absorption. Details on the choice of absorber and its implementation are given in Sec. 3.2.

The commutators appearing in Eqs. (2.54) and (2.56) are the same as in the single particle version, Eq. (2.16). An explicit form for the implied projection from a two particle wavefunction to a single particle wavefunction in Eq. (2.56) is given in appendix 8.5.2.

2.2.3 Gain

To summarize, the tSurff method for computing double emission spectra $P(\vec{k}_1, \vec{k}_2)$ amounts to:

1. Choose sets for $\vec{k}_1$ and $\vec{k}_2$ at which the spectrum shall be computed.
2. Setup a discretized two-electron wavefunction on domain B with a traceless absorber outside and initialize the system to the groundstate.
3. Setup one discretized single-electron wavefunction on domain S for every $\vec{k}_1$, each with absorbing boundary condition, and each initialized to zero.

4. Initialize the scattering amplitude $b(\vec{k}_1, \vec{k}_2)$ to zero.

5. Propagate the system from the beginning of the pulse until some time T after the end of the pulse. For every time step this implies:

   (a) Do the time step on B according to the full Hamiltonian (2.34).

   (b) Compute the source term $J_{\vec{k}_1}(\vec{r}_2, t)$ for every $\vec{k}_1$ according to Eq. (2.56).

   (c) For every $\vec{k}_1$ do the time step of the TDSE (2.55) on S.

   (d) Compute the flux from domain $S \to D$ for every $\vec{k}_1$ and $\vec{k}_2$, Eq. (2.54).

   (e) Add the exchange symmetric flux and integrate according to Eq. (2.49).

6. Finally, the spectrum $P(\vec{k}_1, \vec{k}_2)$ is given by $|b(\vec{k}_1, \vec{k}_2, T)|^2$, equation (2.45).

The power of the method is that time propagation with the full Hamiltonian (2.34) only happens on domain B. For large wavelengths the radial extension of domain B is determined by the quiver amplitude r_q of the electron in the field. In contrast, using the standard approach for computing differential DI spectra, the radial extension of the computation box is given by the maximal distance $r_{\max}$ the wavepacket can reach by the end of time propagation. As in the single particle case, Eq. (2.18), the radial extension of the computation box is therefore reduced by a factor of approximately $10n$. This reduction does however apply for both electron's coordinates. tSurff for double emission at long wavelengths thus reduces the computational effort of time propagation with the full Hamiltonian by a factor of $\sim(10n)^2$ compared to the standard approach. At short wavelengths the required radial extension of the box solely depends on the desired level of accuracy, in both the standard approach and with tSurff.

The cost is the appearance of steps 5 (b)-(e). Solving the array of single particle TDSEs may represent a certain computational challenge depending on the desired $\vec{k}_1$-grid. It is however insignificant compared to the tremendous task the fully correlated two particle problem represents, as problem size only scales as $\lambda^7 I^2$ instead of $\lambda^{13} I^4$, see sections 2.1.1 and 2.2.1. Also, the computations for different $\vec{k}_1$ are completely independent, which lends itself to straight forward parallelization.

2.2.4 Single emission

With $\varphi_{\vec{k}_1}(\vec{r}_2, t)$ (determined by equation (2.55)) known at the final time T after the pulse we can reconstruct the full wavefunction for $|r_1| > R_c$. The projection onto products of an ionic bound state $\phi^{(c)}(\vec{r}_2)$ with Volkov waves $\chi_{\vec{k}_1}(\vec{r}_1)$ gives the single ionization scattering amplitude $b^{(c)}(\vec{k}_1, T)$ into ionic channel c:

$$b^{(c)}(\vec{k}_1, T) \approx \langle \phi^{(c)} | \varphi_{\vec{k}_1}(T) \rangle. \tag{2.58}$$

For the spectral densities, a factor 2 accounts for the symmetric contributions from S and $\overline{S}$:

$$P^{(c)}(\vec{k}, T) = 2|b^{(c)}(\vec{k}, T)|^2. \tag{2.59}$$

If double ionization is negligible, the problem can be further simplified by admitting only contributions from the source (2.56) that will end up in ionic channel c. We introduce the ionic solution

$$\mathrm{i}\partial_t \phi^{(c)}(\vec{r}_2, t) = H_{\mathrm{ion}}(\vec{r}_2, t)\phi^{(c)}(\vec{r}_2, t) \tag{2.60}$$

with a *final* condition at $t = T$

$$\phi^{(c)}(\vec{r}_2, T) = \phi^{(c)}(\vec{r}_2). \tag{2.61}$$

With that the single ionization scattering amplitude into ionic channel c is given by

$$b^{(c)}(\vec{k}_1, T) = \int_{-\infty}^{T} \mathrm{d}t \, \langle \phi^{(c)}(t) | J_{\vec{k}_1}(t) \rangle. \tag{2.62}$$

The simplification is significant, as the ionic solution $\phi^{(c)}(\vec{r}_2, t)$ needs to be computed only once for all $\vec{k}_1$. This approach was used in Refs. [4] and [5] to compute single ionization spectra from multi-electron systems including core polarization and doubly excited states.

Instead of propagating $\phi^{(c)}$ backwards in time to fulfill the final condition at $t = T$, we may also compute single ionization into the ionic channel defined by $\phi^{(c)}$ at $t = -\infty$. Assuming no further ionization, this state evolves into a superposition of ionic bound states at the end of the pulse:

$$|\tilde{\phi}^{(c)}(T)\rangle = \sum_{\gamma} \alpha_{\gamma}^{(c)} |\phi^{(\gamma)}\rangle \tag{2.63}$$

Further assuming orthogonality of all ionic bound states also during the pulse (which is satisfied as long as the ionic states are only little affected by the pulse), we may reconstruct ionization into a specific final bound state ionic channel by inverting the matrix $\alpha_{\gamma}^{(c)}$:

$$|\phi^{(c)}(T)\rangle = \sum_{\gamma} \left(\alpha_{\gamma}^{(c)}\right)^{-1} |\tilde{\phi}^{(\gamma)}\rangle. \tag{2.64}$$

2.2.5 Limitations

The two particle version of the tSurff method inherits from its single particle predecessor the convergence properties with respect to propagation time and the truncation radius of the nuclear Coulomb potential, as well as the effects of excited bound states and position of the absorber, section 2.1.4.

The effects of Rydberg states reaching into the tSurff radius R_c are similar for double emission, see Fig. 2.4.

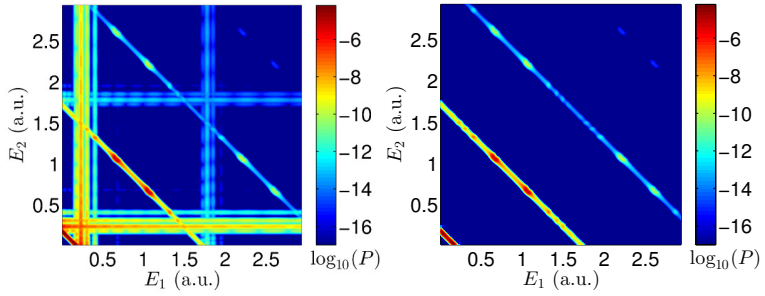

Figure 2.4: Left: Angle-integrated double ionization spectrum $P(E_1, E_2)$ of an XUV pulse hitting a Helium atom, as computed with tSurff and with no treatment of Rydberg states. Right: With averaging as in Eq. (2.33) many of the structures disappear and can thus be identified as unphysical. The remaining structures will be explained in chapter 6.

Specific for two-electron systems is the error introduced by approximating the asymptotics of the exact scattering solution in product form $\chi_{\vec{k}_1,\vec{k}_2} \approx \chi_{\vec{k}_1}\chi_{\vec{k}_2}$. This error decreases with growing R_c. As the essence of tSurff is to keep R_c as small as possible, it is affected most acutely by this. In the direct approach, the product ansatz is made typically only beyond $|\vec{r}| \gtrsim 100$, either explicitly or implicitly as in Ref. [74]. We will show that, depending on the observable in question, tSurff radii as small as $R_c \approx 20$ can give sensible results. Some observables are strongly affected by this approximation: whenever "postcollision" interaction, i.e. repulsion between electrons far from the nucleus, is important, a product description is bound to fail. This is most pronounced for side-by-side double emission, where the two electrons are in close proximity for long times. The relevant distances depend on the details of the process [75]. If these distances lie beyond practical R_c values, tSurff would need to be amended by fully including post-collision electron-electron interaction [33], but such an approach has not been proven yet in practice.

Chapter 3

Numerical solution of the Schrödinger equation

The physical process of a small atom being hit by a short and intense laser pulse and thereby possibly ionizing is well described by the time-dependent Schrödinger equation (TDSE). All approximations are justified for all laser wavelengths and intensities of interest here (see Sec. 1.3). A description by a simpler theory requires additional approximations which are not always fully justified. In particular in the long wavelength regime only the TDSE gives reliable and quantitatively correct results, which can in general only be obtained employing numerical approaches since no fully analytic solution exists for the case of laser-matter interaction.

Such a numerical approach can be broken down into three main steps:

1. The system is to be discretized by expanding the wavefunction $|\Psi(t)\rangle \in \mathcal{H}$ in a finite number N_{coef} of basis functions $\{f_n\}$:

$$|\Psi(t)\rangle = \sum_{n=1}^{\infty} |f_n\rangle c_n(t) \overset{!}{\approx} \sum_{n=1}^{N_{\text{coef}}} |f_n\rangle c_n(t). \tag{3.1}$$

   Choosing the basis $\{f_n\}$ is the conceptually most difficult step, as it requires knowledge of the system's dynamics before having access to the solution. The subspace $\text{span}(\{f_n\}_{n\leq N_{\text{coef}}}) \subset \mathcal{H}$ must be large enough that it covers all populated states of the system, but at the same time it should be as small as possible in order to reduce the size of the numerical problem. Time-dependent basis functions $|f_n(t)\rangle$ are not considered here.

2. For the chosen basis $\{f_n\}$ the corresponding matrices are to be computed. These appear when transforming the partial differential equation (1.1) into its discretized

form using the chosen basis:

$$\begin{aligned} \langle f_i|\mathrm{i}\partial_t|\Psi(t)\rangle &= \langle f_i|H(t)|\Psi(t)\rangle \\ \partial_t \sum_{j=1}^{N_{\mathrm{coef}}} \underbrace{\langle f_i|f_j\rangle}_{=:\widehat{S}_{ij}} c_j(t) &= -\mathrm{i}\sum_{j=1}^{N_{\mathrm{coef}}} \underbrace{\langle f_i|H(t)|f_j\rangle}_{=:\widehat{H}_{ij}(t)} c_j(t) \\ \partial_t \vec{c}(t) &= -\mathrm{i}\widehat{S}^{-1}\widehat{H}(t)\vec{c}(t) \end{aligned} \tag{3.2}$$

This is an ordinary differential equation, where $\widehat{S}$ is called the Overlap matrix and $\widehat{H}$ is called the Hamiltonian matrix. The solution of this equation on $\mathrm{span}(\{f_n\}) \subset \mathcal{H}$ minimizes the time-local error compared to the full solution on $\mathcal{H}$ [76].

3. This equation is to be propagated in time starting with the appropriate initial condition.

Steps two and three are conceptually easy, as they just require straight forward computations and can be fully automatized. In particular the time propagation step may however represent a formidable computational task which makes a numerically efficient implementation essential.

In this chapter we start by describing the used basis set and discussing its merits. Then we summarize the employed technique for implementing absorbing boundary conditions. After a detailed description of the computationally most challenging part in case of two-electron systems, the electron-electron interaction, we describe the code structure and how it automatically computes all appearing matrices. Then time propagation and parallelization are discussed, followed by a summary of all convergence parameters and a short comment on the choice of gauge for the electromagnetic interaction.

3.1 Discretization

In this thesis we will mainly present results for Hydrogen-like atoms and the Helium atom. We start by describing the hydrogenic single particle basis and then move on to the two particle basis for Helium, which is just a combination of two single particle bases.

3.1.1 Single particle basis

3.1.1.1 Spherical harmonics

Before any interaction with an external laser pulse, a single Hydrogen atom will be in its groundstate. The corresponding wavefunction is mainly restricted close to the nucleus and has spherical symmetry which advocates a spherical coordinate system. Also, the tSurff method for computing photo-electron spectra is naturally implemented in spherical coordinates due to the appearance of the tSurff radius R_c, see Eq. (2.17).

Although a laser pulse will break this symmetry, a separation into a radial part and an angular part is still efficient. In particular, the eigenfunctions of the Laplace operator Δ, the spherical harmonics $Y_l^m(\theta, \varphi)$, have several useful properties:

1. They are ideally suited for representing hydrogenic bound states.

2. In case of linearly polarized pulses they embrace the cylindrical symmetry of the system: $m \equiv 0$.

3. The representations of dipole operators have a local structure, i.e. they only connect neighboring $l \pm 1$ and $m \pm 1$.

Thus, with $(\theta, \varphi) \equiv \Omega$, we discretize

$$\psi(r, \Omega, t) \overset{!}{\approx} \sum_{m=-m_{\max}}^{m_{\max}} \sum_{l=|m|}^{l_{\max}} Y_l^m(\Omega) R_{lm}(r, t) \tag{3.3}$$

where the maximum values $l_{\max}$ and $m_{\max}$ are convergence parameters and are determined by the laser pulse.

The values for $l_{\max}$ and $m_{\max}$ required to cover the relevant parts of the Hilbert space can be estimated by analyzing the motion of free electrons in the laser field. Depending on the gauge however, the free motion is described more or less naturally, resulting in different demands on the angular momentum expansion. Velocity gauge is numerically more efficient in strong field problems (see Sec. 3.7), as it absorbs parts of the quiver motion into the time-dependent momentum operator $[\mathrm{i}\vec{\nabla} - \vec{A}(t)]$.

For velocity gauge, the free motion is given by Volkov waves $\chi_{\vec{k}}(\vec{r}, t)$, Eq. (2.15). In the angular momentum expansion of the plane wave factor a strong radial dependence via spherical Bessel functions j_l appears:

$$\mathrm{e}^{\mathrm{i}\vec{k}\vec{r}} = 4\pi \sum_{l=0}^{\infty} \sum_{m=-l}^{l} \mathrm{i}^l j_l(kr) Y_l^m(\Omega_r) Y_l^{*m}(\Omega_k). \tag{3.4}$$

These decay exponentially beyond a certain (l-dependent) value, and therefore a given radius $r_{\max}$ together with a maximum momentum $k_{\max}$ dictate the number $l_{\max}$ above which only exponentially small corrections are added. For large $(k_{\max} \cdot r_{\max})$ the dependence is linear, i.e.

$$l_{\max} \propto k_{\max} r_{\max} \propto \lambda^3 I. \tag{3.5}$$

Here we used that $k_{\max} \propto \sqrt{I}\lambda$ (Eq. (2.3)) and approximated the maximum radius by the quiver radius $r_q \propto \sqrt{I}\lambda^2$, Eq. (1.12), as this is approximately the distance at which the electron may still return close to the core and thus deviate from the free quiver motion. Linearly polarized pulses conserve $m \equiv 0$, but for arbitrarily polarized pulses also $m_{\max} \propto \lambda^3 I$.

3.1.1.2 Interpolating values and total yield

If at the end of the laser pulse angular momenta up to $(l_{\max}, m_{\max})$ are populated, then also the spectrum $P(\vec{k}) = |b(\vec{k})|^2$ represented in spherical harmonics contains information only up to $(l_{\max}, m_{\max})$, which follows from the shared expansion of the angles in Eq. (3.4). When choosing the $\vec{k}$ for which to compute the spectrum (Eq. (2.16)) this should be taken into account, for example by only evaluating at angular points on a quadrature grid of size $l_{\max} \cdot m_{\max}$.

Then we may transform to a (l, m)-grid via

$$b_{lm}(k) = \int \mathrm{d}\Omega\, Y_l^{*m}(\Omega) b(\Omega, k), \qquad b(\Omega, k) = \sum_{l,m} b_{lm}(k) Y_l^m(\Omega), \tag{3.6}$$

and the evaluation of $b(\Omega, k)$ at arbitrary Ω can afterwards be correctly done by interpolation with spherical harmonics without additional computational cost.

Here a short remark concerning the total yield. It can be computed from the spectrum $P = |b|^2$ as

$$Y = \int_{\mathbb{R}^3} \mathrm{d}^3k\, P(\vec{k}) = \int_0^\infty \mathrm{d}k\, k^2 \sum_{l,m} P_{lm}(k) =: \int_0^\infty \mathrm{d}E \sum_{l,m} P_{lm}(E) \tag{3.7}$$

with $P_{lm} = |b_{lm}|^2$, $E = k^2/2$, and where a Jacobian factor $\sqrt{2E}$ was absorbed into $P_{lm}(E)$ in the last step. After angular integration we have

$$Y = \int_0^\infty \mathrm{d}k\, k^2 P(k) =: \int_0^\infty \mathrm{d}E\, P(E). \tag{3.8}$$

The total yield also allows for an easy consistency check as it is given by

$$Y = \int_{r \le R_c} \mathrm{d}^3r\, |\psi(\vec{r}, t \to \infty)|^2 \tag{3.9}$$

except for long range tails of populated bound states.

3.1.1.3 Finite elements

The radial part $R_{lm}(r, t)$ in Eq. (3.3) is discretized with spatially local basis functions such that the corresponding matrices are sparse. Several such local basis sets exist, each with its own minor advantages and disadvantages. All of them have the property to block-diagonalize the corresponding matrices which is essential for efficient numerical application.

In this thesis we employed two methods for the radial discretization: high order finite elements (FE) and a finite element discrete variable representation (FE-DVR) [68,69]. The latter is only used for the efficient implementation of the electron-electron interaction in the Helium system, which is why we defer its discussion to Sec. 3.3.

Construction: The high rank finite element discretization is described in Ref. [77]. It divides the axis into N elements $[r_{n-1}, r_n]$, $n \in \{1 \dots N\}$. On each element we have p_n linearly independent polynomials $\{f_i^{(n)}\}_{i=1\dots p_n}$ satisfying

$$f_k^{(n)}(r_{n-1}) = \quad 0 \quad = f_k^{(n)}(r_n), \tag{3.10}$$

$$\text{except } f_1^{(n)}(r_{n-1}) = \quad 1 \quad = f_{p_n}^{(n)}(r_n). \tag{3.11}$$

With these conditions, the overlap matrix on each finite element $S_{ij}^{(n)} = \langle f_i^{(n)} | f_j^{(n)} \rangle$ can be transformed such that it is diagonal except for the two off-diagonal elements $S_{1,p_n} = S_{p_n,1}^* \neq 0$. The end-elements may have modified constraints to implement the desired boundary conditions. In our case these are $f(r \to \infty) = 0$, and after absorbing the Jacobian also $f(r = 0) = 0$, see below.

Continuity of the wavefunction across element boundaries requires special attention, and is described in appendix 8.6. Continuity of the first derivative need not be enforced if matrix elements are computed in symmetrized forms as explained in Ref. [78].

Centrifugal barrier: The asymptotic behavior at the origin is known for single centered systems, in particular $R_{lm}(r,t) \propto r^l$ for $r \to 0$. This behavior can be directly included into the basis functions by defining

$$f_k^{(n,l)}(r) := r^l f_k^{(n)}(r) \tag{3.12}$$

to discretize the first finite element $[0, r_1]$. For given maximum order of the finite element discretization, the order of the $f_k^{(n)}$ which are multiplied with r^l can be reduced by l. This not only directly reduces the total number of discretization coefficients, but also leads to a more tailored discretization in which the r^l behavior does not need to be imitated by the basis but is automatically present. This results in

$$\psi(r, \Omega, t) \overset{!}{\approx} \sum_{lmnk} Y_l^m(\Omega) f_k^{(n,lm)}(r) c_{lmnk}(t). \tag{3.13}$$

It was expected that this would decrease the number of large and unphysical eigenvalues in the Hamiltonian matrix, and thereby reduce the stiffness of the TDSE (also see section 3.5.2), which however turned out to be a marginal effect.

Estimating number of elements and order: Analogous to the discrete Fourier representation of momenta, the maximal momentum $k_{\max} \propto \lambda\sqrt{I}$ (see Eq. (2.3)) which needs to be represented determines a grid point density. Thus the total number of radial coefficients $N_{\text{coef}} = \sum_n^N p_n$ can be estimated to be proportional to $k_{\max}$. The quality of a radial discretization with fixed N_{coef} however strongly depends on the orders p_n: Typically, convergence is achieved much quicker by increasing the order [76], the drawback being less sparse corresponding matrices. For each set of laser parameters an adequate balance between matrix sparsity and overall problem size has to be found to maximize the resulting numerical efficiency.

3.1.1.4 Other possible basis sets

A multitude of other possible basis function sets could be used. For a single-centered system the spherical harmonic basis is appropriate, but for multi-centered systems other coordinate systems can be better suited. For example, prolate spheroidal coordinates are tailored for the two-centered structure of a binary molecule such as H_2^+ [79].

The radial discretization has however many alternatives. Finite difference schemes, B-splines, the here used finite elements and FE-DVR are all fine choices, and their compatibility with our choice of absorber (Sec. 3.2) has been proven already [80]. Also compatibility with the tSurff technique for extraction of photo-electron spectra (chapter 2) has recently been shown, although not yet published. Due to these recent insights, we expect FE-DVR to be numerically advantageous compared to our finite elements. In particular the overlap matrix $\widehat{S}$ would become trivial, obviating the complicated application of its inverse $\widehat{S}^{-1} = \widehat{\mathbb{1}}$, see appendix 8.6, and thereby simplifying efficient parallelization, see Sec. 3.5.4.

3.1.2 Two particle basis

3.1.2.1 Angular momentum grids

For the representation of a two particle wavefunction $\Psi(\vec{r}_1, \vec{r}_2, t)$ we just combine two single particle basis sets. In particular we again use spherical harmonics, i.e.

$$\Psi(\vec{r}_1, \vec{r}_2, t) \equiv \Psi(r_1, \Omega_1, r_2, \Omega_2, t) \overset{!}{\approx} \sum_{l_1 m_1} Y_{l_1}^{m_1}(\Omega_1) \sum_{l_2 m_2} Y_{l_2}^{m_2}(\Omega_1) R_{l_1 m_1 l_2 m_2}(r_1, r_2, t), \quad (3.14)$$

where the sums are truncated at $l_{\max}$ and $m_{\max}$ respectively. In the literature often a linear combination of the spherical harmonics was used, namely the coupled spherical harmonics $\mathcal{Y}_{l_1 l_2}^{LM}(\Omega_1, \Omega_2) := \sum_{m_1 m_2}^{m_{\max}} \langle l_1 m_1 l_2 m_2 | l_1 l_2 L M \rangle Y_{l_1}^{m_1}(\Omega_1) Y_{l_2}^{m_2}(\Omega_1)$, with Clebsch-Gordan coefficients $\langle l_1 m_1 l_2 m_2 | l_1 l_2 L M \rangle$. Such a basis allows for an easy truncation in the total angular momenta L and M. Mathematically, these basis sets are however fully equivalent, as they span the same space. The convenience of truncation at total angular momenta is negligible for M, as setting $M_{\max} = 0$ (as appropriate for linearly polarized pulses) is equivalent to only including $m_2 = -m_1$ in our basis. For the azimuthal quantum number, the easy truncation in the total angular momentum L when using coupled spherical harmonics is indeed useful, but only at small wavelengths, where dynamics are initiated by the absorption of only few photons. We simply adjust the angular momentum grids by inspecting the population within partial waves at the borders of the grid. This is described now in more detail:

In the perturbative regime no deviation from a simple square l_1-l_2-grid seems useful since the maximal populated angular momentum of l_1 is found to be independent of l_2. At larger wavelengths, the populated angular momentum grids have a more complex shape. In figure 3.1 we show the maximal population $\rho_{l_1 l_2}^{\max}$ achieved in the partial waves $(l_1, l_2, m_1 = 0 = m_2)$

during time propagation for an exemplary pulse at IR wavelength. Thereby

$$\rho_{l_1 l_2}^{\max} := \max_t \rho_{l_1 l_2}(t) \tag{3.15}$$

where $\rho_{l_1 l_2}(t) := \|\Psi_{l_1 l_2}(t)\|^2$ with $\Psi_{l_1 l_2}(r_1, r_2, t) = \int \mathrm{d}\Omega_1 \mathrm{d}\Omega_2 \, Y_{l_1}^0(\Omega_1) Y_{l_2}^0(\Omega_2) \Psi(\vec{r}_1, \vec{r}_2, t)$.

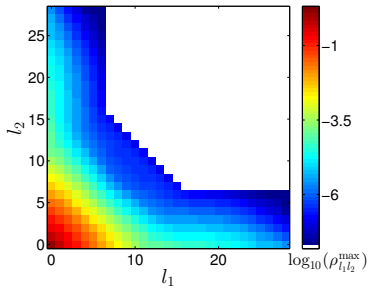

Figure 3.1: Illustration of a possible truncation of the angular momentum $(l_1, l_2, m = 0)$ grid and the corresponding maximal population $\rho_{l_1 l_2}^{\max}$ for a linearly polarized pulse with $\lambda = 780\,\mathrm{nm}$ and $I = 2 \cdot 10^{14}\,\mathrm{W/cm^2}$.

Enlarging the grid results in lower maximum population at the borders of the grid:

$$\rho_{\mathrm{border}}^{\max} := \max_{l_1 l_2 \in \mathrm{border}} \left[\rho_{l_1 l_2}^{\max}\right], \tag{3.16}$$

where different observables require different $\rho_{\mathrm{border}}^{\max}$ for convergence. l_1-l_2-grids for $m = \pm 1$, ± 2 and ± 3 are restricted similarly, although significantly smaller grids suffice. Contributions from $m = \pm 4$ are usually negligible for linearly polarized pulses and our desired degree of precision, as population of the m-components of Ψ changes only indirectly by electron collisions and not directly due to the laser pulse.

3.1.2.2 Radial discretization

For the radial discretizations of the two electrons we simply combine two single particle bases (3.13):

$$R_{l_1 m_1 l_2 m_2}(r_1, r_2, t) = \sum_{n_1 k_1} \sum_{n_2 k_2} f_{k_1}^{(n_1, l_1 m_1)}(r_1) f_{k_2}^{(n_2, l_2 m_2)}(r_2) c_{l_1 m_1 k_1 l_2 m_2 k_2}^{(n_1, n_2)}(t) \tag{3.17}$$

with the same $f_k^{(n),lm}(r)$ as in section 3.1.1.3. This divides the r_1-r_2-space into finite element patches (n_1, n_2) on which all operations are local. Only continuity and the inverse overlap connect different patches, see appendix 8.6.

3.1.2.3 Exchange symmetry

We want to describe a two-electron system where the spins of the electrons are in the singlet state at some arbitrary initial time. As we are neglecting relativistic contributions, the initial spin configuration is conserved. This implies a symmetric spatial wavefunction under particle exchange:

$$\Psi(\vec{r}_1, \vec{r}_2, t) = \Psi(\vec{r}_2, \vec{r}_1, t) \tag{3.18}$$

for all times t, or equivalently

$$c^{(n_1,n_2)}_{l_1 m_1 k_1 l_2 m_2 k_2}(t) = c^{(n_2,n_1)}_{l_2 m_2 k_2 l_1 m_1 k_1}(t). \tag{3.19}$$

Using this symmetry reduces the total number of coefficients by nearly a factor of two. Except for finite element patches on the diagonal $n_1 = n_2$, also the overall number of non-zero entries in the matrices $\widehat{H}$ and $\widehat{S}$ is reduced by a factor of two. In the current implementation of the code this symmetry is not exploited, which reduces the algorithmic complexity, in particular in the application of the inverse overlap (Sec. 8.6).
If by employing a different radial discretization (e.g. FE-DVR instead of our finite elements) the inverse overlap becomes obsolete, taking advantage of the exchange symmetry may become an easy way to reduce the computational effort by nearly a factor of two.

3.2 Absorption using Exterior Complex Scaling

As described in chapter 2, our method for extracting photo-electron spectra allows for the numerical solution of the TDSE (1.1) on reduced volumes. This affects all equations of the form (3.2). Outside these volumes a traceless absorber may be employed. Being able to push the starting point for absorption as close to the nucleus as possible is desired as this reduces the computational effort. The limit is given by the level of inaccuracy one can tolerate, where possible sources for errors are described in Sec. 2.1.4. Thus, the requirement on the absorber to be perfect is strict, as any reflections at short distances immediately affect the dynamics close to the core and amplify quickly.

For that purpose we employ infinite range exterior complex scaling (irECS) [77]. Exterior complex scaling is an analytical continuation method and has the useful property to preserve (in principle) the full information of the dynamics even in the absorbing region. This allows for particle re-entry from the scaled into the unscaled region, although in numerical computations excessive excursion into the scaled region will lead to accumulation of numerical errors. Typically, small tails of rescattering wavepackets moderately extending into the absorbing region are sufficiently undisturbed, which allows for box sizes close to or even below the quiver amplitude. Explicit numerical evidence for this fact was given in Ref. [77]. Due to these properties, irECS is an efficient choice for the absorber, its use is however not essential for tSurff. Any absorber may be used, as long as it satisfies the stringent requirements.

Choice of gauge

Note that exterior complex scaling only works with suitable operators. It can be used in the velocity gauge representation of the dipole operator $\mathrm{i}\vec{A}(t)\cdot\vec{\nabla}$, but not in length gauge $\vec{E}(t)\cdot\vec{r}$. Fortunately, velocity gauge is also numerically favored for strong field problems [3, 81], which is also discussed in Sec. 3.7.

Definition of Exterior Complex Scaling

Exterior Complex Scaling (ECS) [82] is defined by the coordinate rotation into the lower complex plane starting at some scaling radius R_0,

$$r \mapsto r_\theta = \begin{cases} r & r \leq R_0 \\ \mathrm{e}^{\mathrm{i}\theta}(r - R_0) + R_0 & r > R_0. \end{cases} \tag{3.20}$$

with the scaling angle $\theta > 0$.

Its effect is that it turns outgoing plane waves into exponentially decaying ones:

$$\mathrm{e}^{\mathrm{i}kx} \overset{x>R_0}{\longmapsto} \mathrm{e}^{\mathrm{i}k\cos\theta(x-R_0)}\mathrm{e}^{-k\sin\theta(x-R_0)}\mathrm{e}^{\mathrm{i}kR_0} \overset{x\to\infty}{\longrightarrow} 0. \tag{3.21}$$

The effect on the spectrum is a rotation of the continuous part into the lower complex plane by an angle 2θ. The discrete part of the spectrum is unchanged. In Fig. 3.2 the spectrum of a discretized field free scaled Hamiltonian $\widehat{H}_\theta$ for the Hydrogen atom is shown.

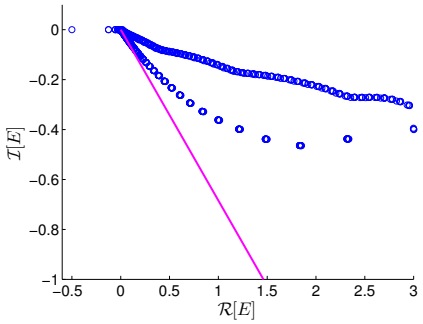

Figure 3.2: Eigenvalues of complex scaled field free Hamiltonian matrix $\widehat{H}_\theta$ for the Hydrogen system. The magenta line has an angle 2θ with the abscissa. The eigenvalues with $\mathcal{R}[E] > 0$ do not fully follow this line because of the discretization with only a finite number of basis functions. The bound states of the system are not affected by the complex scaling transformation, which implies that eigenvalues with $\mathcal{R}[E] < 0$ do not change.

This coordinate rotation is implemented by the following transformation:

$$U_\lambda^{(R)} : L^2(\mathbb{R}^+) \rightarrow L^2(\mathbb{R}^+) \tag{3.22}$$

$$\psi \mapsto U_\lambda^{(R)}\psi \equiv \psi_\lambda \tag{3.23}$$

$$\psi_\lambda(x) := \begin{cases} \psi(x) & x < R_0 \\ \mathrm{e}^{\lambda/2}\psi\big(\mathrm{e}^{\lambda}(x-R_0)+R_0\big) & x > R_0 \end{cases} \tag{3.24}$$

where for $\lambda \in \mathbb{R}$ there is a rigorous mathematical theory. For the absorber we need $\lambda = \mathrm{i}\theta$, $\theta > 0$.

Scaled operators are naturally defined as $\mathcal{O}^{(\theta)} := U_\theta \mathcal{O} U_\theta^\dagger$, where $U_\theta := U_{\mathrm{i}\theta}^{(R)}$, such that for example potential operators in the scaled region transform as

$$V^{(\theta)}(r) = \big(U_\theta V U_\theta^\dagger\big)(r) = V\big(\mathrm{e}^{\mathrm{i}\theta}(r-R_0)+R_0\big) =: V(r_\theta), \tag{3.25}$$

requiring analytic continuation of V into the complex plane. The following formal manipulations, which can be seen as a computational recipe, give the correct result for the transformed derivative operators in radial direction in the scaled region $r > R_0$:

$$\begin{aligned} \big(\partial_r^{(\theta)}\phi\big)(r) = \big(U_\theta \partial_r U_\theta^\dagger \phi\big)(r) &= U_\theta \partial_r \mathrm{e}^{-\mathrm{i}\theta/2}\phi\big(\mathrm{e}^{-\mathrm{i}\theta}(r-R_0)+R_0\big) \\ &= U_\theta \mathrm{e}^{-\mathrm{i}\theta}\mathrm{e}^{-\mathrm{i}\theta/2}\phi'\big(\mathrm{e}^{-\mathrm{i}\theta}(r-R_0)+R_0\big) \\ &= \mathrm{e}^{-\mathrm{i}\theta}\phi'(r) = \mathrm{e}^{-\mathrm{i}\theta}\big(\partial_r\phi\big)(r). \end{aligned} \tag{3.26}$$

Implementation details

For easy implementation we let the scaling radius R_0 fall onto an element boundary of the finite element discretization of the radial axis. Following the specifications in Ref. [77], we

introduce an explicit discontinuity into the basis functions f_i at the scaling radius R_0:

$$f_i^{(\theta)}(r) = \begin{cases} f_i(r) & r < R_0 \\ \mathrm{e}^{\mathrm{i}\theta/2} f_i(r) & r > R_0. \end{cases} \tag{3.27}$$

If the f_i are purely real, then matrix elements of a complex scaled Operator $\mathcal{O}^{(\theta)}$ can be computed in the scaled region via

$$\langle f_i^{(\theta)} | \mathcal{O}^{(\theta)} f_j^{(\theta)} \rangle_\theta := \int_{R_0}^{\infty} \mathrm{d}r \, f_i^{(\theta)}(r) \big(\mathcal{O}^{(\theta)} f_j^{(\theta)}\big)(r). \tag{3.28}$$

This should be seen as a computational rule which gives correct results in the sense that it implements working absorbing boundary conditions. In particular, overlap matrix and two exemplary terms of the Hamiltonian are given by the following expressions in the scaled region $r > R_0$:

$$\langle f_i^{(\theta)} | f_j^{(\theta)} \rangle_\theta = S_{ij}^{(\theta)} = \int_{R_0}^{\infty} \mathrm{d}r \, \big(\mathrm{e}^{\mathrm{i}\theta/2} f_i\big)(r) \big(\mathrm{e}^{\mathrm{i}\theta/2} f_j\big)(r) = \mathrm{e}^{\mathrm{i}\theta} S_{ij} \tag{3.29}$$

$$\langle \partial_r^{(\theta)} f_i^{(\theta)} | \partial_r^{(\theta)} f_j^{(\theta)} \rangle_\theta = \Delta_{ij}^{(\theta)} = \mathrm{e}^{\mathrm{i}\theta} \int_{R_0}^{\infty} \mathrm{d}r \, \big(\mathrm{e}^{-\mathrm{i}\theta} \partial_r f_i\big)(r) \big(\mathrm{e}^{-\mathrm{i}\theta} \partial_r f_j\big)(r) = \mathrm{e}^{-\mathrm{i}\theta} \Delta_{ij} \tag{3.30}$$

$$\langle f_i^{(\theta)} | V^{(\theta)} f_j^{(\theta)} \rangle_\theta = V_{ij}^{(\theta)} = \mathrm{e}^{\mathrm{i}\theta} \int_{R_0}^{\infty} \mathrm{d}r \, f_i(r) V(r_\theta) f_j(r) \tag{3.31}$$

The implementation of complex scaling thus amounts to simple multiplications of the unscaled matrices with factors of $\mathrm{e}^{\mathrm{i}\theta}$, and evaluation of potential terms at complex values $r_\theta = \mathrm{e}^{\mathrm{i}\theta}(r - R_0) + R_0$.

So far this applies to both standard ECS and infinite range ECS. For the implementation of irECS the discretization formally needs to extend to infinity, which simply means that infinite range basis functions are to be used, an example are the P_n defined in Ref. [77]:

$$P_n(r) = L_n\big(2\alpha(r - R_0)\big)\mathrm{e}^{-\alpha(r-R_0)} \qquad \text{with} \qquad L_n(x) = \frac{\mathrm{e}^x}{n!} \partial_x^n \big(\mathrm{e}^{-x} x^n\big), \tag{3.32}$$

where L_n are the Laguerre polynomials, and $\alpha > 0$ is a free scaling factor. Often, best numerical results are found with $\alpha = 2\theta$ and $\theta \in [0.2, 0.4]$.

3.3 Electron-electron interaction

3.3.1 Multipole Expansion

When solving the TDSE (1.1) numerically for a many-electron system, the electron-electron interaction represents the major computational challenge. It is the only part of the Hamilton operator (1.2) that does not factor into tensor products with respect to the two particles. Using the multipole expansion we can express the matrix connecting the (n_1, n_2) patch with (n_1', n_2') as

$$\begin{aligned} &\langle \Psi^{(n_1' n_2')}_{l_1' m_1' l_2' m_2'} | \frac{1}{|\vec{r}_1 - \vec{r}_2|} | \Psi^{(n_1 n 2)}_{l_1 m_1 l_2 m_2} \rangle \qquad (3.33) \\ = \sum_{\lambda\mu} \frac{4\pi}{2\lambda+1} &\langle Y^{m_1'}_{l_1'} Y^{\mu}_{\lambda} | Y^{m_1}_{l_1} \rangle \langle Y^{m_2'}_{l_2'} | Y^{\mu}_{\lambda} Y^{m_2}_{l_2} \rangle \underbrace{\langle R^{(n_1' n_2')}_{l_1' m_1' l_2' m_2'} | \frac{\min(r_1, r_2)^{\lambda}}{\max(r_1, r_2)^{\lambda+1}} | R^{(n_1 n_2)}_{l_1 m_1 l_2 m_2} \rangle}_{=: \widehat{V}^{(\lambda)}} . \end{aligned}$$

The angular factors are only non-zero if $\mu = m_1 - m_1'$ and $\mu = m_2' - m_2$. For linearly polarized pulses with conserved total angular momentum $m_1 + m_2 = 0$, the two conditions reduce to a single one: $\delta_{\mu, m_1 - m_1'}$. Similar, the sum over λ is automatically truncated by $l_{\max}$: $\lambda_{\max} = 2 l_{\max}$. In practice, one may reduce $\lambda_{\max}$ further. For linearly polarized pulses we found that $\lambda_{\max} \approx 8$ is often enough even when $l_{\max} > 20$ need to be included.

The application of the radial part amounts to a full matrix-vector multiplication on each finite element. For a polynomial expansion of maximal degree $P - 1$ (consisting of P functions) this implies an operations count $\propto P^4$, as opposed to all other operators, which have tensor product structure and therefore an operations count of only $\propto P^3$.

3.3.2 Diagonal transformation

However, as pointed out in Ref. [68], the polynomial basis allows to reduce this scaling to P^3. In fact, the radial multipole matrices $\widehat{V}^{(\lambda)}$, Eq. (3.34), can be exactly represented by a multiplication on an R-point quadrature grid ($R := 2P - 1$) which is independent of λ [6]:

$$\widehat{V}^{(\lambda)} = \left(\widehat{T}^{(n_1)} \otimes \widehat{T}^{(n_2)} \right)^{\mathrm{T}} \widehat{D}^{(\lambda)} \left(\widehat{T}^{(n_1)} \otimes \widehat{T}^{(n_2)} \right). \qquad (3.34)$$

This can be seen as follows:

For fixed angular momentum indices (omitted here) and fixed finite element (n_1, n_2), and inserting the radial basis (Eq. (3.17)) these are given by

$$\widehat{V}^{(\lambda, n_1 n_2)}_{p_1' p_2', p_1 p_2} = \int \mathrm{d}r_1 \int \mathrm{d}r_2 \, \frac{\min(r_1, r_2)^{\lambda}}{\max(r_1, r_2)^{\lambda+1}} f^{(n_1)}_{p_1'}(r_1) f^{(n_2)}_{p_2'}(r_2) f^{(n_1)}_{p_1}(r_1) f^{(n_2)}_{p_2}(r_2). \qquad (3.35)$$

If the maximal degree of the polynomial expansion is $P - 1$, then the product polynomials

$$F^{(n_i)}_{K_i}(r_i) := f^{(n_i)}_{p_i'}(r_i) f^{(n_i)}_{p_i}(r_i), \quad i = 1, 2 \qquad (3.36)$$

have maximal degree $2P-2$, and thus only $2P-1$ out of the P^2 functions $F^{(n_i)}_{K_i}$ are linearly independent. We rearrange the indices $(p'_1p'_2, p_1p_2)$ into new indices $K_1 = (p'_1p_1)$ and $K_2 = (p'_2p_2)$, and consider $\widehat{V}^{(\lambda)}_{p'_1p'_2,p_1p_2}$ as a two-index $P^2 \times P^2$ matrix $\widehat{W}^{(\lambda)}_{K_1,K_2}$. This matrix has a maximal rank of $R := 2P-1$ and, in a suitable representation, it reduces to a $R\times R$ matrix $\widehat{D}^{(\lambda)}_{i,j}$, compare Eq. (3.34). One such representation is with respect to R-point Gaussian quadrature grids: $\{q^{(n_1)}_i\}_{i=1\ldots R}$ with quadrature weights $w^{(n_1)}_i$ on the the interval $[r^{(n_1-1)}_1, r^{(n_1)}_1]$, and $\{q^{(n_2)}_j\}_{j=1\ldots R}$ with weights $w^{(n_2)}_j$ on $[r^{(n_2-1)}_2, r^{(n_2)}_2]$. For these grids we have

$$\widehat{D}^{(\lambda)}_{ij} = \sum_{K_1,K_2} F^{(n_1)}_{K_1}(q^{(n_1)}_i)\widehat{W}^{(\lambda)}_{K_1,K_2}F^{(n_2)}_{K_2}(q^{(n_2)}_j). \tag{3.37}$$

The transformation from the P^2 coefficients to the $R < P^2$ coefficients can be done separately for each coordinate, i.e. it has tensor product structure and operations count $RP(R+P) \propto P^3$. It is given by $\widehat{T}^{(n_1)} \otimes \widehat{T}^{(n_2)}$ with

$$\widehat{T}^{(n_1)}_{i,p_1} = \sqrt{w^{(n_1)}_i} f^{(n_1)}_{p_1}(q^{(n_1)}_i), \quad \widehat{T}^{(n_2)}_{j,p_2} = \sqrt{w^{(n_2)}_j} f^{(n_2)}_{p_2}(q^{(n_2)}_j). \tag{3.38}$$

Thus, the application of $\widehat{V}^{(\lambda)}_{p'_1p'_2,p_1p_2}$ amounts to a transformation to the reduced representation with R coefficients, the coefficient-wise multiplication with $\widehat{D}^{(\lambda)}_{ij}$ (operations count R^2), and the back-transformation to the representation with P^2 coefficients:

$$\widehat{V}^{(\lambda,n_1n_2)}_{p'_1p'_2,p_1p_2} = \left(\widehat{T}^{(n_1)}_{i,p'_1} \otimes \widehat{T}^{(n_2)}_{j,p'_2}\right)^{\mathrm{T}} \widehat{D}^{(\lambda)}_{i,j} \left(\widehat{T}^{(n_1)}_{i,p_1} \otimes \widehat{T}^{(n_2)}_{j,p_2}\right), \tag{3.39}$$

compare Eq. (3.34).

The integrals for generating the correct $\widehat{D}^{(\lambda)}_{ij}$, Eq. (3.37), need to be evaluated once exactly during setup. This step must not be bypassed by using $\min(q_i,q_j)^\lambda / \max(q_i,q_j)^{\lambda+1}$, as this potential is not suitable for direct integration with a Gaussian quadrature on the product grid q_iq_j.

In practice, we found that the quadratures do not need to be done exactly. Minor quadrature errors introduced by a Gaussian quadrature grid with only P or even fewer points are acceptable, which further reduces the operations count.

It is obvious from the derivation, that the same procedure can be applied for any two-dimensional multiplication potential and gives the exact matrix elements for a given polynomial product basis. It is most useful for potentials that have points of non-analyticity, such as the Coulomb potential. For potentials with a convergent Taylor series, Gaussian quadrature can be usually applied directly.

3.3.3 Special case: FE-DVR

In the current implementation we follow the description from Ref. [68] with a slightly modified discrete variable representation. In particular, on the n-th finite element $[r_{n-1}, r_n]$

(which is equipped with p_n Legendre functions, see Sec. 3.1.1.3) we define q_n Lagrange interpolating polynomials

$$\chi_i^{(n)} = \prod_{j=0, j\neq i}^{q_n-1} \frac{x - x_j^{(n)}}{x_i^{(n)} - x_j^{(n)}} \mathbb{1}_{[x_{n-1}, x_n]} \qquad i \in \{0, 1 \ldots, q_n - 1\} \tag{3.40}$$

where the $x_i^{(n)}$ are the Gauss-Lobatto quadrature points on the n-th interval. The $w_i^{(n)}$ are the corresponding weights. We have

$$\begin{aligned} \chi_i^{(n)}(x_j^{(m)}) &= \delta_{nm}\delta_{ij} \\ \langle \chi_i^{(n)} | \chi_j^{(m)} \rangle &= \int \chi_i^{(n)} \chi_j^{(m)} = \delta_{nm} \sum_k w_k^{(n)} \chi_i^{(n)}(x_k^{(n)}) \chi_j^{(n)}(x_k^{(n)}) = \delta_{nm}\delta_{ij} w_i^{(n)} \end{aligned}$$

and omitting the interval index (for notational brevity):

$$\big(\partial_x \chi_i\big)(x_j) = \begin{cases} \frac{1}{x_i - x_j} \prod_{k\neq i,j} \frac{x_j - x_k}{x_i - x_k} & \text{for } i \neq j \\ \frac{1}{2w_i}(\delta_{i,q_n-1} - \delta_{i,0}) & \text{for } i = j. \end{cases} \tag{3.41}$$

The Gauss-Lobatto quadrature grid includes the two endpoints of the interval. The key property $\chi_i(x_j) = \delta_{ij}$ can only be satisfied if the maximum order of the functions and the number of quadrature points match. Therefore we introduce a quadrature error, which was found to be acceptable.

Transformation from the n-th interval $[r_{n-1}, r_n]$ with its p_n Legendre polynomials f_i to q_n DVR basis functions χ_i is done via

$$|f_i\rangle = \sum_j |\chi_j\rangle w_j^{-1} \langle \chi_j | f_i \rangle \tag{3.42}$$

where the w_j^{-1} comes from the non-normality of the χ_i (which is the missing $\sqrt{w_i}$ compared to the definition in Ref. [68]. We need the extra inverse in the transformation, but we do not need bridging functions to ensure continuity.) We absorb the factor into the transformation matrix $\widehat{T}$

$$\widehat{T}_{ji}^{(n)} = w_j^{-1} \langle \chi_j | f_i \rangle = w_j^{-1} \sum_k w_k \chi_j(x_k) f_i(x_k) = f_i(x_j). \tag{3.43}$$

The diagonal matrix $\widehat{D}^{(\lambda)}$ is given by

$$\widehat{D}_{ji}^{(\lambda)} = \Big(\frac{(2\lambda+1) w_i w_j}{r_i r_j} K_{ji}^{(\lambda)-1} + \frac{r_i^\lambda r_j^\lambda}{r_s^{2\lambda+1}} w_i w_j \Big) \tag{3.44}$$

with [68]

$$K_{nm}^{(\lambda)} = -\langle \chi_n | \partial_r^2 - \frac{\lambda(\lambda+1)}{r^2} | \chi_m \rangle. \tag{3.45}$$

3.4 tRecX code structure: Recursive indexing

For given choice of discretization $\{f_i\}$, the TDSE (1.1) becomes a coupled system of ordinary differential equations (3.2). The solution requires the setup of the matrices $\widehat{S}_{ij} = \langle f_i|f_j\rangle$ and $\widehat{H}_{ij}(t) = \langle f_i|H(t)|f_j\rangle$ with the Hamilton operator $H(t)$, and the time propagation of the system starting from some initial state until after the end of the time-dependence of $H(t)$. These steps are automatized by our tRecX code.

The tRecX code [83] (**t**ime-dependent **rec**ursive inde**x**ing) is a general partial differential equation (PDE) solver package. It provides various interfaces for inputing the dynamical equations (in our case, the TDSE (1.1)) and the desired basis sets. It then automatically converts the operators of the PDE into corresponding matrices with respect to the given basis, and sets up an efficient and parallelizable matrix-vector multiplication algorithm which takes into account block structure and avoids multiplications wherever possible, currently optimized for the application to the TDSE including a strong external laser field. This is of key relevance, as any algorithm for the most time consuming part - time propagation - eventually reduces to repeated matrix-vector applications. On the lowest level the code employs optimized small scale matrix-vector multiplication routines from the EIGEN [84] library. For the small matrices (100×100 or smaller) appearing as non-zero blocks in the overall matrices of the problems considered in this thesis, EIGEN is extremely efficient and beats the most prominent alternatives, as demonstrated on their benchmark webpage.

The code wraps several other powerful linear algebra packages for maximum efficiency. In particular, ARPACK [85] provides Arnoldi iteration [86] algorithms, and ALGLIB [87] supplies efficient general integrators. Further, parallelization is implemented via open-MPI [88], and of course BOOST [89] is used ubiquitously for various purposes including shared memory communication.

At the heart of the tRecX code lies a design pattern which is known as the "composite pattern" [90], used to build up index structures. Thereby, a class object of type INDEX has the property to contain other INDEX objects, which in turn again contain INDEX objects until finally a FLOOR INDEX is reached. This recursive design allows for full flexibility in the construction of different index trees, as illustrated in figure 3.3.

This recursive indexing scheme is not only useful from a software design perspective, but it also allows for simple translation of the mathematical representation of a basis into its implementation. A basis, such as our single particle angular basis $\psi(r,\Omega,t) = \sum_{m=-m_{\max}}^{m_{\max}} \sum_{l=|m|}^{l_{\max}} Y_l^m(\Omega) R_{lm}(r,t)$, Eq. (3.3), naturally introduces an index hierarchy ($m \to l$) with varying number of subindices (here $l_{\min} = |m|$ depends on m). This can be directly mapped to a corresponding tree structure, and in this sense tRecX provides an easy to use interface for inputing the basis.

Coefficient vectors and matrices are then automatically constructed using the given index tree as a template. The code implements efficient handling of continuity in finite element basis sets and resulting low rank corrections in the inverse overlap, which are discussed in appendix 8.6. Parallelization (see Sec. 3.5.4) of linear algebra operations is naturally carried out by distributing subtrees along the available processes. As the basis

is chosen such that most operators are either diagonal or only connect neighboring indices (see for example Sec. 3.1.1.1), this automatically leads to communication mostly between nearby processes with shared memory, which reduces the amount of the comparably slow inter-node communication via network (InfiniBand).

All the key methods for efficient computation of photo-electron spectra are implemented in the code, in particular irECS (Sec. 3.2) and tSurff (chapter 2).

The following sections describe in detail some of the key techniques and algorithms employed in the code for efficient time propagation.

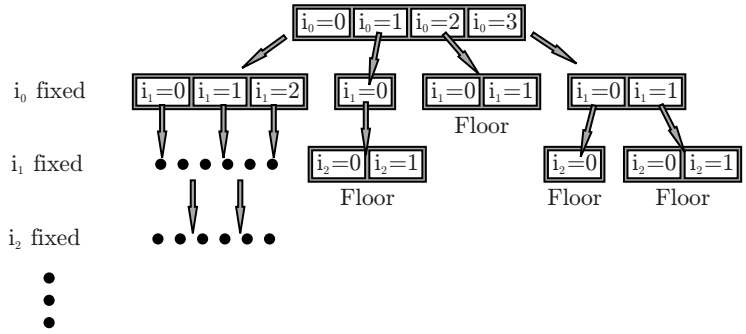

Figure 3.3: Visualization of the recursive index structure. On each level an additional index of the hierarchy is fixed. Coefficient vectors and matrices are build up following such an index tree. On the respective floor level all relevant information is stored, e.g. the actual coefficients, the concrete basis functions used for the discretization or the matrix block corresponding to this set of indices.

3.5 Time propagation

The numerical solution of ordinary differential equations as in Eq. (3.2) can be obtained with a wide variety of algorithms. Within the current framework of the tRecX code, any algorithm which reduces to a repeated application of the inverse overlap and Hamiltonian matrices on a coefficient vector can be implemented easily. The family of Runge Kutta solvers satisfies this property, and our choice as time propagator is the classical Runge Kutta 4 algorithm.

Other time propagators have been applied in the literature. For example, in the context of the computationally challenging two-electron computations, the short iterative Lanczos method [91] was used in Ref. [27], the real-space-product algorithm [92] in Ref. [31], and a Crank-Nicolson method in Ref. [68]. Earlier experiments with several integrators indicated no significant change in efficiency or accuracy. However, these were not performed in the current framework and there may well be room for optimization.

3.5.1 Adaptive step size control

Step size control is important as at long wavelength, depending on intensity, the time evolution can be driven by the external field and strongly vary with the strength of the vector potential $|\vec{A}(t)|$. Thus, an automatically adjusted step size leads to better convergence properties. We use step doubling [93]. Thereby each time step is repeated by doing two steps with half the step size. Then the two results are compared, and their difference ϵ decides if the steps are accepted or need to be discarded and repeated with a smaller step size. The new step size h is determined by

$$h \to h \cdot \left(\frac{\epsilon_0}{\epsilon}\right)^{\frac{1}{5}} \tag{3.46}$$

where ϵ_0 is the maximally admissible error which determines the precision of the time propagator. In order not to discard too many steps, the condition is usually weakened to $\epsilon \overset{!}{<} s\epsilon_0$ with safety factor s around 1.5. The error ϵ may be computed with any norm. We chose the l_∞-norm on the coefficient vector (see Eq. (3.1)) for convenience:

$$\epsilon(\psi, \varphi) := \max_{n=1\ldots N_{\text{coef}}} |c_n^\psi - c_n^\varphi|. \tag{3.47}$$

Larger ϵ_0 will result in larger step sizes. In figure 3.4 the step size during time propagation is shown for various ϵ_0.

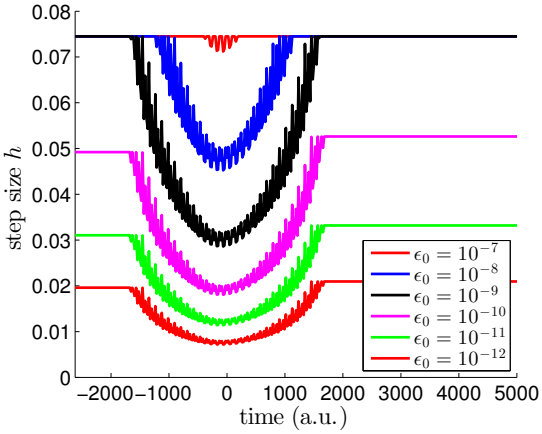

Figure 3.4: Step size h (in a.u.) of the Runge Kutta 4 propagator as a function of time. The chosen laser pulse is present for times $t \in [-2000, 2000]$ a.u.. At times where the laser pulse dominates the system's dynamics, the step size is reduced by condition (3.46) automatically, preventing the error ϵ from becoming larger than the admissible error ϵ_0. The step size was not allowed to exceed $h_{\max} \approx 0.075$ in this case.

3.5.2 High energy projectors

Depending on the discretization, the TDSE (3.2) may exhibit stiffness. This is the case when the radial grid point density is high because then large momenta can be resolved, which implies that the Hamiltonian matrix $\widehat{H}(t)$ has both very large and small eigenvalues.

However, the highest eigenvalues often do not contribute relevantly to the dynamics, and it is possible to project them out explicitly without altering the physics. In principle the eigenvalues of the Hamiltonian matrix $\widehat{H}(t)$ are time-dependent due to the external laser field. For not too large laser intensities the highest eigenvalues are however dominated by the kinetic energy term, and the corresponding eigenvectors are approximately time-independent and equal to those of the field free Hamiltonian $\widehat{H}_0$.

After complex scaling the normalized eigenvectors $|\phi_i\rangle$ of $\widehat{H}_0$ are mutually orthogonal [94, 95] in the sense

$$\langle \phi^{(i)*} | \phi^{(j)} \rangle = \int \mathrm{d}\vec{r}\, \phi^{(i)}(\vec{r}) \phi^{(j)}(\vec{r}) = \delta_{ij}. \tag{3.48}$$

Therefore it is possible to project out the components of the wavefunction into specific eigendirections of the field free Hamiltonian by defining the projector

$$\widehat{Q} = \widehat{\mathbb{1}} - \sum_i \widehat{P}_i = \widehat{\mathbb{1}} - \sum_i |\phi^{(i)}\rangle\langle\phi^{(i)*}|. \tag{3.49}$$

The sum runs over all those eigenvectors corresponding to eigenvalues which are to be projected out. For our application, this applies to eigenvalues satisfying the condition

$$\widehat{H}_0 |\phi^{(i)}\rangle = E_i |\phi^{(i)}\rangle \qquad \text{with } E_i \geq E_{\text{threshold}} \tag{3.50}$$

for some threshold energy $E_{\text{threshold}} \gg 0$. This means we solve the modified Schrödinger equation

$$\dot{\vec{c}} = -\mathrm{i}\widehat{Q}\widehat{S}^{-1}\widehat{H}\vec{c}. \tag{3.51}$$

Figure 3.5 shows how the step size changes with $E_{\text{threshold}}$. As the step size increases, more and more high energetic eigenvalues are taken out of the systems dynamics. Interestingly, this also leads to changes in the variance of the step size, which was not investigated further. Thus, from a computational point of view, $E_{\text{threshold}}$ is to be chosen as small as possible. At some point however, the projector starts to actually modify dynamics. For high laser intensities, it may be impossible to project out any eigenvectors during the presence of the field, as the field free eigenstates may become too different from the eigenstates of the Hamiltonian including the laser field.

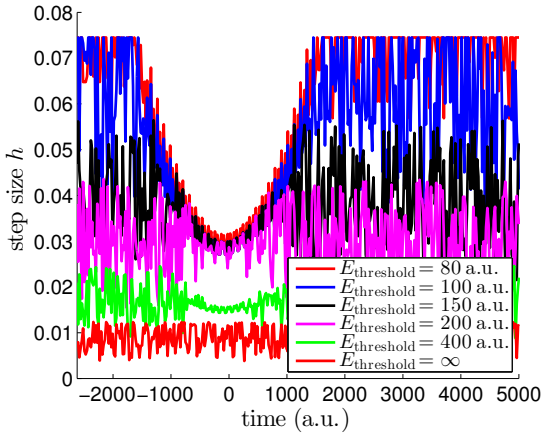

Figure 3.5: Effect of the high energy projectors on the step size of the self adaptive Runge Kutta 4 algorithm. During the laser pulse $t \in [-2000, 2000]$ a.u., the step size is determined by laser induced dynamics. It can be seen, that with decreasing threshold energy $E_{\text{threshold}}$ the step size increases, as less and less high energy eigenvectors are accessible to the system's dynamics. The step size was not allowed to exceed $h_{\max} \approx 0.075$. Note that the graphs in Fig. 3.4 were all computed with $E_{\text{threshold}} = 50$ a.u..

3.5.3 Initial state

Several specific eigenstates of the Hamiltonian matrix are required by our applied algorithms. The TDSE (3.2) needs to be solved with initial state $\psi(t = t_0) = \psi_0$, which in our case was always the field free ground state satisfying

$$E_0 = \langle\psi_0|H_0|\psi_0\rangle = \min_{\|\psi\|=1} \langle\psi|H_0|\psi\rangle. \tag{3.52}$$

The computation of the single emission spectra according to Eq. (2.62) requires ionic bound states, and the projectors for high energetic components of the discretization (Sec. 3.5.2) require the eigenvectors corresponding to the highest eigenvalues.

All of these eigenstates can be efficiently found using an Arnoldi iteration [86], which escapes the need to diagonalize the full matrix, which would represent a daunting task for the larger systems.

3.5.4 Parallelization scheme and scaling

We now demonstrate the parallelization scheme for the two particle problem, where the wavefunction is discretized as

$$\Psi(\vec{r}_1,\vec{r}_2,t)=\sum_{m_1m_2}^{m_{\max}}\sum_{l_1l_2}^{l_{\max}}\sum_{n_1n_2}^{N}\sum_{k_1k_2}^{p_{n_{1/2}}} Y_{l_1}^{m_1}(\Omega_1)Y_{l_2}^{m_2}(\Omega_2)f_{k_1}^{(n_1)}(r_1)f_{k_2}^{(n_2)}(r_2)c_{m_1l_1k_1m_2l_2k_2}^{(n_1n_2)}(t). \quad (3.53)$$

This discretization naturally introduces two distinct parallelization directions: In the directions of angular momenta (m_1, m_2, l_1, l_2) there is broad band communication, which is most efficient on shared memory machines. Due to the high-order finite element discretization, the n_1 and n_2 directions involve only nearest neighbor communication, which is easily handled by the InfiniBand technology between nodes (see Fig. 3.6).

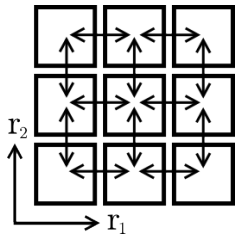

Figure 3.6: The finite element discretization divides space into patches which are only connected to direct neighbors.

By using low-rank updates via an adapted Woodbury formula (appendix 8.6) for the implementation of the inverse overlap, its application also requires communication of element boundary values only (2 out of p_n coefficients). The communication does however involve all-to-all communications, which do not scale very efficiently.

The scaling of the computation time with the number of processes for small problem sizes is shown in figure 3.7.

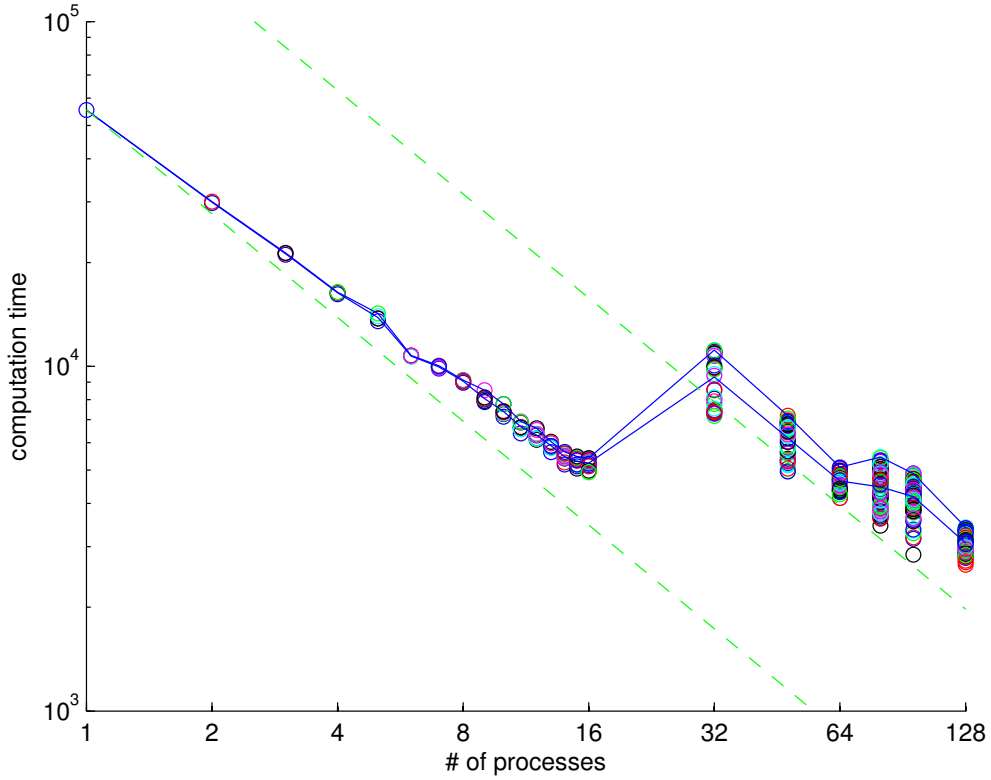

Figure 3.7: Scaling of the computation time T with the number of processes N. For each process a circle marks its computing time (non-idle time). The total time of the entire computation is determined by the slowest process. The spread in computing time indicates non-optimal workload distribution. Blue lines mark average and longest computing times of a single process. Green dashed lines represent perfect scaling behavior $T \propto N^{-1}$. The jump from 16 to 32 cores is due to inter-node communication via InfiniBand (the cluster on which these computations were performed consists of nodes with 16 CPU's). The here used problem size is too small for an efficient use of more than 16 computing cores.

The current implementation of the parallelization algorithms is not well suited to be used on more than 8 nodes when realistic problems are considered. If the problem is tailored to the parallelization scheme, then also much larger systems scale efficiently, as can be seen in Fig. 3.8.

The culprit for non-perfect scaling is the inverse of the overlap operator $\widehat{S}^{-1}$, see Fig. 3.9. Its application only involves little communication, but of an all-to-all nature.

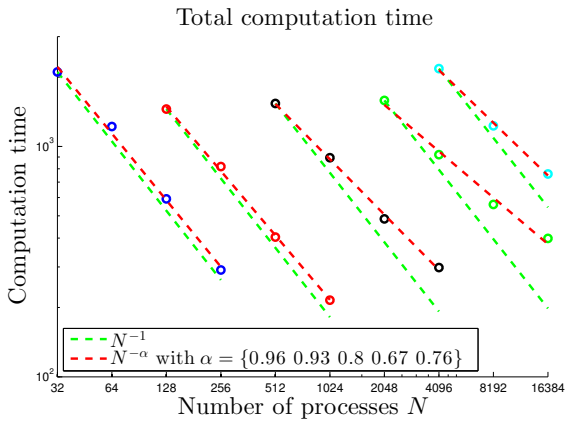

Figure 3.8: Total computation time T versus number of processes N. A given set of computations (circles sharing color) only differ in the number of processes, different sets have different problem sizes. Green dashed lines indicate perfect scaling $T \propto N^{-1}$, red dashed lines are interpolated scaling laws $T \propto N^{-\alpha}$ with exponent α given in the legend. It can be seen that moderate scaling behavior is achieved for up to $2^{14} = 16384$ processes.

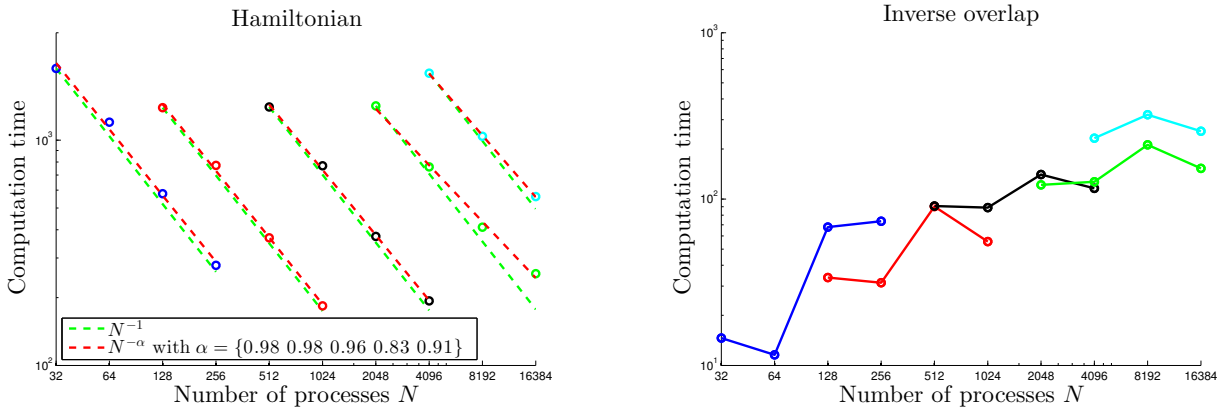

Figure 3.9: Computation time T versus number of processes N. A given set of computations (circles sharing color) only differ in the number of processes, different sets have different problem sizes. Left: The Hamiltonian part (see Eq. (3.2)) gives the main contribution and shows near perfect scaling. Green dashed lines indicate perfect scaling $T \sim N^{-1}$, red dashed lines are interpolated scaling laws $T \sim N^{-\alpha}$ with exponent α given in the legend. Right: The inverse overlap part (including nearly all-to-all communication) does not scale, and is responsible for the non-perfect scaling of the total computation time. As soon as the Hamiltonian computation time drops to the level of the inverse overlap computation time, there is no further gain when adding more processes. The lines connecting the circles are just to help identify a set of computations with constant problem size.

3.6 Determining convergence

The numerical solution of any problem always requires a check for convergence. The translation of the partial differential equation into a set of ordinary differential equations described at the beginning of this chapter truncates the solution space. Simply put, if the chosen basis leaves out an important part of the Hilbert space, then the solution of the discretized TDSE (3.2) can look very different from the solution of the un-discretized TDSE (1.1). Obviously, the size and shape of the chosen basis needs to be converged, as resulting observables should not depend on details of the basis. Explicitly, the following parameters determine our basis:

- Sizes of the angular momentum expansions (3.3) and (3.14): $l_{\max}$ and $m_{\max}$.
- Numbers N and orders p_n of the finite element discretizations (3.13) and (3.17), as well as their domains $[r_{n-1}, r_n]$.
- For the electron-electron interaction, see Sec. 3.3: the highest $\lambda_{\max}$ for the multipole expansion (3.34) and the Lobatto orders q_n in Eq. (3.40).

Our absorber irECS (section 3.2) introduces:

- The scaling angle θ and the scaling radius R_0.

The numerical time propagation (section 3.5) of equation (3.2) depends on:

- The maximally admissible error ϵ_0.
- The threshold for the high energy projectors $E_{\text{threshold}}$.

Additionally, we are computing photo-electron spectra using the tSurff method described in the next chapter 2. It introduces several additional convergence parameters, for which we choose a few dependent on the box size R_0, see Sec. 4.1.1. The remaining parameters are:

- The end of time propagation T, Eq. (2.11).
- The beginning a of the truncation interval of the Coulomb potentials $[a, R_0]$, Eq. (2.19).

All of the above parameters need to be converged until the solution loses all dependencies on them. At several points in this thesis we will demonstrate convergence with respect to some of these parameters explicitly, which will always imply that all other parameters are already converged. In practice, one often relies on the assumption that variations in the high dimensional convergence parameter space can be done independently in all directions. Because this is not always the case, good practice dictates to verify this assertion in each case independently.

3.7 Comment on gauges

For gauges in quantum mechanics the naming "gauge" originates in Maxwell's equations and refers to redundant degrees of freedom in the Lagrangian of Electrodynamics. There, a gauge transformation is a transformation applied solely to the fields with the property that the transformed fields are still a solution of the (untransformed) Maxwell equations. In quantum mechanics such a gauge transformation translates into a time and space dependent unitary transformation U_g of both the wavefunction and the operators, see Ref. [3]. In summary, the transformation

$$U_g = \mathrm{e}^{\mathrm{i}g(\vec{r},t)} \tag{3.54}$$

applied on the wavefunction ψ

$$\psi \quad \rightarrow \quad \psi_g = U_g \psi \tag{3.55}$$

and the operators $\mathcal{O}$

$$\mathcal{O} \rightarrow \mathcal{O}_g = U_g \mathcal{O} U_g^* \tag{3.56}$$

including the time derivative operator

$$\partial_t \rightarrow \partial_t - \mathrm{i}\dot{g} \tag{3.57}$$

leads to a transformed TDSE, which encodes exactly the same dynamics.

One of the most popular gauges is "length gauge", where the dipole operator for the external laser pulse with electric field $\vec{E}(t)$ takes the form $\vec{E}(t) \cdot \vec{r}$. The TDSE in length gauge is

$$\mathrm{i}\partial_t \psi_{\mathrm{L}}(\vec{r},t) = \Big(-\frac{\Delta}{2} + \vec{E}\cdot\vec{r} + V(\vec{r}) \Big) \psi_{\mathrm{L}}(\vec{r},t). \tag{3.58}$$

With

$$U_{\mathrm{L}\rightarrow\mathrm{V}} := \mathrm{e}^{-\mathrm{i}\vec{A}(t)\vec{r}} \mathrm{e}^{-\frac{\mathrm{i}}{2}\int_{-\infty}^{t} \mathrm{d}\tau\, \vec{A}^2(\tau)} \tag{3.59}$$

the length gauge TDSE can be transformed into another popular gauge, the so-called "velocity gauge":

$$\mathrm{i}\partial_t \psi_{\mathrm{V}}(\vec{r},t) = \Big(-\frac{\Delta}{2} - \mathrm{i}\vec{A}(t)\cdot\vec{\nabla} + V(\vec{r}) \Big) \psi_{\mathrm{V}}(\vec{r},t) \tag{3.60}$$

with the vector potential of the electric field $\vec{A}(t) := -\int_{-\infty}^{t} \mathrm{d}\tau\, \vec{E}(\tau)$.

As explained in Ref. [3], while length gauge lends itself to intuitive interpretation and modeling, velocity gauge performs better in numerical calculations [81]. Fewer discretization coefficients can be used and the stiffness of the equations is reduced. This is due to the dynamics of free electrons in the field. For a free electron the velocity gauge canonical momentum is conserved. In contrast, in length gauge, momenta are boosted by $\vec{A}(t)$, reflecting the actual acceleration of the electron in the field. As large momenta correspond to short range modulations of the solution, length gauge requires finer spatial resolution than velocity gauge. This modulation affects numerical efficiency, when the variation of $\vec{A}(t)$ is comparable or exceeds the momenta occurring in the field-free system.

In addition, our choice of absorber (section 3.2) does not work in length gauge, but in velocity gauge. Therefore, most numerical computations presented in this thesis were conducted in velocity gauge.

In Sec. 5.1 however we will present a restricted multi-electron basis, in which all but one electrons are restricted to field-free bound states. As these conserve their meaning only in length gauge, we will require a gauge which mixes properties of length and velocity gauge. Bound states are, by definition, confined to moderate distances, whereas the effect of momentum boosts are most relevant for free electrons, usually far from the bound states. Using length gauge within the reach of bound states and velocity gauge otherwise largely unites the advantages of both gauges: Locally, the system can be modeled intuitively, while at the same time maintaining efficient numerical spatial discretization and asymptotics suitable for absorption by irECS.

This "mixed gauge" is achieved with

$$U_{\mathrm{L}\to\mathrm{M}} := \begin{cases} 1 & \text{for } r < R_c \\ \mathrm{e}^{-\mathrm{i}\vec{A}(t)\vec{r}(r-R_c)/r}\mathrm{e}^{-\frac{\mathrm{i}}{2}\int_{-\infty}^{t}\mathrm{d}\tau\,\vec{A}^2(\tau)} & \text{for } r > R_c \end{cases} \tag{3.61}$$

and in Ref. [3] we demonstrate how the resulting mixed gauge TDSE bears substantial numerical advantages and requires only moderate implementation effort. The transition between length and velocity gauge within the same calculation allows for the implementation of physically motivated restricted basis sets and thereby opens the route to a highly efficient coupled channels type description of laser matter interaction, see Sec. 5.1.

3.8 Computational resources

The highly efficient tSurff method (chapter 2) for computing photo-electron spectra, together with techniques like irECS (Sec. 3.2) or FE-DVR (Sec. 3.3.3) and an efficient implementation (Sec. 3.4), lead to a drastically reduced demand on computational resources in comparison to results reported in the literature.

In Sec. 4.1.3 this becomes apparent for a single-electron system and an elliptically polarized laser pulse. Here computations employing standard approaches represent a significant effort, but with tSurff these are routine calculations on single workstation sized machines.

The true might of tSurff however unfolds when double ionization processes are of interest, treated in chapter 6. Even then, computations can be performed on the workstation scale, at least at XUV wavelengths. For example, on a 16 core shared memory machine the computation of the two-photon double ionization cross section presented in Sec. 6.3.2 took about 12 hours with $R_c = 30\,\mathrm{a.u.}$ and about 60 hours with $R_c = 80\,\mathrm{a.u.}$ for each photon energy. Resource requirements are not significantly increased by the addition of a weak IR field as in Sec. 6.4.1: With a total of 551 partial waves on a 16 core machine, the largest computation with $R_c = 25$ ran for a maximum of two days.

Computations at strong IR fields are the most challenging. Yet, the largest of the computations reported in Sec. 6.4.2 used 128 cores, running for 10 days for solving the full two-electron problem on domain B, see Sec. 2.2.3. Additional 5 days were required to compute the solutions on domain S for a $\vec{k}_1$-$\vec{k}_2$-grid dense enough for extraction of the fully differential data. This should be put into relation to the much larger computing facilities employed in the direct approaches. For example, 4000 cores were used for each computation including only 295 partial waves in Ref. [31] (no run times are quoted). Resource consumption was not reported in Refs. [27, 29, 70, 74, 75], but in all cases computations were performed at supercomputing centers using large scale machines.

Chapter 4

Single-electron systems

We now present results for the Hydrogen atom and for a single-electron effective potential of the Helium atom. Single-electron systems are in general easy to treat numerically due to their low dimensionality. Already for two-electron systems the "curse of dimensions" renders many problems intractable. For the full numerical solution of the time-dependent Schrödinger equation (TDSE), the Hydrogen atom often plays the role of a benchmark system due to its simplicity.

This chapter focuses on large laser wavelengths where ionization is well described by the tunneling picture, see Sec. 1.4.3: The nuclear potential and the electric field together form a potential barrier for the electron to tunnel through. The tunnel probability exponentially depends on the electric field strength $E(t)$, see Eq. (1.9), implying dominant contributions to the spectrum at times where the field strength is maximal. In the next chapter also photo-electron spectra resulting from short wavelength laser pulses will be presented.

4.1 Hydrogen

4.1.1 Linearly polarized fields - tSurff convergence behavior

In this section we consider a Hydrogen atom in a linearly polarized infrared laser field and present photo-electron spectra. Our approach for the numerical computation of these spectra includes the irECS (see Sec. 3.2) and tSurff (see chapter 2) techniques. For the following four convergence parameters we now study their behavior explicitly: The box size R_0 (given by the start of the absorption domain), the tSurff radius R_c for wavefunction flux integration, and the beginning and end points of the Coulomb potential truncation interval $[a, b]$, Eq. (2.19). In Sec. 2.1.4 we already argued that choosing b equal to R_c is best from a convergence point of view, Eq. (2.21). In the following we demonstrate this explicitly and conjecture that the choice $R_0 = R_c = b$ is best, and that convergence is achieved quickest by increasing all three parameters together.

A linearly polarized field is described by the vector potential

$$\vec{A}(t) \propto \sin(\omega t)\mathcal{E}(t) \tag{4.1}$$

with carrier frequency ω and pulse envelope $\mathcal{E}(t) \geq 0$. The electric field is given by $\vec{E}(t) = -\partial_t \vec{A}(t)$. Bursts of ionization in alternating directions are emitted every half cycle when the electric field has a maximum. Except for short pulse effects these instants $t_{\max}$ coincide with zeros of the vector potential. If further Coulomb interactions are neglected the final photo-electron momenta are then given by

$$\vec{p} = -\vec{A}(t_{\max}), \tag{4.2}$$

implying maximum ionization probability at photo-electron energy $E = 0$. According to the three step model (Sec. 1.4.4), recollisions during the pulse can trigger a variety of effects, including high harmonic generation, self interference or further ionization in case of multi-electron systems. Without recollisions, the maximum energy an electron can acquire according to the tunneling picture is $2\,U_p$, while electrons rescattering with the nucleus may reach energies up to $\approx 10\,U_p$, see Sec. 1.4.5. These threshold values are most pronounced for Keldysh parameters $\gamma \ll 1$ where the tunneling picture is most accurate, i.e for large laser wavelengths and intensities. In Fig. 4.1 we present the photo-electron spectrum of a few cycle 1600 nm pulse with $\gamma = 0.5$, which qualifies as "$\gamma \ll 1$".

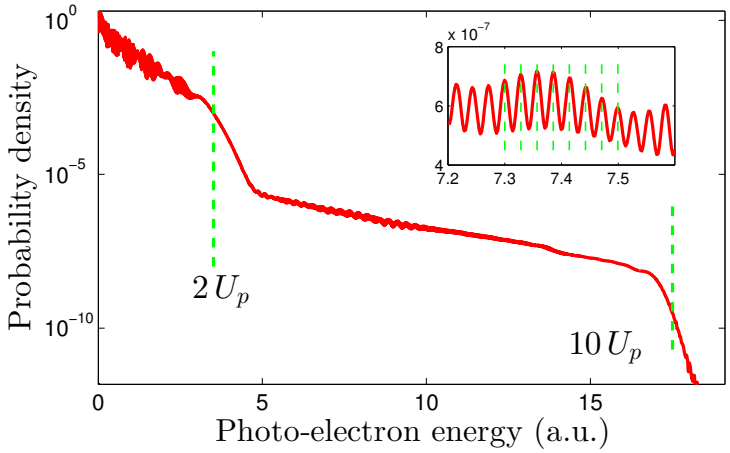

Figure 4.1: Photo-electron spectrum ($P(E)$ in Eq. (3.8)) of a few cycle 1600 nm pulse of intensity $2 \cdot 10^{14}$ W/cm^2 (exact pulse shape: $n = 3$, $m = 8$ in Eq. (8.26)). Clearly visible are the exponential decays at $E = 2\,U_p$ (above which rescattering is requisite), and at $E = 10\,U_p$ (which marks the maximum energy an electron can acquire even with recollision). Also shown in the inset are the above threshold ionization (ATI) peaks, separated by the photon energy $\hbar\omega \approx 0.03$ a.u.. Convergence for these laser parameters required $l_{\max} = 130$, $R_0 = 120$ a.u. and a radial discretization with 48 finite elements of order 15.

Choosing R_0: The quiver amplitude of the electrons in the laser field used for Fig. 4.1 is $r_q \approx 93$ a.u.. Computing this spectrum with the tSurff method we may choose any R_c, also allowing box sizes R_0 even below r_q. The crucial point is that rescattering paths leading

through the absorption region must still be represented correctly, which can always be achieved by improving the discretization in the absorption region.

In figure 4.2 we quantify how for decreasing R_0 an increasing number of radial coefficients N_{absorb} in the absorption region is required for converged results. Thereby we take $b = R_c = 60\,\text{a.u.}$ and convergence with N_{absorb} is determined such that the relative error between the spectra of a fully converged computation P_c (with $R_0 = 120\,\text{a.u.}$) and a smaller computation P_x does not exceed 10%: $\max_{E \leq 10\,U_p} \left| \frac{P_x(E) - P_c(E)}{P_c(E)} \right| \overset{!}{\leq} 0.1$.

It can be seen that for the given laser parameters the required number of radial absorption coefficients N_{absorb} is approximately constant for $R_0 > r_q$. As R_0 is moved below the quiver radius $r_q \approx 93\,\text{a.u.}$, quickly growing N_{absorb} become necessary to correctly represent rescattering dynamics. For $R_0 < r_q$ the increasing demand on N_{absorb} in this case exceeds the reduction of discretization coefficients in the non-absorbing region $r < R_0$. This is a general behavior at small Keldysh parameters $\gamma \ll 1$.

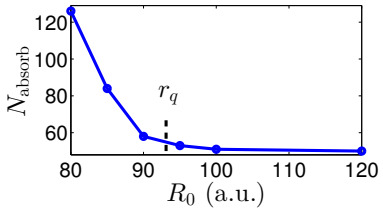

Figure 4.2: The number N_{absorb} of radial coefficients in the absorption domain required for convergence of photo-electron spectra quickly increases for $R_0 < r_q$.

Other observables behave differently. Suppose that only the total yield is of interest. This quantity is only very weakly affected by recollision dynamics, and a much smaller box size R_0 (with significantly smaller N_{absorb} than indicated in Fig. 4.2) suffices for converged results.

Choosing R_c: For fixed $R_0 = 120\,\text{a.u.}$ and leaving $b = 60\,\text{a.u.}$ we may compute the spectrum using any tSurff radius R_c for wavefunction flux integration satisfying $b \leq R_c \leq R_0$. Apart from slight dependencies on the end of time propagation T and Rydberg states artifacts (see Sec. 2.1.4), the resulting photo electron spectra are independent of R_c. This simply means that the free propagation in the laser field for $r \in [b, R_0]$ is correctly reproduced by the numerical computation, as it agrees with the fully analytic expression that is used in the tSurff method, Eq. (2.15).

Choosing b: Thus, we may choose $R_c = R_0$, which in turn allows us to increase b up to 120 a.u. without increasing the numerical demand. The dependence of the spectrum on the truncation interval $[a, b]$ is shown in Fig. 4.3.

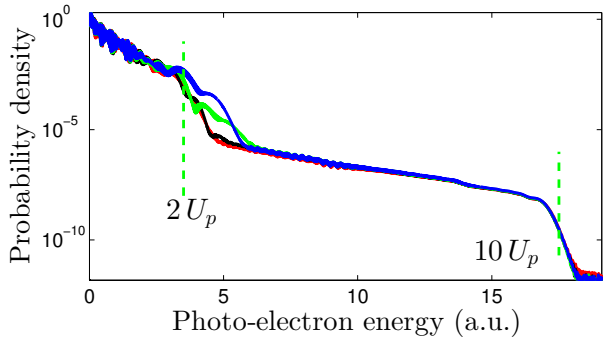

Figure 4.3: Computations with fixed $R_c = R_0 = 120\,\text{a.u.}$ for various truncation intervals, Eq. (2.19): $[a, b] = [80, 120]\,\text{a.u.}$ (red), $[18, 25]\,\text{a.u.}$ (black), $[16, 20]\,\text{a.u.}$ (green), $[12, 15]\,\text{a.u.}$ (blue). Same pulse parameters as in Fig. 4.1. It can be seen that spectra converge as the truncation interval is moved to larger values such that the resulting potential approaches the true Coulomb form.

We conclude that for given box size R_0 it is best to have $b = R_0$, and therefore also $R_c = R_0$. Note, that when neglecting Coulomb tails starting from $b = 25\,\text{a.u.}$ deviations in the total spectrum are already small. Even for $b = 15\,\text{a.u.}$ the qualitative structure of the spectrum is already reproduced.

Choosing a: While it is clear that the upper boundary b should always be chosen as large as possible, such a statement can not be made for the lower boundary a. One might guess that choosing $a = b$ for given b is best, as this would leave the Coulomb potential as undisturbed as possible. However, the resulting discontinuity of the potential at the cutoff $a = b$ then introduces delta-like forces which lead to artifacts in photo-electron spectra. In Fig. 4.4 the beginning of the recollision plateau is shown for various choices of a.

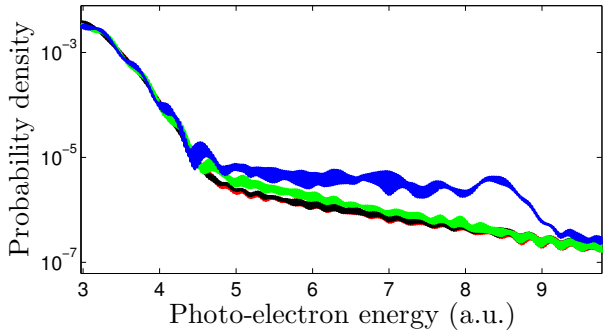

Figure 4.4: Computations with fixed $R_c = R_0 = 120\,\text{a.u.}$ for various truncation intervals, Eq. (2.19): $[a, b] = [80, 120]\,\text{a.u.}$ (red), $[30, 40]\,\text{a.u.}$ (black), $[37.5, 40]\,\text{a.u.}$ (green), $[40, 40]\,\text{a.u.}$ (blue). Same pulse parameters as in Fig. 4.1.

It can be seen that a smooth truncation within $[30, 40]$ a.u. (black) gives excellent agreement with the reference computation (red). As the width of the truncation interval is reduced while keeping the upper boundary fixed at $b = 40$ a.u., significant discrepancies are introduced.

This behavior can not be easily generalized, as the ideal truncation interval width depends on the physical situation and the exact observable of interest. For the here presented laser pulse parameters, discrepancies are largest at the beginning of the recollision plateau, which is not always the case. For example, in elliptically polarized 800 nm fields the dominant emission peak around $2\,U_p$ (see next section) is most accurately described if $a = b$ is chosen, but then severe artifacts are introduced starting from $\sim 3\,U_p$. Thus, the optimal truncation interval width needs to be determined for each physical system and observable independently.

4.1.2 Elliptically polarized fields

The vector potential $\vec{A}$ of a pulse propagating in $\hat{e}_3$-direction with arbitrary polarization can be written as

$$\vec{A}(t) \propto \big(\hat{e}_1 \sin(\omega t) + \hat{e}_2 \epsilon \cos(\omega t)\big)\mathcal{E}(t) \tag{4.3}$$

where $\hat{e}_{1/2}$ are the orthogonal directions to $\hat{e}_3$, $\epsilon \in [0, 1]$ is the ellipticity parameter, and $\mathcal{E}(t) \geq 0$ is the pulse envelope. For $\epsilon = 0$ we recover a linearly polarized pulse, $\epsilon = 1$ implies circular polarization.

At long wavelengths and high intensities, the field of an elliptically polarized pulse combined with the binding potential of the nucleus creates a rotating barrier through which an electron can tunnel (figure 4.6 a, in which the electric field $\vec{E}$ is denoted $\boldsymbol{F}_L$). Owing to the rotation of the barrier, the electron tunnels in different directions at different times, and is subsequently detected at different angles after the end of the pulse (figure 4.6 b). The tunnel probability depends on the instantaneous magnitude of the electric field $|\vec{E}(t)|$ in the adiabatic limit. For circular pulses the maximum is approximately achieved at the same time as the absolute value of $\vec{A}(t) = -\int_{-\infty}^{t} \vec{E}(\tau)$ becomes maximal (except for envelope effects), implying that final photo-electron energies are most probable with a kinetic energy of $2\,U_p$. This is also true for slightly elliptically polarized laser pulses. In non-circular pulses, local maxima in $|\vec{E}(t)|$ lead to bursts of varying strength. Where multiple bursts interfere, complicated structures appear and ATI peaks become discernible, see figure 4.5. Convergence of these spectra required $l_{\max} = 50 = m_{\max}$.

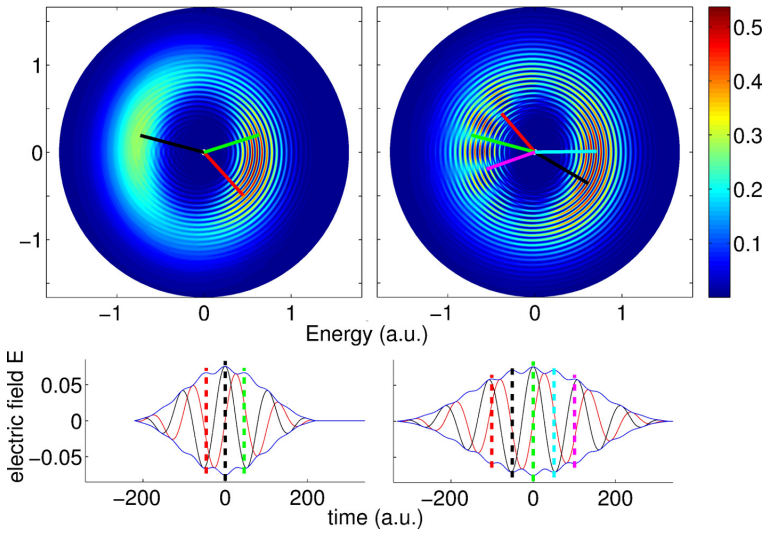

Figure 4.5: Bottom: Electric field components in $\hat{e}_1$ (black) and $\hat{e}_2$ (red) directions for a two-cycle (left) and a three-cycle (right) near circular polarized pulse with wavelength $\lambda = 800\,\mathrm{nm}$ and intensity $I = 2 \cdot 10^{14}\,\mathrm{W/cm^2}$. Dashed lines indicate times of local maxima of the electric field strength $|\vec{E}(t)|$. Exact pulse shape given by Eq. (8.30) and $\epsilon = 0.8$. Top: Corresponding photo-electron spectra in the polarization plane. The plots show the spectra with radial coordinates $k^2/2$ and angles indicating emission direction. Color indicates ionization probability, with a clear maximum along a ring structure with radius $\sim 2\,U_p$. The direction of the bursts is indicated by the colored lines, where the colors of top and bottom plots are chosen correspondingly.

4.1.3 Interpreting Attoclock measurements

In Ref. [2] the possibility to time electron release during photo-ionization employing the Attoclock was analyzed by applying the so-called analytical R-matrix formalism to data of our numerical computations. In this section we summarize the key results.

In the simple case of one-photon ionization, the removal of an electron from an atom or molecule creates a non-equilibrium charge distribution which evolves on the attosecond timescale [96]. Ionization time then serves as a sensitive measure encoding the dynamics of core rearrangement triggered by electron removal (see for example Refs. [97–99]). Understanding the nature of the measured delays required the accurate calibration of the measurement schemes, with the Hydrogen atom used as a benchmark (see for example Refs. [100–103]).

Going beyond the one photon process, employing infrared fields as either pump or probe in time-resolved ionization experiments provides access to the timescale of electronic motion, but it also introduces a hurdle in interpreting such experiments. Identifying and disentangling time delays related to multi-electron dynamics from the apparent delays induced by the interaction with the infrared field is challenging both technically and conceptually as multi-photon ionization can excite rich multi-electron dynamics.

Since strong field ionization at long wavelengths is often interpreted using the tunneling picture (Sec. 1.4.2), time resolving this process opens the opportunity to revisit the long-standing problem of tunneling times [14, 34, 104, 105]. Recent high accuracy measurements of tunneling times in strong-field ionization employed the Attoclock technique [17], which is studied here.

4.1.3.1 The Attoclock

The experimental setup measures angle- and energy-resolved photo-electron spectra produced by ionization in strong, (nearly) circularly polarized infrared fields like Eq. (4.3). Emission times can be inferred from the emission angle. Essentially, the rotating electric field vector serves as the hand of a clock, deflecting electrons in different directions depending on their moment of escape from the atom.

Suppose the field rotates anticlockwise and reaches its maximum at $t = 0$ when the field vector $\vec{E}(t)$ (denoted as $\boldsymbol{F}_L$ in figure 4.6) points at an angle of 90° (as in figure 4.6 b). In the tunneling picture, this instant is associated with the thinnest tunneling barrier and the highest probability of ionization. In the absence of tunneling delays and of electron-core interaction after tunneling, we expect that an electron which escapes at time $t_i = 0$ will be detected at an angle of 0°, orthogonal to $\vec{E}(t)$. Indeed, if the electron is released from the barrier with zero initial velocity, as suggested by the tunneling picture (illustrated in figure 4.6 a), its final momentum at the detector will be $\vec{p} = -\vec{A}(t_i)$, where $\vec{A}(t_i)$ is the vector potential of the laser field at the moment of ionization, see Eq. (4.2). For circularly polarized pulses, $\vec{A}(t)$ is orthogonal to $\vec{E}(t)$ (up to effects of the ultra short envelope).

An observed deviation of the photo-electron distribution maximum from 0° could come from the deflection of the outgoing electron by the attractive core potential ($\boldsymbol{F}_C$ in figure 4.6 b) and, possibly, from tunneling delays [17]. This deviation is characterized by the offset angle θ (figure 4.6 c). Experimentally, θ can be measured with high accuracy ($\delta\theta \sim 2°$), which implies the potential to measure ionization delays with accuracy $\delta\tau = \delta\theta/\omega \sim 15\,\text{as}$ for 800 nm radiation, provided the angles are accurately calibrated, excluding alternative sources for offset angle deviations.

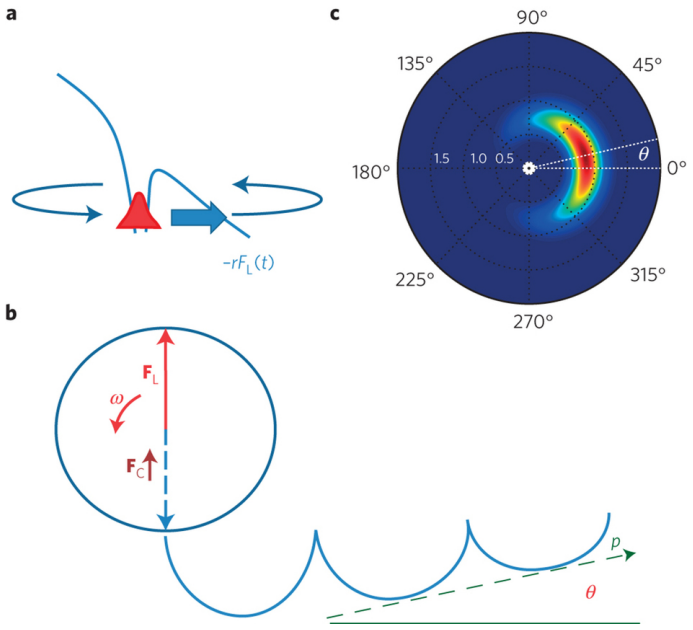

Figure 4.6: a) In the Attoclock setup, the laser field and the core potential together create a rotating barrier through which the bound electron can tunnel. As the barrier rotates, the electron will escape in different directions at different times. b) While the laser field rotates (with frequency ω) it reaches its maximum at some point in time (here: $\boldsymbol{F}_L$ pointing up). The electron tunnels in the opposite direction (blue dashed arrow), and in the absence of electron-core interaction, detection is expected in orthogonal direction (solid green line). An offset $\theta \neq 0$ with resulting final momentum p (dashed green line) could be due to the attractive core potential ($\boldsymbol{F}_C$) and/or possible tunneling delays. c) The experimental observable: The angle- and energy-resolved photo-electron spectrum of Hydrogen due to a single-cycle circularly polarized infrared pulse. Figure taken from Ref. [2].

4.1.3.2 Numerical computations

As reference data for the analysis, results from numerical calculations were employed. These were conducted with three independent codes, see Fig. 4.7, where in all cases the TDSE was solved numerically for pulse shape (8.30) with $n = 1$, $m = 4$ and ellipticity $\epsilon = 1$. An example spectrum is shown in Fig. 4.6 c. The computations marked in black invoked

the tSurff method and represent the main contribution of our group to the publication. Our computations required angular momentum expansions with $l_{\max} = 95$ for the highest intensities. The here considered observable (maximum emission angle) is rather sensitive to the long range behavior of the Coulomb potential. Thus, converged results required box sizes of up to $R_0 = 120\,\text{a.u.}$, discretized with 24 finite elements of order 14 resulting in a total of $\sim$300 radial discretization coefficients.

All three approaches agree, but due to the highly efficient tSurff method convergence was achieved expending less computational resources compared to the other approaches. In particular, the computations marked in green [106] employed the standard approach (see Sec. 2.1.1) and used box sizes of up to 2700 a.u. with nearly 75000 radial coefficients. These numbers seem excessive, as a classical estimate of the maximum wavefunction extension at the end of the very short pulse only gives $\sim$300 a.u.. Indeed, although the method marked in red [107] has no fundamental difference, it only required box sizes of 300 a.u. with 6000 radial coefficients.

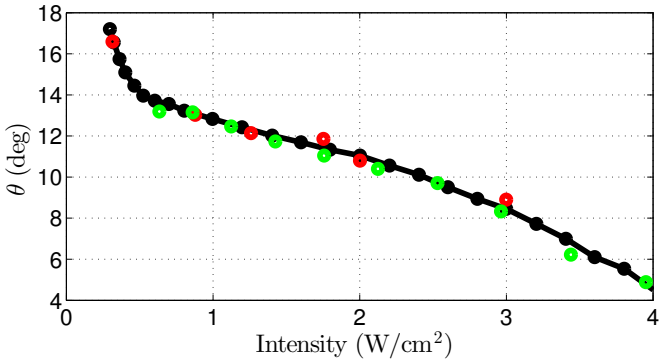

Figure 4.7: Maximum offset angle θ as extracted from TDSE results. Three independent codes were used: Out results, marked in black, employed the tSurff method while results marked in green [106] and red [107] used the standard method, see Sec. 2.1.1.

4.1.3.3 Results

Analysis was performed by invoking the analytical R-matrix (ARM) formalism [108, 109] to results of numerical experiments on Hydrogen and a Yukawa potential. ARM theory allows to establish a connection between the maximum emission angle θ as extracted from TDSE computations, and the moment t_i at which the electron emerges in the classically allowed region:

$$t_i(\theta) = t_0(\theta) - \Delta t_e(\theta) - \Delta t_c(\theta). \tag{4.4}$$

Thereby it fully includes electron-core Coulomb interactions also after tunneling (leading to the correction term Δt_c), and also short envelope effects are taken into account (leading to the correction Δt_e). t_0 is the simple expectation according to Eq. (4.2) with $t_0(\theta = 0) = 0$. The contributions of the three terms in Eq. (4.4) are summarized in Fig. 4.8.

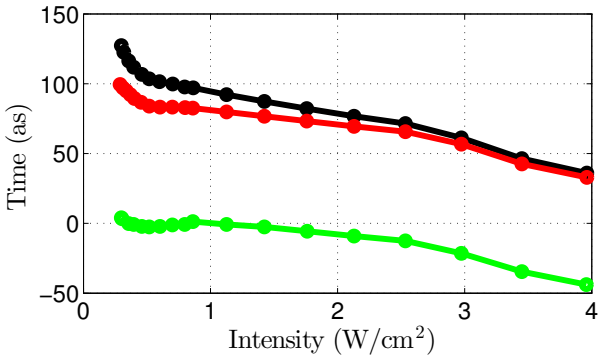

Figure 4.8: Black: Ionization time t_0 neglecting short pulse effects and long range Coulomb interactions. Red: Short pulse corrected $t_0 - \Delta t_e$. Green: t_i also including Coulomb corrections. It can be seen that the ionization time extracted with ARM theory from TDSE results is close to zero for intensities below $\approx 1.5 \times 10^{14}\,\mathrm{W/cm^2}$ and then becomes increasingly negative.

It can be seen that for intensities below $\approx 1.5 \times 10^{14}\,\mathrm{W/cm^2}$ the Attoclock setup detects no tunneling delays for Hydrogen. At higher intensities the negative time delays indicate that the dominant contribution to the ionization process stems from times slightly before the peak electric field is reached, which could in parts be attributed to ground state depletion. Investigations with independent analytical theories indicated that frustrated tunneling [110] (no true ionization but recapture at recollision into Rydberg states) may be responsible for the remaining negative delay [2].

However, the situation may be different when electronic excitations during ionization are involved. For two-electron systems, independent computations indicated that multi-electron responses to the infrared laser field leave distinct traces in Attoclock measurements, leading to additional delays, either negative or positive. Thus, employing the here presented calibration of the Attoclock, such experiments with molecules or alkaline-earth atoms, where doubly excited states lie below the first ionization threshold, may uncover a rich multi-electron response. These are expected to manifest in non-trivial, intensity dependent ionization delays caused by correlation-driven excitations during strong-field ionization.

4.2 Effective potential: Pseudo Helium

The Helium system represents a 6-dimensional problem (5-dimensional for linearly polarized laser pulses due to symmetry). A full numerical treatment is extremely cumbersome, but only necessary if simplifying models are not sufficiently accurate for the observable of interest.

4.2.1 Applicability

Treating Helium as a single-electron system in an effective potential created by the second electron is justified if all forms of dynamical electron-electron correlation effects can be neglected. These include core polarization effects, dynamic exchange (both treated in Sec. 5.1), the existence of doubly excited states (treated in Sec. 5.2), and double ionization dynamics (treated in chapter 6).

In the perturbative regime only the missing doubly excited states have a significant effect on the single ionization dynamics. In the long wavelength regime core polarization effects would become noticeable if the ionic excitation energy were not so exceptionally large. The first excited state of the He^+ ion is 1.5 a.u. above its groundstate, which is too large a gap for all but the highest laser intensities. In other atoms, where ionic excitation energies are significantly smaller, polarization effects become relevant. There, qualitatively accurate results can be achieved already by including a small number of ionic bound states, see Sec. 5.1. However, in most Alkali metals, where the ion has a closed shell, and noble gases, where ionic excitation involves an electron changing subshell [111], a simple single-electron effective potential is often sufficient.

The "Pseudo Helium" potential

$$V(r) = -\frac{1 + \mathrm{e}^{-\alpha r}}{r} \tag{4.5}$$

with $\alpha = 2.1325$ strongly resembles the effective potential a single electron is subjected to in the Helium atom. In particular, its first 5 bound states are similar to Helium's ionization potentials, which is shown in the table below.

Dominant configurations:	$1s^2$	$1s2s$	$1s2p$	$1s3s$	$1s3p$
Helium ionization potentials [112]:	0.90372	0.146	0.124	0.061	0.0551
Pseudo Helium bound state energies:	0.90370	0.157	0.128	0.064	0.0556

4.2.2 Interpreting longitudinal momentum spreads

Due to the strong similarities in ionization potentials, we may use the effective potential (4.5) to describe single ionization of Helium at long wavelengths, and apply it to provide the numerical results on which the work in Ref. [1] is based. Here we summarize the key results.

Electrons which are freed from their atom by a strong, elliptically polarized laser field through tunnel ionization acquire a momentum in the direction of the electric field (also referred to as the longitudinal direction) at the instance of ionization during propagation in that same field. The value of the acquired momentum depends on the phase of the field at the moment when the electron exits the tunnel and enters the continuum. This results in a final longitudinal momentum spread $\sigma_{\parallel}$ which can be measured at a detector, see left plot in Fig. 4.9. In semi-classical models where tunnel ionization is followed by classical propagation starting from the tunnel exit one often includes initial momentum spreads. While the expressions for the initial transverse spread at the tunnel exit are well accepted [113], the initial longitudinal spread has long remained a matter of debate, with the usual assumption that it is equal to zero [55]. Recent experimental results [38] could however not be explained under that assumption, but quantitative agreement was found if a non-zero initial longitudinal spread is used [114]. In Ref. [1] it is investigated whether non-adiabatic effects, instead of an initial longitudinal momentum spread, can account for discrepancies between theory [36, 37] and experiment [38].

To ensure that the additional longitudinal momentum spread $\sigma_{\parallel}$ measured in the experiment (Fig. 4.10) reflected underlying physics and was not the result of unknown experimental noise, solutions of the TDSE were used for comparison, see figure 4.9.

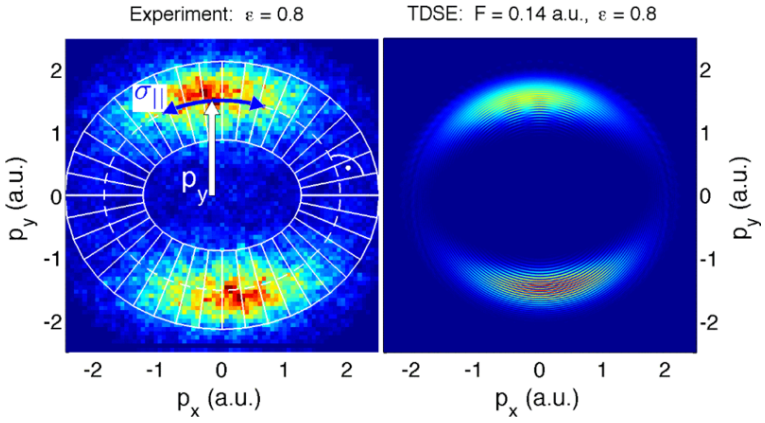

Figure 4.9: The final electron-momentum distributions $P(\vec{k})$ in the plane of polarization as measured in COLTRIMS (cold target recoil ion momentum spectrometer [115]) and calculated by TDSE shows two distinct maxima separated by $2p_y$ along the minor axis. In TDSE, wave packets from different cycles of the pulse interfere (pulse shape: Eq. (8.30) with $n = 2$ and $\epsilon = 0.8$) leading to interference patterns which the experiment could not resolve. Figure taken from Ref. [1].

Conducting the numerical computations was the main contribution of our group to the publication. The observable longitudinal momentum spread $\sigma_\parallel$ is similarly sensitive to the long range behavior of the Coulomb attraction as the angle of peak emission considered in the previous Sec. 4.1.3. Thus, we had to employ box sizes of up to $R_0 = 120\,\text{a.u.}$ discretized with ~ 300 radial coefficients, and angular momentum grids with $l_{\max} = 95$ to ensure errors below 1%. The momentum spreads found in TDSE results agree with experimental measurements at high ellipticity and exceed the measured values at lower ellipticity (see figure 4.10). The minor deviations could either be a two-electron effect, neglected in the used effective single-electron potential (4.5), or an artifact of the actual experimental conditions [38].

These results are compared with various approaches for adiabatic and non-adiabatic theories, all based on PPT theory [116] which converges to ADK (see Sec. 1.4.2) in the adiabatic limit. The PPT expression for the ionization probability depending on the final momentum $\vec{p}$ at Keldysh parameter γ is given by equation (3) in Ref. [1]. In Fig. 4.10 we show the predictions from the purely analytical expressions of the non-adiabatic theory [117] (solid red) and the adiabatic theory [113] (blue dashed). Thereby the same underlying assumptions are employed for both the tunneling process and the extraction of laser field strength from experiment. (The field strength obtained assuming adiabaticity is $F^{\text{A}} = 0.151\,\text{a.u.}$, assuming non-adiabaticity it is $F^{\text{NA}} = 0.14\,\text{a.u.}$.) An inconsistent combination of non-adiabatic theory with adiabatic field strength extraction is also shown (dotted red). Also classical trajectory Monte Carlo (CTMC) simulations were employed for the electron trajectories after tunnel ionization in order to calculate the final longitudinal momentum spread $\sigma_\parallel$ for both theories (red and blue stars) assuming zero initial longitudinal momentum spread. Adding a possible initial momentum spread, perfect agreement with the experimental data is found (as described in Ref. [114]), where the values for the best fit are shown as blue and red triangles.

It turns out that the non-adiabatic and the adiabatic theories give nearly coinciding results for the final momentum spread $\sigma_\parallel$ (both for the full analytic expression and the CTMC simulations), and that both cannot explain fully the experiment, if applied consistently. However, if non-adiabatic theory is inconsistently combined with a standard (adiabatic) intensity calibration technique from Ref. [118], then it fits the experiment better (red dotted line).

This highlights a problem of current intensity calibrations: Experimental intensity calibration of laser sources is often based on some version of strong field ionization theory. Even worse, typically, experimental data is first calibrated with a specific theory, and later the calibrated data is used to test the exact same theory. For example, in the context of final momentum spreads in strong field ionization experiments, the results in Ref. [14] were consistent with a non-adiabatic approximation, the same theory which was also used to calibrate their experimental data. Similarly, in Ref. [119], consistency in the transverse momentum spreads with the adiabatic ADK theory [36, 37] was shown, but an adiabatic assumption of zero initial velocity was used to calibrate the experimental data.

Theory-independent intensity measurements would therefore be desirable. However, these are known to be highly imprecise [120], hence necessitating the use of theory-based

calibration.

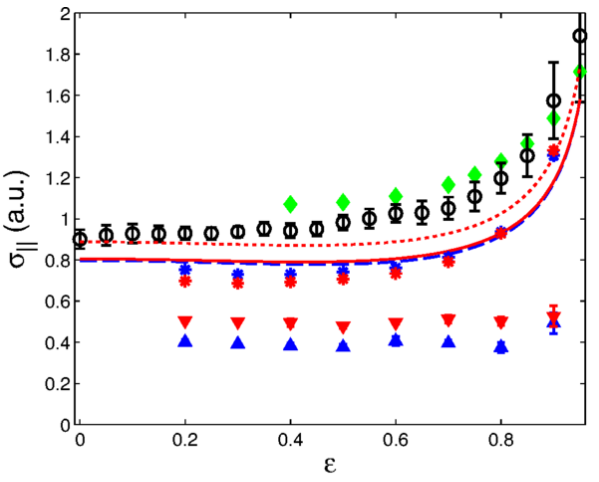

	type	theory	field strength
○	experiment		
– –	analytical	ADK, A	$F^{\mathrm{A}} = 0.151$ a.u.
···	analytical	PPT, NA	F^{A}
—	analytical	PPT, NA	$F^{\mathrm{NA}} = 0.14$ a.u.
*	CTMC	ADK, A	F^{A}
▲	$\sigma_{\parallel}^{\mathrm{in}}$	ADK, A	F^{A}
*	CTMC	PPT, NA	F^{NA}
▼	$\sigma_{\parallel}^{\mathrm{in}}$	PPT, NA	F^{NA}
♦	TDSE		F^{NA}

Figure 4.10: Longitudinal momentum spread $\sigma_{\parallel}$ as a function of ellipticity ϵ. A = adiabatic, NA = non-adiabatic. All error bars show the 98% confidence interval of the corresponding fitting process to extract the respective value. See text for detailed explanation of all data series. Figure taken from Ref. [1].

It can be concluded that adiabaticity effects can not explain discrepancies between theory and experiment. Further theoretical work is needed to find a physical model motivating the origin of the initial longitudinal momentum spread required to match the experimental results. Moreover, further investigation is required to establish better than the current state of the art calibration methods for the $\gamma \approx 1$ regime, where a majority of experiments in attosecond science take place.

In Ref. [121] an alternative to the usual calibration method is proposed. Based on our numerical results, it was found that the transverse momentum spread appears relatively insensitive to non-adiabatic effects, and is therefore better suited for calibration then the typically used maximum of the transverse momentum distribution.

4.2.3 Experimental Attoclock results for Helium

Recently, experimental data obtained in an Attoclock setup was used to infer tunnel delay times in strong field ionization of Helium in a few cycle elliptically polarized pulse [35]. The measured deflection angles θ (defined as in Fig. 4.6) do however not match straight forward TDSE computations employing the single active electron approximation. In an attempt to understand the precise experimental conditions, we performed extensive numerical studies, varying several experimentally undefined parameters, but we were not able to match our results with the experimental data. Figure 4.11 compares the published data with results of our TDSE simulations, where we tried to mimic the experimental conditions as close as possible.

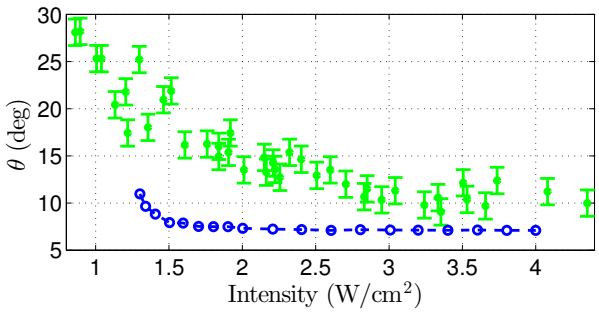

Figure 4.11: Green: Experimental values for the deflection angle θ as a function of the cycle-averaged intensity, extracted from Ref. [35]. Blue: TDSE results employing a shifted envelope and an average over the carrier-envelope-phase, see text below for details. Computations at lower laser intensities suffer numerical problems due to small overall signals and could not be converged. It can be seen that the experimentally measured emission angle exceeds our numerical results by $\sim 3°$ at high intensities and up to $\sim 10°$ at low intensities.

We investigated several possible sources for the discrepancies:

4.2.3.1 Pulse shape effects

The exact experimental pulse is unknown. The conditions determined in the experiment are a wavelength of 735 nm, an ellipticity of $\epsilon = 0.87$ and a pulse duration of 6.1 fs. Detailed information like the exact envelope and the carrier-envelope-phase (CEP) remain undefined. Let the pulse be given by the expression

$$\vec{A}(t) \propto C_1(t)\sin(\omega t + \varphi_{\text{CEP}})\vec{e}_1 + C_2(t)\cos(\omega t + \varphi_{\text{CEP}})\vec{e}_2 \tag{4.6}$$

where $C_{1/2}(t)$ are the envelope functions of the $\vec{e}_{1/2}$ components, and φ_{CEP} is the CEP.

The first thing to note is that in case of low intensity near circular polarized pulses, the smoothness of the pulse envelope functions $C_{1/2}(t)$ is crucial. Figure 4.12 compares two

total photo-electron spectra computed for equal conditions except for the envelope. It can be seen that a $\cos^2$-envelope produces spurious artifacts near $E = 0$ and also discrepancies for high energies arise. These artifacts become larger for decreasing intensities.

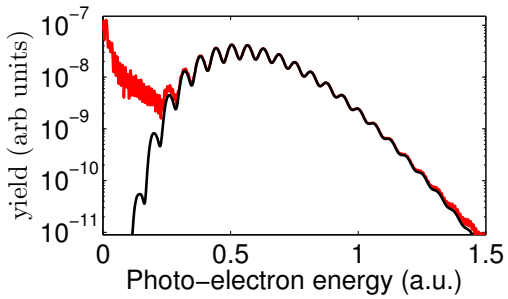

Figure 4.12: Angle integrated photo-electron spectrum for low intensity elliptically polarized pulses (8.30) with equal parameters ($I = 2 \cdot 10^{14}\,\mathrm{W/cm^2}$) except for the pulse envelope: A $\cos^2$-envelope (red) produces significant artificial enhancement at low energies compared to the more realistic $\cos^8$-envelope (black).

Second, there is the question on how $C_1(t)$ and $C_2(t)$ relate. The pulse defined in Eq. (8.30) assumes $C_1(t) = C_2(t)$, but the experiment uses a quarter wave plate to create the elliptically polarized pulse. Thereby it might be appropriate to assume that the entire envelope is shifted by a quarter of a cycle: $C_1(t) = C_2(t + \frac{\pi}{2\omega})$. Computations comparing pulses with $C_1(t) = C_2(t + \frac{\pi}{2\omega})$ and with $C_1(t) = C_2(t)$ reveal differences in the maximum emission angle θ on the order of $\delta\theta \sim 1°$, where the sign of the discrepancy depends on the CEP.

Further the CEP is unknown, and TDSE results show that $\delta\theta \sim 5°$ with varying CEP. The experimental value of the CEP is however expected to change from laser shot to laser shot, implying that the measured spectrum is some kind of average over all CEP. Assuming that all CEP appear with equal probability we can include this averaging effect in our computations. The result of this averaging in turn depends on the assumptions on the pulse envelope. If $C_1(t) = C_2(t)$, then contributions from φ_{CEP} and $-\varphi_{\mathrm{CEP}}$ cancel out and the final averaged results for θ equals the results from a single computation with $\varphi_{\mathrm{CEP}} = 0$. If however $C_1(t) = C_2(t + \frac{\pi}{2\omega})$, then no such cancellation happens, and the CEP averaged result for θ is $\sim 2°$ larger than the result of a single computation with $\varphi_{\mathrm{CEP}} = 0$.

4.2.3.2 Calibration of maximum emission angle

A direct consequence of the unknown pulse shape in experiment is unknown direction of peak electric field, which defines the expected emission direction according to the simple tunneling picture (the t_0 term in Eq. (4.4)). This amounts to an inability to calibrate the emission angle, as the point $\theta = 0$ is unknown. In the experiment, they only had access to time averaged quantities and the reference angle was determined by maximizing the

expression

$$I(\alpha) = \int \mathrm{d}t \, (\vec{E}(t) \cdot \hat{e}_\alpha)^2. \tag{4.7}$$

which deviates from the peak electric field direction by up to $\sim 6°$, depending on the CEP. After averaging over the CEP this gives a $< 1°$ positive correction to the emission angle θ, which is included in the data points of Fig. 4.11.

4.2.3.3 Conclusion

The experimentally measured angle of maximum emission θ as a function of intensity could not be reproduced within numerical TDSE computations, although small corrections to the TDSE results due to CEP averaging and the calibration of the maximum emission angle reduced the discrepancies. We can speculate on possible reasons:
First, we may have overlooked a pulse shape effect. For example the average over the CEP in experiment may not be uniform. Second, the single-electron model excludes multi-electron effects. Their influence is currently being investigated employing a coupled channels approach (described in Sec. 5.1), and first results indicate that corrections of few degrees may be possible. Third, there might be an experimental error in the measurements.

Should further numerical studies achieve agreement with the experimental data, then improvements for the experimental setups could be suggested. For example, if CEP effects turn out to be relevant, as indicated by the strong dependence in a single active electron approximation, then a CEP stabilized experiment is required for correct extraction of ionization times.

Chapter 5

Single-ionization of multi-electron systems

While simple single-electron models (like in the previous section) or also low dimensional models have been partially successful in explaining laser matter interactions, there have been several cases reported where a more elaborate description of electronic structure becomes important. Some of the examples include inter-channel coupling leading to an enhancement in high harmonic generation (HHG) from Xenon [122], modification of angle resolved ionization yield of CO_2 [123], photo-ionization cross sections in SF_6 [124], enhancement in HHG due to participation of doubly excited states in Beryllium [125], influence of nuclear motion [126], and presence of conical intersections [127]. All these instances need a more involved description of the electronic structure.

For one- and two-electron systems a full dimensional numerical treatment is possible. However, for systems with more than 6 degrees of freedom a full dimensional calculation is unfeasible. There have been several efforts in the past decade to overcome this barrier of dimensionality for few electron systems by choosing only a part of the Hilbert space that is seemingly important for the dynamics. Some of the approaches that are being employed are time-dependent configuration interaction methods [128], different variants of multi-configuration methods [129], the time-dependent R-matrix method [130], and coupled channel methods [123].

In this section we present the hybrid anti-symmetrized coupled channels (haCC) method, where all but one electron may populate only field free ionic bound states, while only this one electron can evolve without restriction. Results for (effective) two-electron systems obtained with haCC are compared with results employing a full (unrestricted) basis and with results using a single-electron effective potential. Physically, this allows to establish a hierarchy of complexity: On the one hand side there are multi-electron systems and observables which are perfectly fine described by a single-electron model. Then there are systems and observables which require a more elaborate treatment of multi-electron effects, but still allow for the restrictions incorporated in haCC, and then there are those which call for a fully non-restrictive ansatz. An example for a phenomenon which can be accurately described employing haCC are resonant line shapes

of doubly excited state, which are treated in detail in Sec. 5.2.

For the computation of photo-electron spectra we employ the multi particle version of tSurff for single emission, see Sec. 2.2.4.

5.1 Polarizable effective potentials

This section summarizes the publication [4].

The ansatz is based on the following physical picture: For many laser parameters only one electron fully follows the laser pulse, while the remaining electrons only weakly participate in the dynamics and mainly "remain bound". Thus, we allow only the one electron to be excited into the continuum, ionize and possibly rescatter. The other electrons are only allowed to couple to a limited number of field free ionic bound states.

5.1.1 The haCC approach

We discretize our multi-electron wavefunction by a severely restricted basis [4]:

$$|\Psi(t)\rangle \approx \sum_{\mathcal{I}} |\mathcal{I}\rangle C_{\mathcal{I}}(t) + |\mathcal{G}\rangle C_{\mathcal{G}}(t) \tag{5.1}$$

where the

$$|\mathcal{I}\rangle = \mathcal{A}[|i\rangle \otimes |I\rangle] \tag{5.2}$$

consist of an anti-symmetrized product (indicated by $\mathcal{A}$) of an unrestricted single-electron basis (same as in Sec. 3.1.1)

$$|i(\vec{r})\rangle = |R_{lm}(r)\rangle \otimes |Y_l^m(\Omega)\rangle \tag{5.3}$$

and ionic wavefunctions $|I\rangle$, which in case of Helium simply represent hydrogenic bound states scaled to twice the nuclear charge. In practice these were obtained from the multi-reference configuration interaction singles doubles (MR-CISD) [131] level of quantum chemistry, computed by the COLUMBUS code [132]. $|\mathcal{G}\rangle$ is chosen as the ground state of the system, also obtained from the MR-CISD level of quantum chemistry. These quantum chemistry wavefunctions are constructed with an atom centered primitive Gaussian basis as the starting point.

This procedure works for an arbitrary number of restricted electrons. The wavefunctions $|\mathcal{G}\rangle$ and $|I\rangle$ can be represented in a general form as sums of determinants:

$$|I\rangle = \sum_{p_1 \dots p_{n-1}} d_{p_1 \dots p_{n-1}} |\mathcal{A}[\phi_{p_1} \cdots \phi_{p_{n-1}}]\rangle \tag{5.4}$$

$$|\mathcal{G}\rangle = \sum_{p_1 \dots p_n} d_{p_1 \dots p_2} |\mathcal{A}[\phi_{p_1} \cdots \phi_{p_n}]\rangle. \tag{5.5}$$

where ϕ_{p_i} are single-electron Hartree-Fock orbitals of the neutral system.

This is a hybrid ansatz using an unrestricted numerical basis $\{|i\rangle\}$ together with an ionic basis $\{|I\rangle\}$ and treating anti-symmetrization exactly. Consequently, the method was dubbed hybrid anti-symmetrized coupled channels (haCC) method. The resulting set of coupled ordinary differential equations is solved with out tRecX code, see Sec. 3.4. The ionic basis creates a sophisticated time-dependent effective potential for the one fully active electron, and in that sense the method implements a polarizable effective potential. Explicitly, compared to the true single particle effective potential presented in Sec. 4.2, the haCC ansatz includes polarization effects, but only partially, as virtual excitations of the ion are only possible within the restricted basis (in particular we do not include continuum contributions to polarization). The method also allows for core excitations and thereby opens the possibility for ionization into excited channels. Also, it fully includes exchange interaction due to indistinguishability of electrons, which is correctly accounted for by the anti-symmetrization. Dynamic exchange interaction is often neglected in similar approaches, but in Ref. [26] it was shown that this effect is crucial for reproducing the experimentally observed angle of peak ionization yield in CO_2.

There is no quantitative statement possible concerning where this picture breaks down. In general one may say, that at small Keldysh parameters $\gamma < 1$ the picture is accurate, and a rather small restricted basis is often able to represent the relevant polarization effects. At large $\gamma > 1$ however many effects may require a huge ionic basis as shake-up channels or near-threshold ionic excitations become important.

5.1.2 Helium

We first apply this method to the Helium atom, where we expect the haCC approach to be well suited due to the high excitation energy of the ion of 1.5 a.u..

5.1.2.1 Short wavelength regime

We start in the perturbative regime with a wavelength of $\lambda = 21\,\mathrm{nm}$ ($\hbar\omega \approx 2.2\,\mathrm{a.u.}$), where core polarization is negligible. As detailed in Sec. 1.4.1, we expect peaks in the photoelectron spectrum at energies $-I_p^{(1)} + n\hbar\omega$ where $n \in \mathbb{N}$ is the number of absorbed photons and $I_p^{(1)} \approx 0.9\,\mathrm{a.u.}$ is the first ionization potential of the Helium atom. The possibilities of doubly excited states and ionization into excited ionic channels are introduced compared to the single particle effective potential used in Sec. 4.2. One example for a double excited state is the $2s2p$ state, where both electrons are elevated into the second shell. This will be discussed in more detail in section 5.2. In figure 5.1 we compare results obtained employing the haCC ansatz with results using the full two-electron basis described in Sec. 3.1.2 and the single particle effective potential of Sec. 4.2.

The required quality of the unrestricted part of the haCC basis $\{|i\rangle\}$ is equal to those of the two-electron basis (3.14) and the single-electron basis (3.3). The size of the ionic basis $\{|I\rangle\}$ is parametrized by the principal quantum number n, indicating up to which atomic shell all field free ionic bound states are included. For example, $n \leq 2$ indicates the inclusion of the following ionic states: $1s$, $2s$, $2p_x$, $2p_y$ and $2p_z$.

Concerning the ground state ionic channel (left graph of Fig. 5.1), it can be seen that decent agreement is achieved between all three approaches, except for the doubly excited $2s2p$ resonant line shape shown in the inset. Neither the single-electron effective potential nor the haCC basis with only one ionic basis function can represent a doubly excited state. However, as soon as the second shell $n = 2$ is included, excellent agreement is achieved between the full two-electron basis and the very restrictive haCC basis. Note, that the line shape is not converged with respect to the end of time propagation T, Eq. (2.11), a detailed study follows in section 5.2.

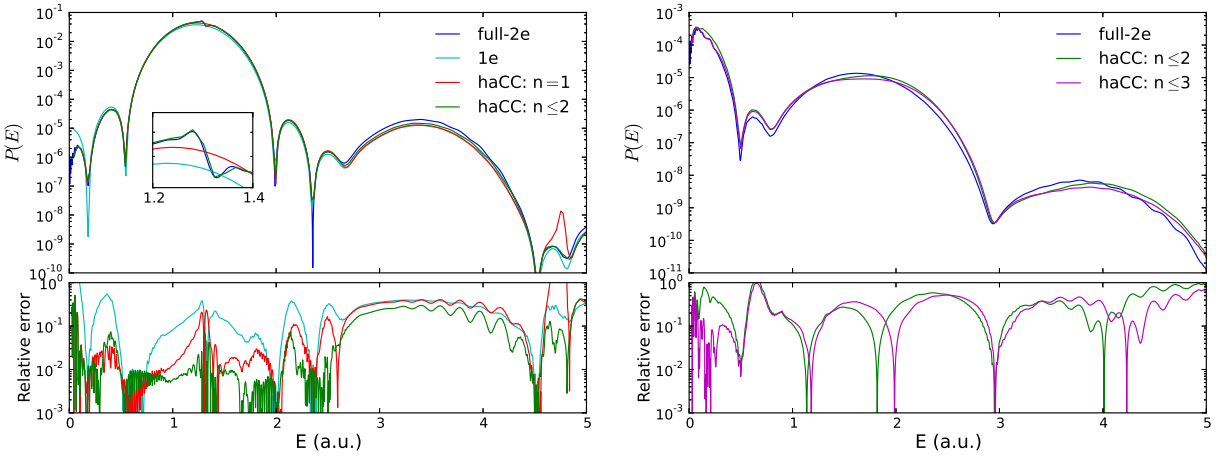

Figure 5.1: Photo-electron spectra ($P(E)$ in Eq. (3.8)) of Helium in a three-cycle, linearly polarized 21 nm laser pulse with a peak intensity of $10^{15}\,\mathrm{W/cm^2}$, Eq. (8.26). Left figure: Ground state channel ($1s$). Right figure: A first excited state channel ($2p_z$). The upper panels show spectra obtained with a full two-electron basis (full-2e), the single-electron effective potential (1e, only for the ground state channel), and haCC calculations with different number of ionic states included as indicated in the legend by the principal quantum number n. The lower panels show relative errors with respect to the full two-electron calculations. The inset shows the $2s2p$ resonance. Figures taken from Ref. [4].

Although the single-electron model in effective potential (1e) and the haCC basis with a single ionic state $n = 1$ are very similar, they give small quantitative differences in the results albeit identical ionization potentials. These can originate in any of the differences between the models. As already mentioned, haCC includes dynamic exchange interaction. Further, the effective potential created by the ionic ground state need not be exactly the same as Eq. (4.5). Finally, the explicit inclusion of the ground state $|\mathcal{G}\rangle$ introduces strong initial state correlations.

The excited state ionic channel (right graph) is non-existent in the single particle effective potential computation and can only be represented in the haCC approach if at least two ionic basis functions are included. If the second shell $n = 2$ is fully included, agreement is already on the level of a few percent. Convergence with the other

discretization parameters is achieved with $l_{\max} = 5$, $m_{\max} = 1$ and 9 finite elements of order 12 in a box size of $R_0 = 45\,\text{a.u.}$, where the large box size is only needed to accommodate the high lying ionic states with large spatial extent.

5.1.2.2 Near visible wavelength regime

We continue with larger wavelengths. Due to the small basis size of haCC we can increase the wavelength of the external laser pulse without running into the disastrous scaling problems described in Sec. 2.2.1, such that the computational effort at $\lambda = 400\,\text{nm}$ is moderate. In contrast, the full two-electron computation represents a significant computational effort. In Fig. 5.2 it is shown that at this near visible wavelength the haCC approach gives excellent results. Except for double ionization all relevant physical phenomena are captured by the haCC basis. As in the short wavelength case, the single-electron computation gives qualitative agreement, but quantitative deviations are present. Convergence with angular momenta required $l_{\max} = 16$.

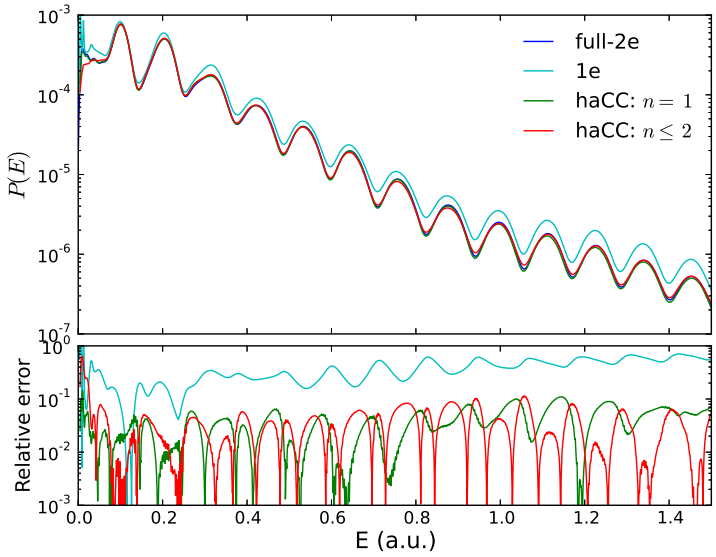

Figure 5.2: Total photo-electron spectra from Helium exposed to a three-cycle, linearly polarized 400 nm laser pulse with peak intensity $3 \cdot 10^{14}\,\text{W/cm}^2$, Eq. (8.26). The upper panel shows spectra obtained from haCC calculations with different numbers of ionic states included as indicated in the legend, and compares them to a full two-electron computation (full-2e) and a computation of a single electron in an effective potential (1e). The lower panel shows relative errors with respect to the full-2e calculation. Figure taken from Ref. [4].

Thus, for qualitative analysis of single emission of Helium in external laser fields, single-electron computations in an effective potential like in Eq. (4.5) are adequate. These can

be obtained with marginal computational effort. Quantitative agreement down to $< 10\%$ accuracy compared to a full two-electron computation over most part of the spectrum can be achieved using an haCC ansatz with just a single ionic basis function (and the fully correlated groundstate). To illustrate the hierarchy in computational effort we summarize computation times and the total number of coefficients (length of vector $\vec{c}$ in Eq. (3.2)) in the table below. All computations were thereby conducted using 8 computing cores in parallel.

Method	Computation time	Coefficient vector length
full-2e	150000s $\approx$ 42h	510000
1e	70s	1600
haCC: $n = 1$	55000s $\approx$ 15h	46000
haCC: $n \leq 2$	170000s $\approx$ 47h	105000

The reason for the comparably long computation times of the haCC approach albeit their significantly smaller basis size, is a reduced sparsity of the corresponding Hamiltonian and overlap matrices, and a resulting less efficient parallelization scheme.

5.1.3 Beryllium

The true might of the haCC approach is its ability to also deal with many-electron systems, like large atoms or even molecules. For example in Ref. [26] the CO_2 molecule was examined, which is currently only possible employing haCC.

Here we consider the Beryllium atom, which is a four electron system that is often treated as a two electron system due to the strong binding of its inner two electrons. The first excitation energy of Be^{2+} is ≈ 4.5 a.u.. With photon energies below this third ionization potential, it can be safely treated as an effective two-electron system. This allows us to use the full two-electron basis by adapting the simple Coulomb potential to an effective potential. We use the effective potential given in Ref. [133]:

$$V(r) = -\frac{2}{r}\Big(1 + (1+\beta r)\mathrm{e}^{-2\beta r}\Big) - \frac{\alpha_c}{2r^4}\Big(1 - \mathrm{e}^{(r/r_c)^3}\Big)^2 \tag{5.6}$$

where the parameters $\alpha_c = 0.05$, $\beta = 2.3$ and $r_c = 0.4$ are chosen appropriately. The groundstate of this potential is artificial and needs to be projected out explicitly. The ionization potentials of the first few excited states correspond to the bound states of the outer two electrons in Beryllium's electronic shell.

Figure 5.3 shows photo-electron spectra for Beryllium created by 21 and 200 nm wavelength laser pulses. It can be seen that as soon as the second shell $n = 2$ is fully included, i.e. all the states $1s^2 2s$ and $1s^2 2p_i$ $(i = x, y, z)$, then results employing a full two-electron basis in an effective potential and the haCC approach coincide up to 20% accuracy.

The fact that at 200 nm wavelength (right plot) the single ion computation (only including $1s^2 2s$) significantly differs from the true result, implies that single-electron

models break down. A single electron in an effective potentials worked fine in Helium (Sec. 5.1.2) and also works fine for Lithium, the smallest alkali metal, see for example in Ref. [134], but Beryllium can not be successfully modeled with a single-electron effective potential. With $1s^2 2s$ and $1s^2 2p$ ionic states included, the spectra produced have 20% accuracy with respect to the two-electron calculation. With the addition of $1s^2 3s$ and $1s^2 3p$ states, the resonant structure corresponding to the $1s^2 2p 3s$ doubly excited state at ≈ 0.39 a.u. [125] starts to emerge. The coupled channels calculations with the number of ionic states considered here, however do not reproduce the structure exactly. This is because the correct representation of a strongly correlated state that has bound character requires a large number of ionic states. The full two-electron basis is able to describe such states but implies a significant computational task. As an alternative strategy, the correlated state of interest could be explicitly included into the basis, on the same footing as the correlated ground state. This is however only possible if it can be identified in advance, which is a non-trivial task (as opposed to the ground state) because it is embedded in singly ionized continuum.

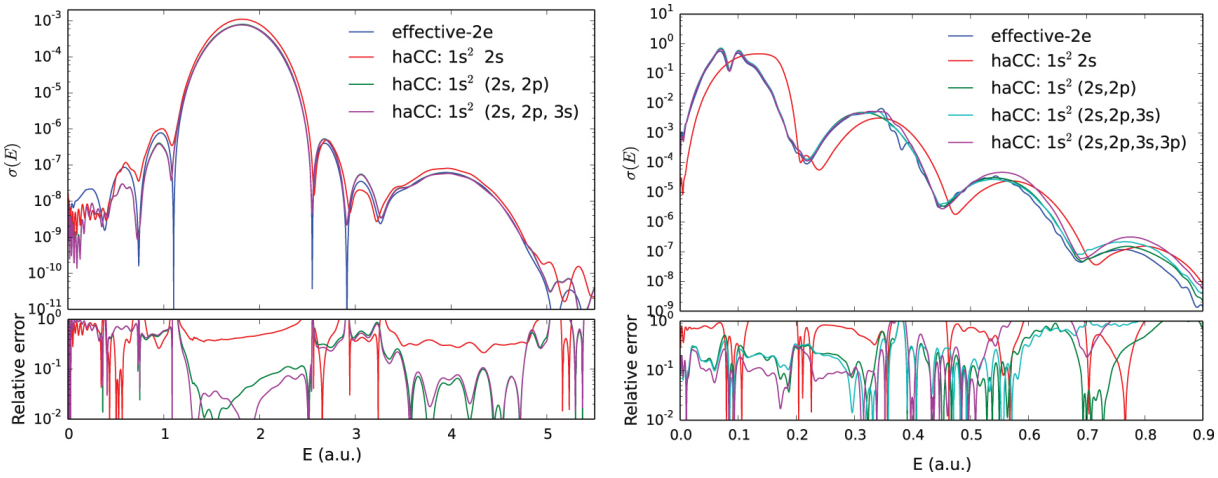

Figure 5.3: Total photo-electron spectra from the Beryllium atom. Left figure: Ground state channel spectra from three-cycle, 21 nm laser pulse with peak intensity 10^{15} W/cm^2. Right figure: Total spectra from three-cycle, 200 nm laser pulse with peak intensity of 10^{14} W/cm^2. Exact pulse shape given by Eq. (8.26) with $m = 8$. The upper panels show spectra obtained with the full two-electron basis in an effective potential (effective-2e) and haCC calculations with different number of ionic states included as indicated in the legend. The lower panels show relative errors of haCC calculations with respect to the effective-2e calculations. Figure taken from Ref. [4].

5.1.4 Hydrogen molecule

Finally we show results for one of the simplest molecules. The Hydrogen molecule H_2 in linearly polarized laser fields parallel to the molecular axis, with fixed nuclei has the same

symmetry as Helium in linearly polarized laser fields. The off-centered nuclear potential does however increases the angular momenta requirement when treated with a single center expansion, Eq. (3.3). While the number of basis functions can be reduced through a choice of a more natural coordinate system like prolate spheroidal coordinates for diatomics [135], these necessitate complicated transformation for the extraction of photo-electron spectra using tSurff. In the case of the Hydrogen molecule at equilibrium internuclear distance (1.4 a.u.), a calculation with a single center expansion easily converges, as the proton charges do not significantly distort the spherical symmetry of the electron cloud. We used $l_{\max} = 15$.

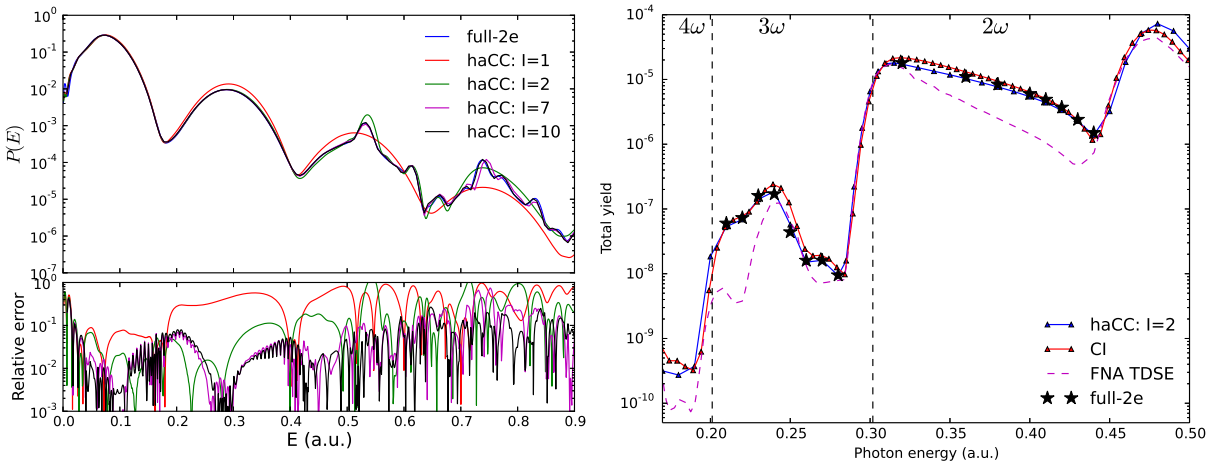

Figure 5.4: Left figure: H_2 photo-electron spectra from a three-cycle 200 nm laser pulse with a peak intensity of 10^{14} W/cm^2, Eq. (8.26). The upper panel shows spectra obtained with full-2e and haCC calculations with different number of ionic states included (as indicated in the legend). The lower panel shows relative errors of haCC calculations with respect to the full-2e calculation. Right figure: Ionization yield from H_2 as a function of photon energy. haCC results with I = 2 ionic states are compared with CI results from Ref. [136], TDSE results from Ref. [126], and our full-2e results. The dashed vertical lines separate different multi-photon ionization regimes. Figures taken from Ref. [4].

Figure 5.4 (left) shows spectra at 200 nm which are converged up to 10% with 2 ionic states. Addition of more ionic states helps reproduce additional resonant features in the spectrum. Figure 5.4 (right) compares the ionization yields for different wavelengths in the range $\hbar\omega = 0.17 - 0.5$ a.u. with other published results. We believe that the present level of agreement between haCC and the results from Ref. [136] using a time-dependent configuration interaction method (CI) is quite satisfactory and supports the validity of both approaches.

5.2 Fano resonances

We now focus on the subject of doubly excited states, which lead to characteristic line shapes in the photo-electron spectrum, called Fano line shapes [39]. They appear not just in the Helium atom, for which we go into further detail here, or in Beryllium (Sec. 5.1.3), but in virtually all atoms and molecules with more than one electron [43]. The mechanism leading to Fano line shapes is general as it is independent of the particular nature of the transitions and states involved, implying that the description applies to other physical situations as well.

This section is based on our publication [5].

5.2.1 Fano situation

The Fano system is encaptured by the following Hamiltonian:

$$H = |\varphi\rangle E_\varphi \langle\varphi| + \int \mathrm{d}E\, |E\rangle E \langle E| + \int \mathrm{d}E \left(|E\rangle V_E \langle\varphi| + |\varphi\rangle V_E^* \langle E| \right) \tag{5.7}$$

where the discrete state $|\varphi\rangle$ is embedded in a continuum of states $\{|E\rangle\}$ and coupled to this continuum via V_E. The Fano line shape appears when an external excitation mechanism, which shall be described by the transition operator T, transports mass from some initial state $|\phi_0\rangle$ into both $|\varphi\rangle$ and $|E\rangle$:

$$T|\phi_0\rangle = X_\varphi |\varphi\rangle + \int \mathrm{d}E\, X_E |E\rangle. \tag{5.8}$$

Note that $|\varphi\rangle$ and $|E\rangle$ are only eigenstates of the Hamiltonian without configuration interaction, i.e. when $V_E = 0$. The coupling V_E leads to a decay of $|\varphi\rangle$ into the continuum, which implies interference of two pathways into $|E\rangle$: the direct pathway ($X_E|E\rangle$) and a delayed pathway ($X_\varphi|\varphi\rangle$ with subsequent decay). This interference leads to a modified transition probability which gives rise to the line shape of the Fano resonance. In Ref. [39] this system was solved by diagonalizing above Hamiltonian resulting in eigenfunctions $|\tilde{E}\rangle$ (in the appendix 8.2 we give a more modern derivation), and the transition due to T was characterized by the cross section

$$\sigma(\mathcal{E}) = \frac{|\langle \tilde{E}|T|i\rangle|^2}{|\langle E|T|i\rangle|^2} = \sigma_0 \frac{(\mathcal{E}+q)^2}{\mathcal{E}^2+1} \tag{5.9}$$

with normalized energy $\mathcal{E} = \frac{E-E_\varphi-F_E}{\Gamma/2}$ where $E_\varphi + F_E$ is the position of the resonant line, Γ is the decay rate of the discrete state $|\varphi\rangle$, σ_0 is the φ-free cross section, and

$$q = \frac{\langle\varphi|T|\phi_0\rangle + \mathcal{P}\int \mathrm{d}E' \, \frac{V_E^*}{E-E'} \langle E'|T|\phi_0\rangle}{\pi V_E^* \langle E|T|\phi_0\rangle} \tag{5.10}$$

is the so-called Fano parameter. ($\mathcal{P}\int$ indicates a principal value integral.) In Ref. [39] the expression for q is assumed to be real without further explanation. As we show below, this is not always satisfied.

In the case of the Helium atom, $|\phi_0\rangle$ represents the ground state, $|\varphi\rangle$ is a doubly excited state like $2s2p$, and $|E\rangle$ represents the singly ionized continuum. The external excitation mechanism T can be an XUV laser pulse of appropriate wavelength, and the configuration interaction V_E is electron-electron interaction. (De-excitation by photon emission is orders of magnitude slower.) The interfering pathways are illustrated in figure 5.5.

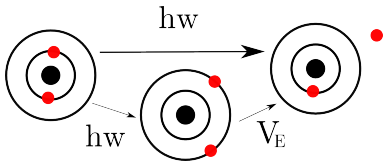

Figure 5.5: A cartoon illustrating the Fano interference phenomenon in case of the $2s2p$ doubly excited state of the Helium atom. The ground state $|\phi_0\rangle$ is depicted to the left, with the two electrons (red dots) on the innermost shell. The external excitation mechanism T in this case is an XUV laser pulse with appropriate photon energy $\hbar\omega$. It may either directly ionize the atom (upper pathway) or create a meta-stable excitation $|\varphi\rangle$ where both electrons are elevated to the second electronic shell (bottom pathway). This doubly excited state then decays via electron-electron interaction V_E into the same singly ionized continuum $|E\rangle$ with the ion in its ground state. The two pathways interfere which modifies the overall transition probability into the final state $|E\rangle$.

5.2.2 Line shape control

In recent years it was proposed to control the line shape by external fields and interactions, and schemes in diverse fields of physics were experimentally realized (see review in Ref. [40]). For a quantum dot system controlled by a time-independent magnetic field it was observed that a generalization to complex q was required to fit the control dependence of the line shape. Complex values of q result from the breaking of time-reversal symmetry by the magnetic field [41]. In contrast, in standard Fano theory [39], applicable to time-reversal symmetric systems, q is real valued [137]. Complex q has also been discussed as a signature of dephasing and decoherence in atoms [42, 43] as well as in quantum dots [44] and microwave cavities [45]. More generally, complex q is expected to appear whenever coupling to the environment or external fields turn the embedded state into a state that cannot be described by a real valued eigenfunction. In Ref. [5] we show that a time-dependent electric control field, specifically a linearly polarized IR probe pulse (parallel to the XUV), also generates complex q parameters. Thereby the implicit assumption of an instantaneous excitation T in original Fano theory, which implies that in equation (5.8) all X_E and X_φ share the same phase, breaks down. The external IR laser streaking field renders T non-instantaneous, as during the ongoing excitation process the populations in all $|E\rangle$ and $|\varphi\rangle$ may accumulate phases independently, and only after the excitation is completed does the undisturbed Fano decay proceed. If the IR is not too strong, the line shape remains well described by the

Fano situation (5.7) but the assumption of a real q needs to be dropped, see next section.

The effects of the IR streaking field on the spectrum and in particular on the resonant line shape were studied with numerical experiments and are described in the following paragraphs. For the numerical computation of spectra we employed both the full two-electron basis (Sec. 3.1.2) and the haCC approach (Sec. 5.1.2), which are both equally well suited.

5.2.2.1 Dipole selection rules

First of all, the dipole selection rules determined by the pure XUV transition are abrogated. The left plot in figure 5.6 shows photo-electron probability maxima within odd angular momentum partial waves at energies $-I_p + (2n-1)\hbar\omega$, $n \in \mathbb{N}$, and maxima with even angular momentum at energies $-I_p + 2n\hbar\omega$, $n \in \mathbb{N}$. Every absorbed photon may change the angular momentum of the electron by ± 1, which leads to this simple behavior. In the presence of the weak IR field, ionized electrons are modified and may thereby exchange angular momenta with the streaking field. Thus the photo-electron peak at $-I_p + \hbar\omega$ at 35 eV consists of all, even and odd, angular momentum components. Convergence of photo-electron spectra with and without streaking field was achieved with $l_{\max} = 5$ and a box size of 50 a.u. discretized with 10 finite elements of order 12. The large box size is required for correct representation of high lying resonances like $2s5p$.

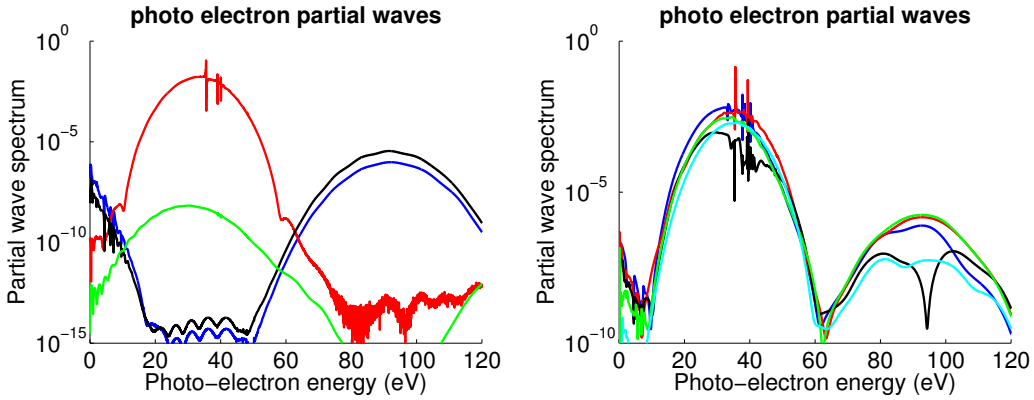

Figure 5.6: Photo-electron partial wave spectrum ($P_{lm}(E)$ in Eq. (3.7); in this section P and σ are used interchangeably) of Helium subjected to a 21 nm ($\hbar\omega \approx 59$ eV) excitation pulse without (left) and with (right) an additional few cycle IR streaking field of wavelength 730 nm and intensity $2 \cdot 10^{14}$ W/cm^2 temporally overlapping with the XUV pulse. The first four partial waves $l = 0$ (black), $l = 1$ (red), $l = 2$ (blue) and $l = 3$ (green) are shown. Without IR field, the single-photon transition leads to a photo-electron peak at 35 eV which consists of odd angular momenta only, and is dominated by $l = 1$ with the $2s$Np Fano line shape series clearly visible. With IR the partial waves get mixed, and several other line shapes appear.

5.2.2.2 Modified line shapes

Second, the Fano resonant line shapes are transformed. This implies that the lines with total angular momentum equal to one (i.e. the entire $2sNp$ series) change shape, but also other resonant lines with other angular momenta appear (the lines around 35 eV in partial waves $l = 0$ and $l = 2$ in Fig. 5.6). A zoom around the $2sNp$ line shapes is shown in figure 5.7 for various time delays between the excitation XUV pulse and the weak IR streaking field.

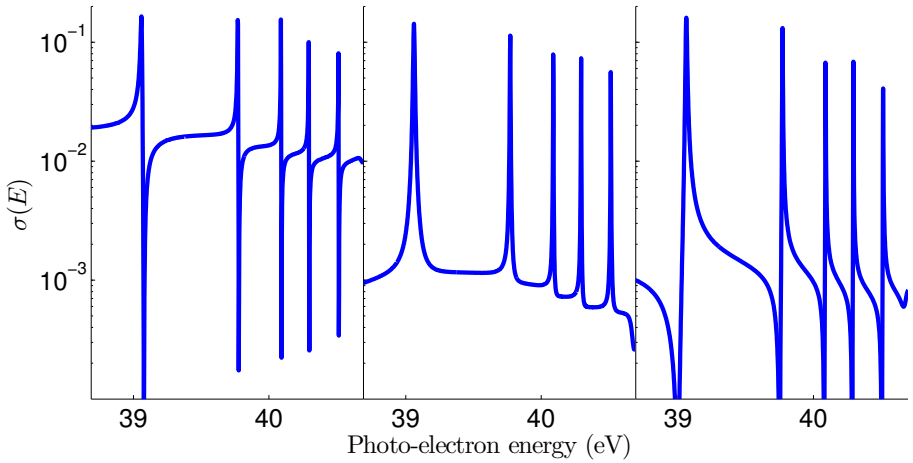

Figure 5.7: Zoom into the $2sNp$ Fano series visible in the photo-electron partial wave $l = 1$ for various time delays between XUV excitation and IR streaking pulse (730 nm and $2 \cdot 10^{14}$ W/cm^2). Left: Without IR all lines are perfectly described by a classical Fano line shape with $q \approx -3$. Middle: XUV excitation near a zero of the IR electric field strength, Lorentzian line shape with $|q| \to \infty$. Right: XUV excitation near a maximum of the IR electric field strength, "anti-Fano" line shape with $q \approx +5$. The entire series of Fano resonances undertakes a synchronized transition of the line shapes.

It can be seen in figure 5.7 that positions and widths of the line shapes are unmodified, but their shapes change in unison. This indicates that a universal characterization of the line shape modification is possible, as the details of the involved doubly excited state seem to be of negligible importance. The full streaking analysis is encaptured in figure 5.8, where the $2s2p$ resonance is shown for a wide range of time delays t_0 between IR and XUV. In particular we observe line shape modifications on the sub-femtosecond time scale in the temporal overlap regime. With an IR optical cycle (opt. cyc.) corresponding to ≈ 2.4 fs, full transitions from Lorentzian to Fano line shapes or the other way around happen within nearly half a femtosecond of time delay variations.

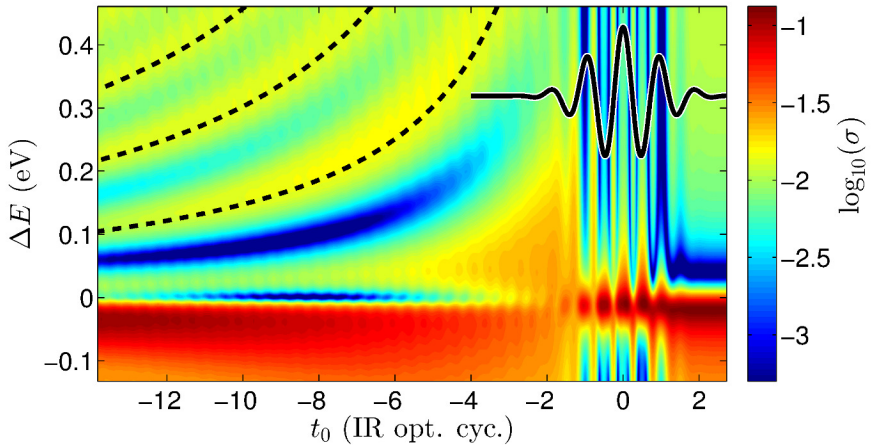

Figure 5.8: Streaking spectrogram of the $2s2p$ resonant line shape of Helium with an IR streaking pulse of wavelength 730 nm and intensity $2 \cdot 10^{14}\,\mathrm{W/cm^2}$, indicated by the black solid line (Eq. (8.26) with $n = 2$, $m = 8$). Positive $t_0 > 0$ imply the XUV excitation coming after the IR field maximum, large negative time delays $t_0 \ll 0$ imply that the IR pulse does not modify the excitation process, but only the Fano decay. It can be seen that for $t_0 \gtrsim 2$ the original undisturbed Fano line shape persists as the IR is too weak to modify the Helium ground state. In the overlap regime of the two pulses the spectrum shows oscillatory modifications of the line shape, from Fano through Lorentz until anti-Fano, see figure 5.7. For $t_0 \lesssim -2$ the original Fano line shape reappears, albeit with sidebands, which have a well defined behavior as indicated by the black dashed lines, see next section. Figure taken from Ref. [5].

All other resonances show similar behavior, as is exemplified in Fig. 5.9 for the $2s3s$ resonance. It only becomes visible in the temporal overlap regime of IR and XUV pulses with a total angular momentum of $l = 0$.

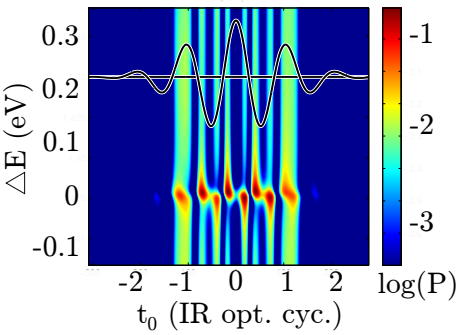

Figure 5.9: The $2s3s$ resonance line shape on the $l = 0$ partial wave of the photo-electron spectrum of Helium generated by an XUV excitation subjected to a 730 nm and intensity $2 \cdot 10^{14}\,\mathrm{W/cm^2}$ streaking pulse, indicated by the black line. For temporal overlap between XUV and IR, the $l = 0$ partial wave is visible and exhibits the $2s\mathrm{N}s$ series of doubly excited state resonant line shapes, where again synchronized modifications are observed (not shown).

To summarize, we observe the same behavior for all resonant line shapes in the temporal overlap regime of IR and XUV pulses ($|t_0| \lesssim 2$ IR opt.cyc.): Synchronized line shape modification on the attosecond time scale.

5.2.2.3 Oscillatory sidebands

If the IR comes truly after the XUV we can observe oscillating sidebands with well defined frequency. Similar structures also appear at $E_- := E_\varphi - 2\hbar\omega_{IR}$, see Fig. 5.10 (left). These wiggles can be identified with two-IR-photon couplings, which are not included in the standard Fano model (5.7). The electron amplitude generated by two-photon absorption near $E_+ := E_\varphi + 2\hbar\omega_{IR}$ is super-imposed with the higher lying Fano resonances and therefore not clearly discernible. Absorption-emission transitions couple the embedded state to the continuum near $E \approx E_\varphi$. We model the spectral features near E_β ($\beta = \varphi$ or $\beta = -$) by

$$\sigma(E) = |f(E) + \mathcal{E}_0^2 \mathrm{e}^{-\mathrm{i}t_0(E-E_\beta)} b_\beta(E)|^2 \tag{5.11}$$

where $\mathcal{E}_0$ denotes the IR peak field strength, and $f(E)$ is the spectral amplitude in absence of the IR. The unknown two-IR-photon transition amplitudes are parametrized as

$$b_\beta(E) \;=\; c_\beta g(E - E_\beta). \tag{5.12}$$

For g we use a Gaussian profile with a fixed width equal to the spectral width of the IR. The only adjustable parameters are the two-photon coupling strengths c_β, accounting for the different strengths of the transition into structured and unstructured continuum. In figure 5.10 the cross-section (5.11) at $t_0 = -12$ IR opt. cyc. is compared to the TDSE result. The fringe separation of $2\pi/t_0$ discernible in Figs. 5.8 and 5.10 proves that the structures

are caused by interference of photo-electrons emitted at relative delay t_0. Without any further adjustment of c_β or g the model equally well reproduces the spectra for varying intensities up to $10^{12}\,\mathrm{W/cm^2}$ and for all t_0. The found quadratic dependence on the IR field strength $\mathcal{E}_0$ shows that this is a true two-photon process without resonant coupling to neighboring states. At short time-delays $t_0 \gtrsim -4$ IR opt. cyc. the effect is negligible, as fringe separation diverges and fringes are hardly discernible.

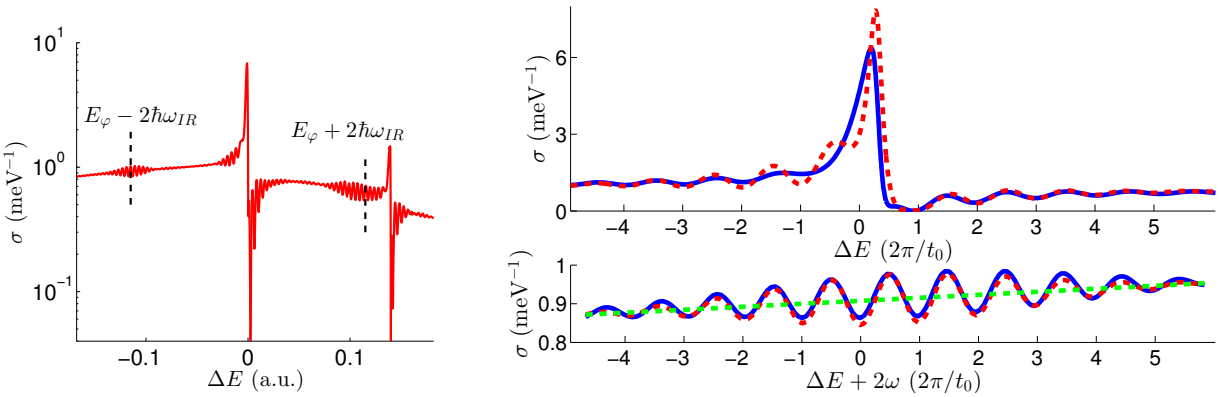

Figure 5.10: Left: Overview of the $l = 1$ partial wave around the $2s2p$ resonance for $t_0 = -12$ IR opt. cyc.. Sidebands can be seen at the resonance position $\Delta E = 0$ and at $E_- = E_\varphi - 2\hbar\omega_{IR}$, $\hbar\omega_{IR} \approx 0.06$. Sidebands at $E_+ = E_\varphi + 2\hbar\omega_{IR}$ overlap with the $2s3p$ resonance at $\Delta E \approx 0.14\,\mathrm{a.u.}$. Right: Two-photon interference resonance near E_φ (upper panel) and near E_- (bottom panel). Cross section (5.11) (red dashed) is compared to the full numerical result (solid blue). In the bottom plot also the back ground slope is indicated (green dashed). Figure taken from Ref. [5].

5.2.3 Complex q

In the following we propose a theoretical explanation for the line shape modifications in the temporal overlap regime and verify its validity by comparing to our numerical data.

5.2.3.1 Partial wave basis

The description of the line shape modifications requires correct inclusion of angular momenta, i.e. we start by expanding the Fano Hamiltonian into spherical harmonics:

$$H = |\varphi\rangle E_\varphi \langle\varphi| + \sum_{l,m,k} |l,m,k\rangle E_{l,m,k} \langle l,m,k| + \sum_{l,m,k} \Big(|l,m,k\rangle V_{l,m,k} \langle\varphi| + |\varphi\rangle V^*_{l,m,k} \langle l,m,k| \Big) \tag{5.13}$$

with $V_{l,m,k} = \delta_{l,1}\delta_{m,0}V_k$ for the $l = 1$ resonances $2s\mathrm{N}p$, $E_{l,m,k} = \frac{k^2}{2}$, $\sum_k \equiv \int_0^\infty k^2 \mathrm{d}k$ and

$$\langle \vec{r} | l,m,k \rangle \quad = \quad \sqrt{\frac{2}{\pi}} j_l(kr) Y_l^m(\Omega_r) \tag{5.14}$$

where j_l are spherical Bessel functions and Y_l^m are spherical harmonics. We may diagonalize this (see appendix 8.2) and obtain

$$|\tilde{k}\rangle := |1,0,\tilde{k}\rangle = \frac{\sin\Delta}{\pi V_k k}|\Phi\rangle - \cos\Delta|1,0,k\rangle \tag{5.15}$$

where $|\Phi\rangle = |\varphi\rangle + \mathcal{P}\int \mathrm{d}E_{k'}\,|k'\rangle\frac{k'V_{k'}}{E_k - E_{k'}}$, $\tan\Delta = -\frac{\pi|V_k|^2 k}{E_k - E_\varphi - F_{E_k}}$ and $F_{E_k} = \mathcal{P}\int \mathrm{d}E_{k'}\,\frac{k'|V_{k'}|^2}{E_k - E_{k'}}$. In full analogy to Fano's original theory, Sec. 5.2.1, we define the initial state

$$|\psi_0\rangle := T|\phi_0\rangle = |\varphi\rangle X_\varphi + \int \mathrm{d}^3k\,|\vec{k}\rangle X_{\vec{k}} \tag{5.16}$$

which leads to the normalized cross section

$$\sigma(\mathcal{E}) = \frac{|\langle\tilde{k}|\psi_0\rangle|^2}{|\langle k|\psi_0\rangle|^2} = \sigma_0\frac{|\mathcal{E}+q|^2}{\mathcal{E}^2+1} \tag{5.17}$$

with

$$q = \frac{1}{\pi V_k^* k}\frac{\langle\Phi|\psi_0\rangle}{\langle k|\psi_0\rangle}, \tag{5.18}$$

$\mathcal{E} = \frac{E_k - E_\varphi - F_E}{\Gamma/2}$ and $\Gamma = 2\pi|V_k|^2 k$.

5.2.3.2 Modified initial state

We now include the effect of a temporally extended IR pulse into the theory.

The explicit computation of the cross section employs the strong field approximation, see Sec. 1.4.3. Only phase modification and momentum boost by the external dipole field are taken into account. In this approximation, the time-evolution in the IR dipole field from a state with momentum $\vec{k} - \vec{A}_{\mathrm{IR}}(t_0)$ at t_0 until the end of the pulse at t_1, where it has the final momentum $\vec{k}$, is given as

$$U_{IR}|\vec{k} - \vec{A}_{\mathrm{IR}}(t_0)\rangle = \mathrm{e}^{-\mathrm{i}\int_{t_0}^{t_1}\mathrm{d}t\,(\vec{k}-\vec{A}_{\mathrm{IR}}(t))^2/2}|\vec{k}\rangle. \tag{5.19}$$

The effect of the IR pulse on the embedded state $|\varphi\rangle$ is assumed to be a modification of its phase according to the Stark-shifted energy $E_\varphi(t)$:

$$|\varphi\rangle(t_1) = \mathrm{e}^{-\mathrm{i}\int_{t_0}^{t_1}\mathrm{d}t\,(E_\varphi + \Delta E_\varphi(t))}|\varphi\rangle(t_0). \tag{5.20}$$

We may neglect the coupling $V_{\vec{k}}$ between $|\varphi\rangle$ and $|\vec{k}\rangle$ for the duration of the IR, as the decay of all resonances occurs on much longer time scales. Thus, we can insert these time evolutions into Eq. (5.16) to obtain the modification of the initial wave packet $|\psi_0\rangle$ by the IR pulse in the time interval from its creation by the XUV at t_0 until t_1

$$|\psi_1\rangle := |\varphi\rangle X_\varphi + \int \mathrm{d}^3k\,\mathrm{e}^{-\mathrm{i}\Phi_{\vec{k}}}|\vec{k}\rangle X_{\vec{k}-\vec{A}_{\mathrm{IR}}(t_0)}. \tag{5.21}$$

The phase offset $\Phi_{\vec{k}}$ between embedded and continuum states, accumulated from excitation at t_0 until the end of the IR pulse at t_1, $A_{\mathrm{IR}}(t_1) = 0$, is

$$\Phi_{\vec{k}} = \int_{t_0}^{t_1} \mathrm{d}t \left((\vec{k} - \vec{A}_{\mathrm{IR}}(t))^2/2 - E_\varphi - \Delta E_\varphi(t) \right). \tag{5.22}$$

Even if the initial amplitudes X_φ and $X_{\vec{k}-\vec{A}_{\mathrm{IR}}(t_0)}$ are all real, the interaction with the IR imprints a phase modulation on $|\psi_1\rangle$. Such an energy-dependent phase-imprint on the initial wave-packet $|\psi_1\rangle$ is generic for short-time controls. After the end of the control pulse the evolution is governed by the Fano-Hamiltonian (5.13), but the matrix elements $\langle\varphi|\psi_0\rangle$ and $\langle k|\psi_0\rangle$ in Eq. (5.18) are replaced with $\langle\varphi|\psi_1\rangle$ and $\langle k|\psi_1\rangle$, which no longer share the same phase. As a result the modulated q parameter becomes complex.

5.2.3.3 Modified line shape

The dipole transition matrix element from an initial $l = 0$ state has the general form $X_{\vec{k}} = (\hat{\epsilon} \cdot \vec{k}) Z_{|\vec{k}|}$ for polarization direction $\hat{\epsilon}$. We neglect the $|\vec{k}|$-dependence of $Z_{|\vec{k}|} \equiv Z$, as the spectral width of the chosen XUV excitation pulse is much larger than the resonance width Γ. Also the energy dependence of the transition to the structureless continuum states $|k\rangle$ far from threshold can be considered negligible across Γ. We expand $\Phi_{\vec{k}}$ into spherical harmonics and project out the $l = 1$ partial wave of $|\psi_1\rangle$:

$$|Y_1^0\rangle\langle Y_1^0|\psi_1\rangle = |\varphi\rangle \mathrm{e}^{-\mathrm{i}\int_{t_0}^{t_1} \mathrm{d}t\, E_\varphi(t)} X_\varphi + \int \mathrm{d}k\, k^2 |k\rangle \mathrm{e}^{-\mathrm{i}(t_1-t_0)k^2/2 - \mathrm{i}\chi} \sqrt{\frac{4\pi}{3}} k Z \mathcal{J}(k) \tag{5.23}$$

with

$$\mathcal{J}(k) = j_0\big(k|\vec{\alpha}|\big) - 2j_2\big(k|\vec{\alpha}|\big) - 3\mathrm{i} j_1\big(k|\vec{\alpha}|\big) \frac{\vec{\alpha} \cdot \vec{A}_{\mathrm{IR}}(t_0)}{k|\vec{\alpha}|} \tag{5.24}$$

$$\vec{\alpha} = \int_{t_0}^{t_1} \mathrm{d}t\, \vec{A}_{\mathrm{IR}}(t) \tag{5.25}$$

$$\chi = \int_{t_0}^{t_1} \mathrm{d}t \left(\Delta E_\varphi(t) - \frac{\vec{A}_{\mathrm{IR}}(t)^2}{2} \right). \tag{5.26}$$

This results in a modified q parameter

$$q_{\mathrm{IR}} = \frac{1}{\pi V_k^* k} \frac{\langle\Phi|\psi_1\rangle}{\langle k|\psi_1\rangle} \tag{5.27}$$

where for the evaluation of the principal value integral we neglect the k-dependence of $\mathcal{J}$

$$\mathcal{P} \int k'^2 \mathrm{d}k' \, \frac{V_{k'}^*}{E_k - E_{k'}} \langle k'|\psi_1\rangle \approx \mathcal{J}(k) \mathrm{e}^{-\frac{\mathrm{i}}{2}\int A_{\mathrm{IR}}^2} \mathcal{P} \int k'^2 \mathrm{d}k' \, \frac{V_{k'}^*}{E_k - E_{k'}} \mathrm{e}^{-\mathrm{i}(t_1-t_0)k^2/2} \langle k'|\psi_0\rangle. \tag{5.28}$$

Note that $\langle k'|\psi_0\rangle = \frac{4\pi}{3}k'Z$. We find for the $l=1$ component

$$q_{IR} = \frac{1}{\pi V_k^* k}\Big(\frac{\langle\Phi|U_0|\psi_0\rangle}{\langle k|U_0|\psi_0\rangle} + \frac{\langle\varphi|U_0|\psi_0\rangle}{\langle k|U_0|\psi_0\rangle}\big(\mathrm{e}^{-\mathrm{i}\chi}/\mathcal{J}(k) - 1\big)\Big) \tag{5.29}$$

where U_0 is the free time evolution during the time interval $[t_0, t_1]$ in absence of the IR and without the coupling $V_k = 0$. It is given by $U_0|k\rangle = \mathrm{e}^{-\mathrm{i}(t_1-t_0)k^2/2}|k\rangle$ and $U_0|\varphi\rangle = \mathrm{e}^{-\mathrm{i}(t_1-t_0)E_\varphi}$. The effect of U_0 on the q parameter is negligible for time intervals that are short compared to the decay time: $t_1 - t_0 \ll 1/\Gamma$:

$$\frac{\langle\Phi|\psi_0\rangle}{\langle k|\psi_0\rangle} \approx \frac{\langle\Phi|U_0|\psi_0\rangle}{\langle k|U_0|\psi_0\rangle} \qquad \text{and} \qquad \frac{\langle\varphi|\psi_0\rangle}{\langle k|\psi_0\rangle} \approx \frac{\langle\varphi|U_0|\psi_0\rangle}{\langle k|U_0|\psi_0\rangle}. \tag{5.30}$$

With this, the first term in Eq. (5.29) can be identified with field free Fano parameter q_{noIR}, and thus we get

$$q_{\mathrm{IR}} = q_{\mathrm{noIR}} + a\Big(\mathrm{e}^{-\mathrm{i}\chi}/\mathcal{J}(k) - 1\Big). \tag{5.31}$$

The prefactor $a = \langle\varphi|\psi_0\rangle/(\pi V_k^* k\langle k|\psi_0\rangle)$ denotes the ration of embedded to continuum amplitudes in absence of the IR pulse.

5.2.3.4 Comparison with numerical data

Expression (5.31) can be put to the test by comparing with numerical data. Figure 5.11 (left) shows the complex valued q parameter of the $2s2p$ resonance as predicted by Eq. (5.31) and as extracted from the spectrogram of Fig. 5.8. For this comparison we neglected Stark shifts, $\Delta E_\varphi(t) = 0$, and took $a = -3.3$ by fitting to the field free resonant line shape. Sign changes of the real part and peaks in the imaginary parts are all well reproduced. Quantitative deviations must be expected due to the employed approximations, most importantly the strong field approximation (plane waves $|\vec{k}\rangle$ instead of the exact scattering solutions).

There are excitation times t_n where the spatial offset vanishes, $\vec{\alpha} = 0$, and therefore $\mathcal{J} = 1$, Eq. (5.24). At these delays, the imaginary part of q is exclusively due to the phase-shifts χ, Eq. (5.26). Up to small corrections arising from the short IR pulse duration, the t_n coincide with zeros of the field. At the t_n the profile is Fano-like, except that the characteristic minimum remains slightly above zero. In our model, the minima for subsequent t_n's grow monotonically as the delay $|t_0|$ increases (figure 5.11, right) reflecting the accumulation of the shift χ.

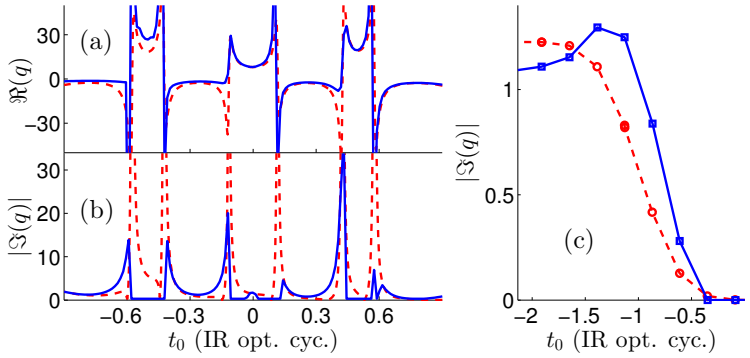

Figure 5.11: Dependece of q on the time delay t_0 between IR and XUV for the $2s2p$ resonance. Numerical data (solid blue) and analytical prediction (5.31) (red dashed) agree well. (a),(b): Real and imaginary parts of q respectively. (c): Imaginary part of q at times t_n where $\vec{\alpha} = 0$ shows the effect of χ, equation (5.26).
Figure taken from Ref. [5].

A similar qualitative agreement is given by the higher resonances $2s\mathrm{N}p$, $\mathrm{N} \geq 3$. Thereby the value for the prefactor in Eq. (5.31) was adjusted slightly: $a = -5$.

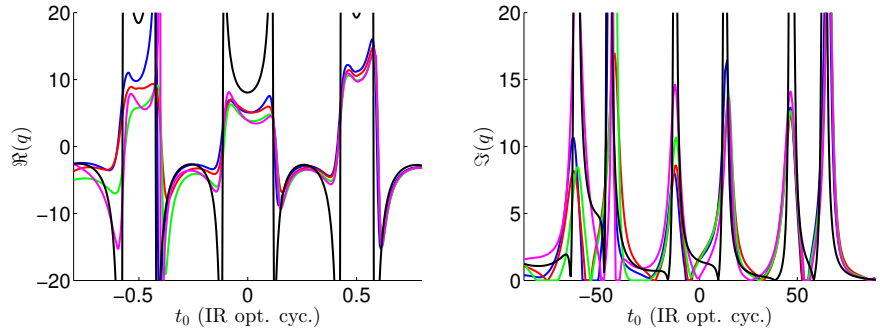

Figure 5.12: Real (left) and imaginary (right) parts of q for the resonances $2s3p$ (blue), $2s4p$ (red), $2s5p$ (green) and $2s6p$ (magenta) as extracted from numerical computations show synchronized dependence on the offset time t_0, and agree qualitatively with the prediction (black line), Eq. (5.31).

In summary, we expect anomalous Fano profiles with complex q parameter to appear whenever a non-trivial relative phase between embedded state and continuum is imprinted on the system during the Fano decay. Such a phase can reflect internal dynamics of the embedded state $|\varphi\rangle$, i.e. when it is not strictly an eigenstate of a stationary Hamiltonian, as for decaying states and decoherence. It can equally be generated by an external control, as demonstrated here. Our theoretical description of the process should be generalizable to systems where we can model the impact of the control on bound and embedded states

and when control time is short compared to the resonance life time. This is the case for laser pulses on atoms or molecules, but the approach is also valid, e.g., for time-dependent electric or magnetic fields acting on quantum dots.

5.2.4 Transient absorption spectra

Similar to our expression (5.31), they developed a theory for the Fano line shapes in transient absorption spectra (TAS) in Ref. [138] and tested it against experimental data. Without IR pulse, photo-electron spectra (PES) and TAS from an XUV pulse alone are perfectly related to each other: Energy absorbed by the target atom must lead to ionization and thus directly leads to photo-electron signal at the detector at energies peaked at $-I_p + n\hbar\omega$, $n \in \mathbb{N}$. Because the XUV photon energy exceeds the first ionization potential, single-photon ionization into the groundstate channel dominates, and the presence of excited channels is negligible. The absorbed energy must be missing in the pulse, which directly leads to TAS. Indeed, in numerical computations TAS and PES coincide perfectly without IR. (The formula for extracting TAS from TDSE results is summarized in the appendix 8.1.)

However, in the presence of the IR pulse the relation is not that straightforward, as energy may be absorbed from (or deposited into) either the XUV or the IR. The resulting spectra from photo-ionization and transient absorption differ in many aspects in this case.

The theory in Ref. [138] predicts

$$\sigma(\mathcal{E}) = \sigma_0 \cdot \left(\frac{q_{\mathrm{noIR}}^2 + 1}{q_{\mathrm{IR}}^2 + 1} \cdot \frac{(\mathcal{E} + q_{\mathrm{IR}})^2}{\mathcal{E}^2 + 1} + 1 - \frac{q_{\mathrm{noIR}}^2 + 1}{q_{\mathrm{IR}}^2 + 1} \right) \tag{5.32}$$

with

$$q_{\mathrm{IR}} = -\cot\frac{\varphi_{\mathrm{IR}}}{2} \tag{5.33}$$

$$\varphi_{\mathrm{IR}} = \varphi_{\mathrm{noIR}} - \int_{t_0}^{\infty} \mathrm{d}t\, \Delta E(t). \tag{5.34}$$

Here φ_{noIR} satisfies $q_{\mathrm{noIR}} = -\cot(\varphi_{\mathrm{noIR}}/2)$ and $\Delta E(t)$ is the energy shift of the resonance due to the IR pulse. For high lying resonances $2s\mathrm{N}p$ with $\mathrm{N} \geq 4$ it is dominated by the ponderomotive shift

$$\Delta E(t) = \frac{A_{\mathrm{IR}}^2(t)}{2}. \tag{5.35}$$

Comparing this with our numerical computations we find nearly perfect agreement:

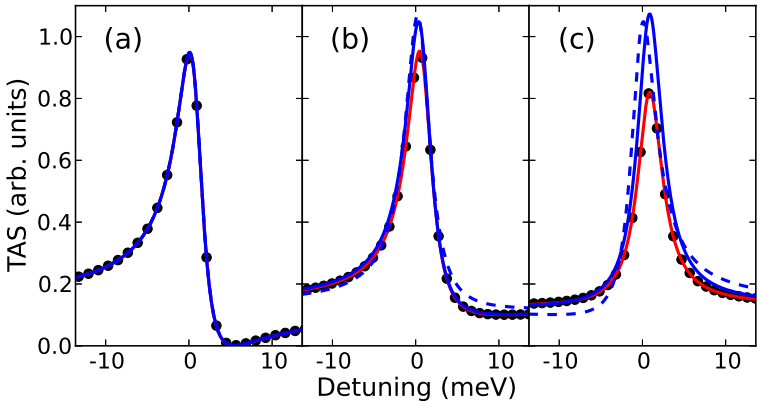

Figure 5.13: Transient absorption cross section around the $2s4p$ resonance. Numerical results (dots) are compared to fits with complex q (solid red), fits with real q_{IR} (solid blue) in Eq. (5.32) and the predicted q_{IR} (dashed blue) assuming only a ponderomotive shift by Eq. (5.35). (a): In the field free case both complex and real q reproduce the numerical data perfectly. (b): At $t_0 = 0$ both predicted $q_{\mathrm{IR}}(t_0 = 0) = -11$ and fitted $q_{\mathrm{IR}}(t_0 = 0) = -5.8$ show slight discrepancies. (c): Also at $t_0 = 5\,\mathrm{fs}$ predicted $q_{\mathrm{IR}}(t_0 = 5\,\mathrm{fs}) = 5.7$ and fitted $q_{\mathrm{IR}}(t_0 = 5\,\mathrm{fs}) = 20$ can not achieve perfect agreement, in contrast to the fit with complex q.

Interestingly, the Fano cross section $\sigma(\mathcal{E})$ (5.32) for TAS introduces the line shape modification not via complex q as in our theory for PES, but through a modified real q together with an explicit pedestal. As is shown in Fig. 5.13, also an unmodified Fano profile (i.e. no pedestal but with complex q) as Eq. (5.17), fits the numerical results. This suggests, that an alternative description of the TAS cross section with complex q could be possible, which may very well turn out to be equivalent to the theory presented in Ref. [138].

Chapter 6

Double ionization

6.1 Motivation

This chapter reports results accepted for publication in Phys. Rev. A [6].

Understanding the quantum dynamics of the three body Coulomb problem is a fundamental and ongoing challenge. As one of the most elementary realizations, the Helium atom has been examined extensively over the past few decades, in particular the breakup process initiated by short and intense laser pulses. Analyzing the dynamics and the importance of correlation in this simple process is a first step for understanding more complex many-body phenomena.

A multitude of mechanisms have already been identified for the various intensity and wavelength regimes. For example, at long laser wavelengths in the near infrared (IR) and at high intensities, double ionization (DI) is well described by two independent sequential tunnel ionization events. At lower intensities, however, the predicted efficiency for the liberation of the second electron is far too small. The experimentally observed enhancement of DI yield by several orders of magnitude compared to the expectation from a purely sequential process, referenced to as the "knee" [47, 139], appears not just in Helium but in many atoms and molecules [49], and represents one of the most dramatic manifestations of dynamical electron-electron correlation in nature [140].

To explain the discrepancy various so-called non-sequential double ionization (NSDI) mechanisms have been proposed, all following the recollision scenario introduced by the three-step-model (Sec. 1.4.4). Thereby the recolliding electron can interact with the second electron and the nucleus in various ways. It may directly dislodge the second electron leading to simultaneous ejection (SE) of both electrons, also called the direct pathway. It may also lift the second electron to an excited state from which the field can ionize it on its own, also called recollision induced excitation with subsequent ionization (RESI) or the delayed pathway [50, 51]. The first electron may even form a bound compound with the second electron and the nucleus which survives for at least a quarter of a cycle (doubly delayed ejection, DDE) [52], a process which can also occur when the kinetic energy of the recolliding electron is smaller than the excitation energy of the ion. How all these

mechanisms work in detail and interact with each other is not yet fully understood, it is even unclear if these are all involved possible DI pathways or if yet unthought of ones play a role. In order to further understand the dynamics accurate benchmark data for model comparisons is needed.

Another process that has received significant attention is two-photon DI of the Helium atom. This occurs in the extreme ultraviolet (XUV) when the energy of two photons suffices for DI and it dominates up to the threshold for single-photon DI. The process necessarily probes correlation dynamics, most simply by shake-up into an excited ionic state during detachment of the first electron, followed by second ionization of the excited ionic state. Also more direct processes were considered, that involve correlated initial and final states [141]. In numerical simulations, consensus appears to be arising in recent literature, also for photon energies $\omega \approx 40\,\mathrm{eV} \sim 54\,\mathrm{eV}$ where the sequential channel is closed [27].

At present, the most complete experimental tests for the mechanisms discussed above are provided by detecting, in coincidence, the momenta of two particles from the fully fragmented state consisting of the two ionized electrons and the remaining ion. Sophisticated momentum imaging techniques like COLTRIMS [142] and continued advances in laser technologies have opened up the possibility to study the correlated three-particle Coulomb breakup in Helium experimentally on its intrinsic time-scales, see for example Refs. [143–147]. Due to the high binding energies of the Helium atom and the resulting low efficiency of laser induced ionization, many DI experiments are performed with other targets, such as Neon atoms [147] or Argon atoms [22, 148–151]. Final state correlations are one of the more accessible observables, but also more convoluted questions are being investigated, like the exact release time of the electrons [22]. Although experimentally more challenging, data for Helium is often preferable because the additional electrons in the multi-electron targets complicate analysis and model building.

Apart from the discussion of simplifying models, significant effort has been invested into numerical computations. The main goal is to obtain reliable benchmark data that is not obscured by experimental limitations. Advances in numerical techniques and ever increasing computational resources allowed for extensive *ab initio* calculations of the Helium system. At short laser wavelengths, where dynamics are initiated by the absorption of only few photons, fully differential photo-electron spectra and cross sections have been computed using a wide array of methods. While time-independent approaches like lowest order perturbation theory [152] or R-matrix Floquet theory [153, 154] have also been successfully applied, mostly the time-dependent Schrödinger equation (TDSE) was solved numerically in full dimensionality, see for example Refs. [27, 53, 65, 71–74, 155]. At longer wavelengths computations remain challenging. The reason is the inapplicability of perturbative approaches, which only allows for time-dependent non-perturbative methods, combined with their rather unfavorable scaling of the necessary computational power with wavelength and intensity, see Sec. 2.2.1. As a consequence, already at the near visible wavelength of $\lambda \sim 400\,\mathrm{nm}$ full dimensional numerical computations are scarce [28–30]. Progress at longer wavelengths like the experimentally relevant

Ti:sapphire wavelength of 780 nm has only been made recently. Weak infrared (IR) dressing fields, unable to ionize on their own, were combined with XUV pulses in Ref. [73] to study their effect on joint energy distributions for coplanar emission. Hu [31] used a precisely timed XUV pulse to enhance photo-absorption from a single cycle IR streaking field of moderate intensity.

Using the tSurff method for double emission (Sec. 2.2) we are able to compute accurate *ab initio* DI spectra at both XUV and IR wavelength with significantly reduced numerical effort. In the XUV regime, we reproduce results from literature and corroborate the consensus that has emerged in recent publications for the observables such as the total DI cross section, two-electron energy distributions and triply differential cross sections. Compared to literature, we were able to significantly reduce the computational effort. At the near IR wavelength of 780 nm, we present fully differential spectra for intensities up to $4 \cdot 10^{14}\,\mathrm{W/cm^2}$ and pulse durations $\gtrsim 10\,\mathrm{fs}$. The measured single-to-double ionization ratio — the IR double-ionization "knee" — is reproduced to within estimated $\sim 50\%$ accuracy. We further present two-electron energy distributions and up to five-fold differential electron spectra.

Throughout, convergence is studied systematically and provides error estimates from below 1% in the XUV regime to $\lesssim 60\%$ for a large part of the IR data. These error estimates consent with the comparison to other calculations and experimental data, where available. The five-fold differential spectra at IR wavelength must be considered only as qualitative results, as convergence could not yet be achieved. For quantitative analysis we suggest a measure of correlation that is directly applicable to experimental double-emission spectra.

6.2 Observables

We now introduce the various physical quantities which will be examined in this chapter. All observables are derived from the fully differential photo-electron spectrum, which we will simply call the probability density of the two ionized electrons

$$P(E_1, E_2, \Omega_1, \Omega_2) = k_1 k_2 P(\vec{k}_1, \vec{k}_2) \tag{6.1}$$

with $P(\vec{k}_1, \vec{k}_2) = |b(\vec{k}_1, \vec{k}_2)|^2$, see Eq. (2.45). The E_i are the final kinetic energies and $\Omega_i \equiv (\theta_i, \varphi_i)$ are the emission angles. For the here considered linearly polarized pulses, the spectra are independent of the sum of the azimuthal angles $\varphi_1 + \varphi_2$. The total DI yield is given by

$$Y := \iiiint \mathrm{d}E_1 \mathrm{d}E_2 \mathrm{d}\Omega_1 \mathrm{d}\Omega_2 \, P(E_1, E_2, \Omega_1, \Omega_2). \tag{6.2}$$

In the regime of multi-photon perturbation theory, one can define the total N-photon cross section as

$$\sigma_N := \frac{\omega^N Y}{\int \mathrm{d}t \, I(t)^N}, \tag{6.3}$$

where $I(t)$ is the laser intensity profile and ω is the photon energy (see Refs. [27, 71] and references therein). Another popular quantity is the triply differential cross section (TDCS) defined as

$$\frac{\mathrm{d}\sigma_N}{\mathrm{d}E_1\mathrm{d}\Omega_1\mathrm{d}\Omega_2} := \frac{\omega^N}{\int \mathrm{d}t\, I(t)^N} \int \mathrm{d}E_2\, P(E_1, E_2, \Omega_1, \Omega_2) \tag{6.4}$$

which is typically evaluated in coplanar geometry ($\varphi_{1/2} \in \{0, \pi\}$ for polarization axis in z-direction). This observable is experimentally accessible as a nuclear recoil momentum distribution, as summarized in Ref. [71]. These cross sections take into account the Fourier width of the pulse by the energy integrations. Therefore, as long as the photon energy is defined sharply enough that no alternate reaction channels open up they are in good approximation independent of the exact pulse shape.

In contrast, the energy probability distribution, given by

$$P(E_1, E_2) := \iint \mathrm{d}\Omega_1 \mathrm{d}\Omega_2\, P(E_1, E_2, \Omega_1, \Omega_2) \tag{6.5}$$

sensitively depends on the exact pulse shape. The same holds true for the joint angular distribution (JAD) at fixed energies E_1 and E_2,

$$P_{E_1,E_2}(\theta_1, \theta_2) := P(E_1, E_2, \Omega_1, \Omega_2)\Big|_{\varphi_{1/2}\in\{0,\pi\}} \tag{6.6}$$

where the polar angles $\theta_{1/2} \in [0, 2\pi)$ both scan the entire $\varphi = 0/\pi$ plane. JADs may exhibit several symmetries. For linearly polarized pulses the spectrum is invariant under rotations around the polarization z-axis, in particular a rotation by π: $(\varphi_1, \varphi_2) \to (\varphi_1 + \pi, \varphi_2 + \pi)$. This implies $P(\theta_1, \theta_2) = P(2\pi - \theta_1, 2\pi - \theta_2)$. For long pulses, where the distinction between $+z$ and $-z$ direction disappears, the spectrum additionally satisfies $P(\theta_1, \theta_2) = P(\pi - \theta_1, \pi - \theta_2)$. And at equal energy sharing points $E_1 = E_2$, exchanging the angles $P(\theta_1, \theta_2) = P(\theta_2, \theta_1)$ is equivalent to exchanging the particles, such that JADs exhibit a reflection symmetry with respect to the $(\theta_1 = \theta_2)$-line.

Note, that JADs as defined in Refs. [71,73] included an energy integral, as is appropriate for studying one- or two-photon DI. In the non-perturbative regime, where neither N-photon cross sections nor triply differential cross sections are meaningful, direct evaluation of the full probability density $P(E_1, E_2, \Omega_1, \Omega_2)$ is more adequate.

Finally we introduce a measure for angular correlation by a principal component analysis: Sampling the JAD $P_{E_1,E_2}(\theta_1, \theta_2)$ for fixed energies on $\mathcal{A}$ by $\mathcal{A}$ angular grid points we obtain a matrix and can compute its singular values $\{s_\alpha\}_{\alpha=1\ldots\mathcal{A}}$. In analogy to the definition for wavepacket correlation in Ref. [156], after normalizing to $\sum_\alpha s_\alpha = 1$ we define the degree of correlation C as

$$C := \Big(\sum_{\alpha=1}^{\mathcal{A}} s_\alpha^2\Big)^{-1}. \tag{6.7}$$

It is a measure of how much information is stored in the angular distribution, and it is independent of $\mathcal{A}$ for sufficiently dense sampling (we used $\mathcal{A} = 64$). As a principal

component analysis it is an expansion into independent products. If many terms effectively contribute, a lot of information is stored in the distribution, and C is large. If only one term contributes, as for example will be seen in Fig. 6.5 (right), then $C \approx 1$. We would like to point out that this measure of correlation is readily applicable to experimental data. In this way the discussion whether processes occur with strong or little correlation can be put to a direct experimental test, independent of the analysis presented here.

6.3 Double ionization at XUV wavelengths

We first present results at short wavelengths. The goal of this section is to validate both the method and the code by comparing to results of previous publications and by reproducing simple theoretical expectations.

Our method requires the numerical solution of the full two-electron TDSE on domain B, Eq. (3.2), and ionic TDSEs on S, Eq. (2.55), see Sec. 2.2. Their convergence depend most notably on the number of partial waves included, Eq. (3.14), and on the quality of our finite element scheme, Eq. (3.17). For short wavelengths, the demand on those discretization parameters is moderate and a multitude of publications with numerical solutions of the TDSE exist. All results presented in this section are converged below 1% with respect to these parameters, in particular the achieved Helium groundstate was always below -2.902 a.u., which is in good agreement with the exact ground state energy $E_0 = -2.9037$ a.u.. In the next section, which will be devoted to IR wavelengths, we will demonstrate explicitly how convergence of the sensitive observable JAD was achieved with respect to the discretization parameters.

The tSurff method introduces additional convergence parameters, most importantly the radius where spectral information is accumulated (tSurff radius R_c) and beyond which all Coulomb interactions are neglected. As already indicated in sections 2.1.4 and 2.2.5 the complete neglection of the Coulomb interactions is not an intrinsic requirement of the method. In its current form the Coulomb potentials are truncated explicitly, equation (2.19), and we always take the box size R_c coinciding with the end point of the truncation interval $[a, R_c]$. In this section the truncation interval was taken with a width of 4 a.u. and only R_c was varied. Additionally, there is the end of time propagation T, equation (2.45), which was always chosen ≥ 8 fs after the end of the pulse, (which was mainly necessary to remove artifacts of Rydberg states reaching into the tSurff radius R_c, see Sec. 2.2.5). This leaves R_c as the only parameter with respect to which we demonstrate convergence of the short wavelength computations explicitly.

6.3.1 Single-photon double ionization

Exposing Helium to a laser field with photon energies larger than the DI threshold energy of $E_{\mathrm{GS}} \approx 2.9$ a.u. leads to single-photon DI due to electron correlation effects. The total cross section $\sigma_{N=1}$, Eq. (6.3), for this process was computed numerically [53, 71] and measured experimentally [157] as a function of the photon energy. In Fig. 6.1 we compare results

obtained with different surface radii R_c. It can be seen that reasonable agreement is already achieved with a box size of only 15 a.u.. Convergence was achieved with a square l_1-l_2-grid for each m, see Sec. 3.1.2.1, with $l_{\max} = 5$ for $m = 0$ and $l_{\max} = 3$ for $0 < m \leq m_{\max} = 3$. The radial discretization employed finite elements of width 5 a.u. and order 14.

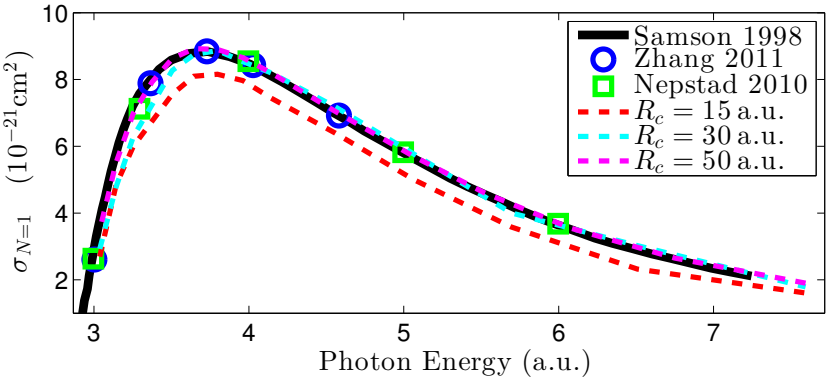

Figure 6.1: Total single-photon DI cross section of Helium as a function of the photon energy for different R_c, compared with previous numerical computations from Nepstad [53] and Zhang [71], and experimental measurements from Samson [157]. For the pulse, Eq. (8.26), we used $n = 80$ cycles and peak intensity $I = 10^{14}\,\mathrm{W/cm^2}$.

6.3.2 Two-photon double ionization cross section

For photon energies $\hbar\omega$ larger than half the DI threshold (1.45 a.u.) two-photon DI is dominant. At photon energies below the second ionization threshold $\hbar\omega < 2$ a.u. DI necessarily involves electron correlations. In this regime full agreement among the numerous theoretical approaches [27, 53, 74, 141, 152, 153, 158–164] has not yet been achieved, not even for the fully integrated total two-photon DI cross section $\sigma_{N=2}$, Eq. (6.3).

Fig. 6.2 shows a selection of recent results where approximate agreement emerges. In Ref. [158] the time-dependent full configuration interaction method was applied using pulses with a bandwidth of ≈ 0.15 a.u.. The authors attribute the large deviation from most other calculations to their method of extracting DI spectra as well as to the large spectral width of their pulse. Far from threshold there is good agreement among Refs. [27, 53, 74, 163, 164] and with our calculations for $R_c \geq 30$ a.u., but already at $R_c = 20$ a.u. we obtain qualitatively correct results.

The divergence of the results in Refs. [27, 74, 152, 158] is largest near the threshold $\hbar\omega \lesssim 2$ a.u., where the numerical distinction between low energy sequential processes and correlated double emission becomes blurred. Clearly, in this regime results also depend on the spectral width of the pulse. At $R_c = 80$ a.u. we estimate our convergence error to be $\lesssim 5\%$ and find agreement with Refs. [27, 74]. Note that the longest pulse duration of Ref. [74] is 3 fs rather than the 4 fs of Ref. [27]. We verified that the larger spectral width

changes the ratio by less than 3% for the data point $\hbar\omega = 53\,\mathrm{eV} = 1.95\,\mathrm{a.u.}$, which is the value closest to threshold in Ref. [74].

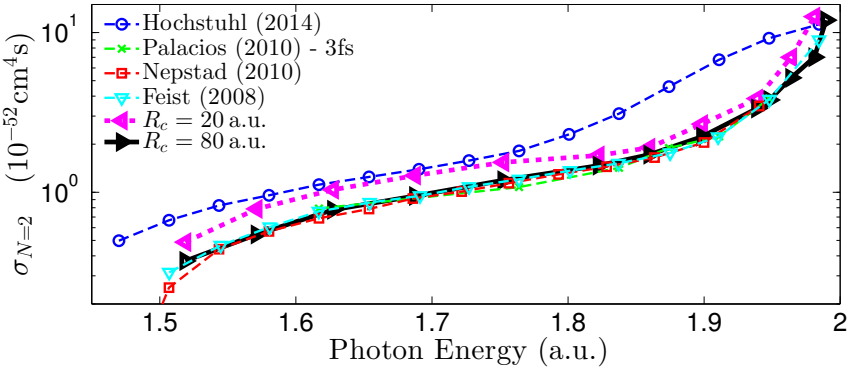

Figure 6.2: Total two-photon DI cross section as a function of the photon energy. The pulse duration of 4 fs and the peak intensity $I = 10^{12}\,\mathrm{W/cm^2}$ are chosen as in Ref. [27]. Results with $R_c = 80$ (solid black line) agree with those from Feist [27], Palacios [74] and Nepstad [53] (dashed lines). Results from Hochstuhl [158] differ, see text for explanation. Already with $R_c = 20$ (dotted magenta line) good qualitative agreement is reached.

6.3.3 Energy probability distribution

Inspecting the angle-integrated energy probability distributions $P(E_1, E_2)$ one sees pronounced two-electron multi-photon lines (see Fig. 6.3) where the electrons share the total energy $E_1 + E_2 = E_0 + N \cdot \hbar\omega$, $N = 2, 3 \ldots$, of N absorbed photons. The two-photon cross section σ_2 is the integral over the $N = 2$ shared energy line. Along the $N \geq 3$ shared energy lines local maxima are found, signatures of sequential, uncorrelated double emission. This is the case if one electron overcomes the first ionization potential $I_p^{(1)} \approx 0.9\,\mathrm{a.u.}$ ending up with energy $E_1 = -I_p^{(1)} + n\hbar\omega$, $n = 1, 2 \ldots$, and in a separate step the second electron gets detached from the ion by the absorption of two or more photons with final energy $E_2 = -I_p^{(2)} + m\hbar\omega$, $m = 2, 3 \ldots$. This process was dubbed "double ionization above threshold ionization" (DI-ATI) [165]. Other local maxima along the shared energy lines involve intermediate excited ionic states, see Sec. 6.3.5.

All these features can be seen in the energy probability distribution, shown in Fig. 6.3 for the photon energy $\hbar\omega = 42\,\mathrm{eV} \approx 1.54\,\mathrm{a.u.}$: the $N = 2$ shared energy line at $E_1 + E_2 \approx 0.2\,\mathrm{a.u.}$ does not have particular structure, while the $N = 3$ line at $E_1 + E_2 \approx 1.7\,\mathrm{a.u.}$ exhibits pronounced sequential peaks at $(E_1, E_2) \approx (0.6, 1.1)\,\mathrm{a.u.}$ and $(1.1, 0.6)\,\mathrm{a.u.}$ and similar at $N = 4$.

Fig. 6.3 also demonstrates the effect of the pulse envelope by replacing the $\cos^2$ envelope (8.27) by a $\cos^8$ one (8.28) with the same full width at half maximum. The $\cos^2$-envelope produces extra DI structures that can hardly be considered as physical. Such artifacts were already observed in Ref. [165], but their origin was not linked to

envelope effects. Both computations in Fig. 6.3 used $R_c = 20\,\text{a.u.}$ and $T = 1\,\text{ps}$. By the long time propagation any artifacts from Rydberg states are safely suppressed, see Sec. 2.2.5.

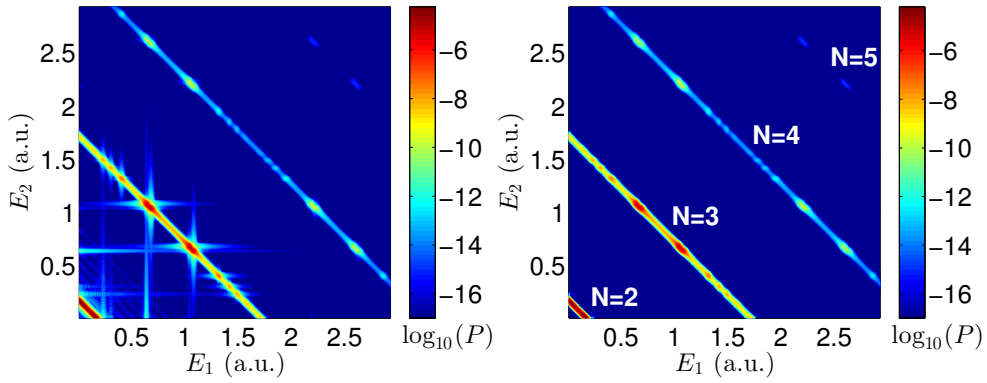

Figure 6.3: Left: Energy probability distribution $P(E_1, E_2)$ for an $n = 120$ cycle pulse with photon energy $\hbar\omega = 42\,\text{eV}$ and peak intensity $I = 10^{13}\,\text{W/cm}^2$ with a $\cos^2$ pulse envelope. Right: Calculation with a $\cos^8$ envelope of same full width at half maximum. Structures generated by the spectral sidebands of the $\cos^2$ pulse envelope disappear.

6.3.4 Angular distributions

The TDCS, Eq. (6.4), was calculated for $N = 2$ at $E_1 = 0.092\,\text{a.u.} = 2.5\,\text{eV}$ where contributions of equal energy sharing $E_1 \approx E_2$ dominate. The TDCS, as most angle and energy resolved quantities, is rather sensitive to R_c as it is strongly affected by postcollision interactions [75]. In Fig. 6.4 it can be seen that for equal energy sharing, even with a box size of $R_c = 80\,\text{a.u.}$, there remain minor quantitative discrepancies with Ref. [27]. The zero in the cross section for side-by-side emission ($\theta_1 = \theta_2$) is reproduced if electron-electron repulsion can act also far from the nucleus. One can directly see that electron repulsion rather than total box size is responsible, by performing computations with $R_c = 80\,\text{a.u.}$ but suppressing electron-electron for all $r_1, r_2 > 30\,\text{a.u.}$, which reproduces the $R_c = 30\,\text{a.u.}$ results.

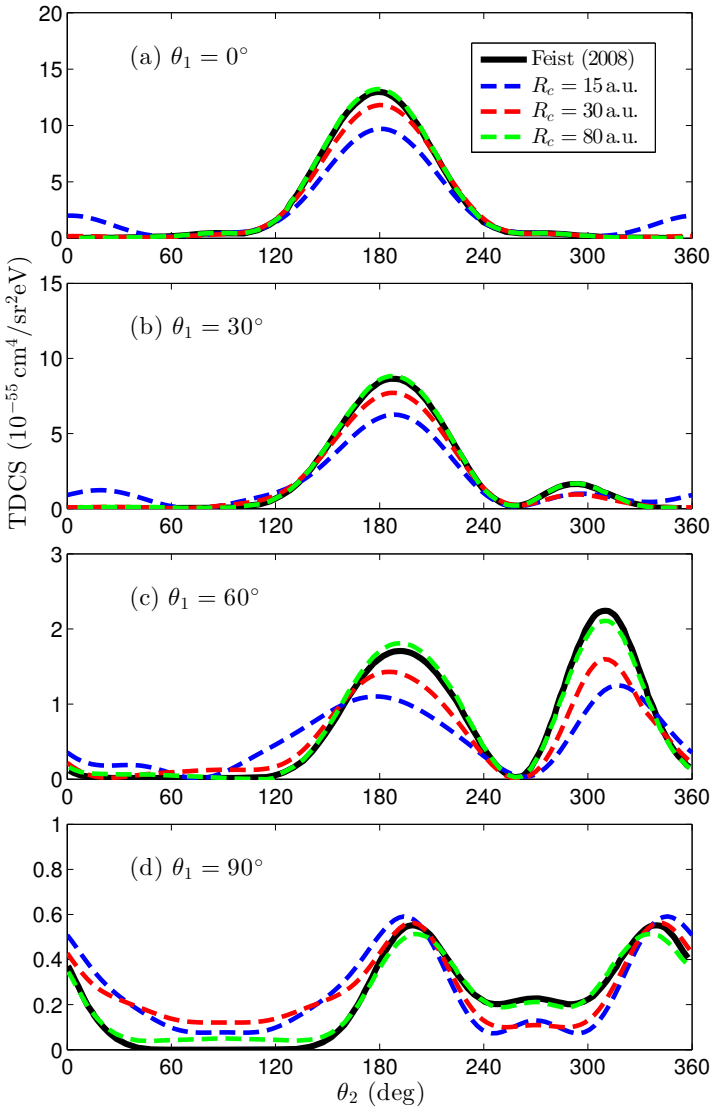

Figure 6.4: Triply differential cross section for two photon DI of He at photon energy $\hbar\omega = 42\,\mathrm{eV}$ and equal energy sharing for different tSurff radii R_c. For direct comparison, the same pulse parameters as in Feist [27] were used.

The coplanar JADs (6.6) provide a two-dimensional differential view on the cross sections (6.4), which reveals a pronounced energy dependence of the emission patterns. In Fig. 6.5 two exemplary JADs are shown. At the equal energy sharing point $(E_1, E_2) \approx (0.86, 0.86)\,\mathrm{a.u.}$ for three absorbed photons, we observe side-by-side $\theta_1 \approx \theta_2$ emission, see Fig. 6.5(a). Back-to-back emission is suppressed due to selection rule C stated in Ref. [166]: As the three-photon photo-electron states are odd, they have a node at $\vec{k}_1 = -\vec{k}_2$.

To contrast this, we picked as a second point the sequentially accessible energies $(E_1, E_2) \approx (1.09, 0.64)$ a.u., Fig. 6.5(b), where emission is almost completely uncorrelated (see also next section) and well described by the simple angular distribution $P(\theta_1, \theta_2) \sim \left|Y_2^0(\theta_1)Y_1^0(\theta_2)\right|^2$. Qualitatively these structures are already reproduced with box sizes as small as $R_c = 15$ a.u..

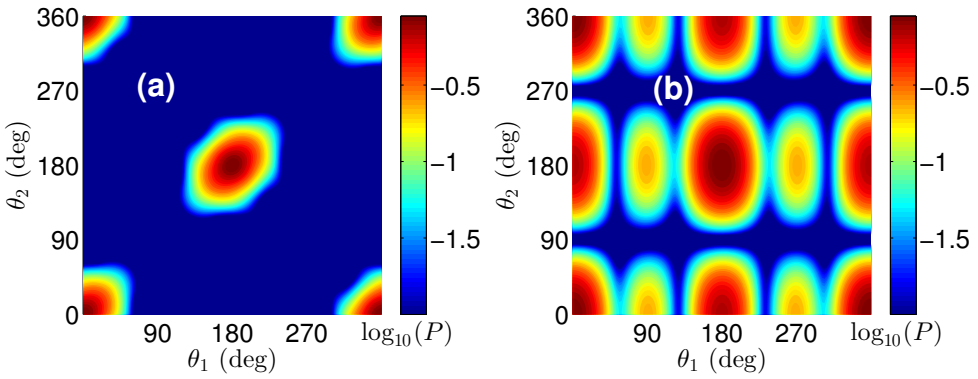

Figure 6.5: Left: Correlated side-by-side emission at three photon equal energy sharing with $\hbar\omega = 42$ eV. Right: Uncorrelated three photon sequential ionization at $(E_1, E_2) \approx (1.09, 0.64)$ a.u. at same $\hbar\omega$. Plots are normalized to $\max_{E_1,E_2}[P(E_1, E_2)] = 1$.

DI processes involving a different number of absorbed photons or different energy sharings may exhibit other angular distributions. We showed two-photon equal energy sharing, which is dominated by back-to-back emission, see Fig. 6.4(a). At three photon equal energy sharing back-to-back emission is suppressed, and we observe side-by-side emission. In single-photon DI (only possible for higher photon energies) at equal energy sharing, selection rules B2 and F in Ref. [166] exclude both back-to-back and side-by-side, as well as conic emission (where $\theta_2 = \pi - \theta_1$), and the resulting JAD is dominated by four peaks that correspond to symmetric emission (where $\theta_2 = -\theta_1$) [73], see Fig. 6.6(a). At the same photon energy, the sequential channel for two-photon DI is open, and the angular distribution at the sequential peak is again almost completely uncorrelated and well described by $P(\theta_1, \theta_2) \sim \left|Y_1^0(\theta_1)Y_1^0(\theta_2)\right|^2$, Fig. 6.6(b).

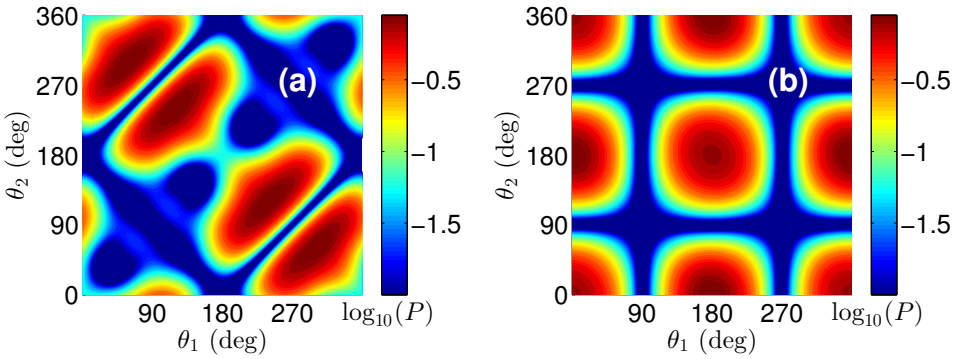

Figure 6.6: Left: Correlated symmetric double emission at equal energy sharing of a single $\hbar\omega = 124\,\mathrm{eV}$ photon. Right: Uncorrelated two-photon sequential ionization at same $\hbar\omega$. Plots are normalized to $\max_{E_1,E_2}[P(E_1,E_2)] = 1$.

6.3.5 Angular correlations

We already classified, by visual inspection, the angular distributions shown in Figs. 6.5 and 6.6 as correlated or uncorrelated. For a more quantitative description we use the correlation measure defined in Eq. (6.7).

In Fig. 6.7(a) we show the probability distribution evaluated along the $N = 3$ photon shared energy line of Fig. 6.3. The JADs in Fig. 6.5 correspond to the points $\Delta E := E_1 - E_2 = 0$ and $\Delta E \approx 0.45\,\mathrm{a.u.}$. Apart from the purely sequential peaks at $(E_1, E_2) = (-I_p^{(1)} + \hbar\omega, -I_p^{(2)} + 2\hbar\omega)$, there are several more peaks corresponding to excited states of the He^+ ion. Denoting by $\mathcal{E}_n$ the excitation energy from the ionic ground state to the n-th excited state, the DI efficiency is enhanced at energies $(E_1, E_2) = (-I_p^{(1)} + 2\hbar\omega - \mathcal{E}_n, -I_p^{(2)} + \hbar\omega + \mathcal{E}_n)$ with $n \in \mathbb{N}$, also see Ref. [70]. As the photon energy $\hbar\omega \approx 1.54\,\mathrm{a.u.}$ is nearly resonant with the first excitation energy $\mathcal{E}_1 = 1.5\,\mathrm{a.u.}$, the peak involving this transition and the pure sequential peak are barely discernible.

The degree of correlation along the three photon shared energy line features a minimum for each maximum of the DI probability. As expected, correlation is reduced when the transition goes through an intermediate state that disentangles the detachment of the two electrons. In particular the value for no correlation $C = 1$ is almost reached at the sequential point $\Delta E = 0.45$, where the angular distribution is well described as $\propto |Y_2^0 Y_1^0|^2$, Fig. 6.5(b).

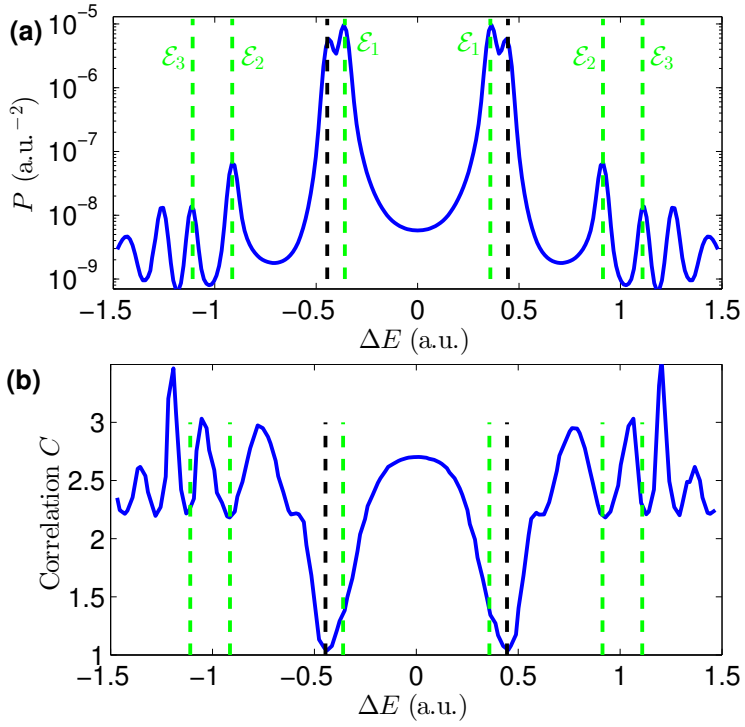

Figure 6.7: Top: Probability distribution $P(E_1, E_2)$ shown in Fig. 6.3 along the $N = 3$ photon line as a function of the energy difference $\Delta E := E_1 - E_2$. Bottom: Angular correlation C, Eq. (6.7), along the same line. Dashed lines: Sequential peaks involving the ionic ground state (black), and excited ionic states (green). The minima for higher ionic excitations are slightly displaced due to the cutoff of the Coulomb potential at $R_c = 20$ a.u..

6.4 Double ionization at infrared wavelengths

6.4.1 Two-color XUV-IR double emission

To the best of our knowledge, the only published results of *ab initio* computations for DI photo-electron *spectra* at IR wavelengths treat situations, where an XUV pulse initiates dynamics and a weak IR pulse controls the ionization of the excited system. For example, in Ref. [73] an IR pulse with intensity $3 \times 10^{12}\,\mathrm{W/cm^2}$ was used to modify the angular distributions of single- and two-photon DI by the XUV pulse. In Ref. [28] time-dependent ionization yields at large intensities were computed, but the used method did not allow for computation of DI spectra.

In Ref. [31] an attosecond XUV pulse with photon energy $\hbar\omega = 1.5\,\mathrm{a.u.}$ tuned to the lowest He^+ transition energy was used to enhance photo-absorption from a single cycle IR dressing pulse of moderate intensity $2 \times 10^{14}\,\mathrm{W/cm^2}$. A strong increase in DI efficiency was found at time delays between IR field and XUV pulse coinciding with recollision events, which was ascribed to excessive absorption of IR photons induced by the strong electron-electron correlation.

Fig. 6.8 shows our results for the probability density of total emission energy $E_{\mathrm{tot}} = E_1 + E_2$

$$P(E_{\mathrm{tot}}) = \int_0^{E_{\mathrm{tot}}} \mathrm{d}E_1\, P(E_1, E_{\mathrm{tot}} - E_1). \tag{6.8}$$

The upper panel shows the enhancement across the whole energy range. The lower panel singles out $E_{\mathrm{tot}} = 60\,\mathrm{eV}$ as a function of delay time. We reproduce the overall picture reported in Ref. [31], but find significant quantitative discrepancies. Note that the comparison is not in absolute numbers, as results of Ref. [31] are given in arbitrary units. For example, at larger positive offsets Ref. [31] shows nearly constant data points for large positive offsets, which does not match with our computations. Such a behavior may appear implausible, as at these delays the IR has nearly passed when the XUV arrives, and yields should fall to the very low level of pure XUV double ionization at $E_1 + E_2 = 60\,\mathrm{eV}$. We would like to remark that the simulation box size of 305 a.u. used in Ref. [31] falls short of the distance of $\gtrsim 400\,\mathrm{a.u.}$ that 60 eV electrons travel during the IR pulse duration. For tSurff, the cutoffs at $R_c \leq 25\,\mathrm{a.u.}$ used in our simulations would mask long range Coulomb and post-collision effects, however the impact of R_c appears to be small, see Fig. 6.8.

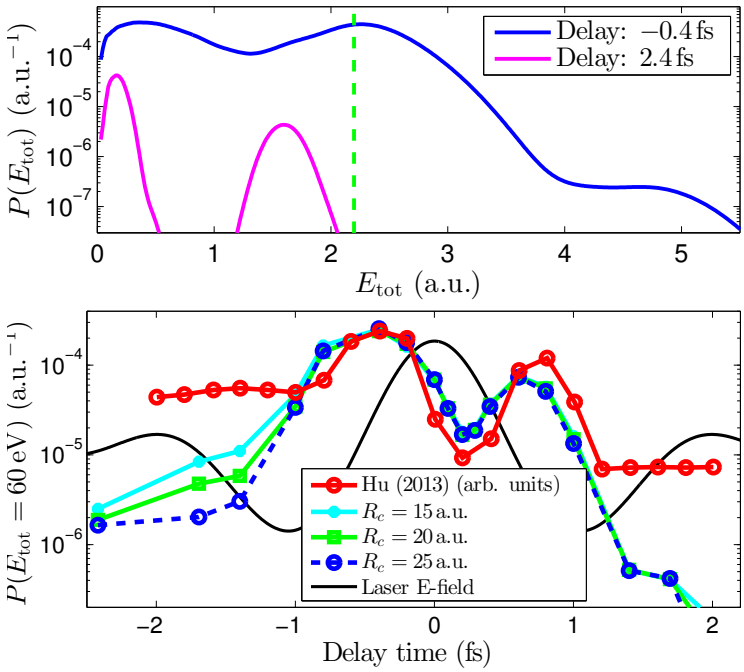

Figure 6.8: Top: Photo-electron spectrum as a function of the shared total energy, Eq. (6.8), for two relative time delays between XUV and IR pulses. Large positive time delays correspond to the XUV pulse coming after the IR pulse. Green dashed line indicates $E_{\rm tot} = 60\,{\rm eV}$. Bottom: $P(E_{\rm tot} = 60\,{\rm eV})$ as a function of the relative time delay: Dependence on R_c and comparison with Hu [31]. Arbitrary units in Ref. [31] are adjusted to approximately match our results.

6.4.2 Double ionization enhancement by recollision

The full fragmentation of Helium by an IR laser pulse *alone* is only fully understood for very high laser intensities $\gtrsim 5 \times 10^{15}\,{\rm W/cm^2}$, where the description by two independent and sequential tunnel ionization events agrees with experiment [47]. At lower intensities, predictions by such a sequential model are wrong by several orders of magnitude. It has been widely accepted that in this case field induced recollisions lead to some form of non-sequential double ionization (NSDI) [59]. Several such NSDI pathways have been proposed, including simultaneous ejection (SE) and recollision induced excitation with subsequent ionization (RESI) [50, 51]. For kinetic energies of the recolliding electron below the ionic excitation threshold $\mathcal{E}_1 = 1.5\,{\rm a.u.}$, which is the case for intensities below $\approx 2.3\times10^{14}\,{\rm W/cm^2}$ at 780 nm, these pathways are closed and a mechanism called doubly delayed ejection (DDE) [52] seems to dominate.

To this date, these DI processes have not been reproduced by solutions of the two-electron TDSE for the full intensity range because of the high demand on computational resources, see Sec. 2.2.1. Using tSurff, we can provide yields up to intensities $4\times10^{14}\,{\rm W/cm^2}$, with error estimates of $\lesssim 20\%$ up $3.5 \times 10^{14}\,{\rm W/cm^2}$, using only moderate computational

resources.

The ratio of double to single ionization yields is shown in Fig. 6.9 for R_c up to 30 a.u. and compared to experiment. Except for R_c, our results are converged with respect to all other discretization parameters to within a few percent. We used a laser pulse with single cycle rampup, n cycles at full intensity and one cycle rampdown at wavelength $\lambda = c\tau = 780\,\mathrm{nm}$:

$$A(t) \propto f_{\alpha,\beta}(-t)\sin\left(2\pi t/\tau\right) f_{\alpha,\beta}(t). \tag{6.9}$$

with $\alpha = n\tau/2$, $\beta = (n/2+1)\tau$ and $f_{\alpha,\beta}$ as in Eq. (2.20). The calculations were performed with pulse durations of $n = 4$ cycles.

Fig. 6.9 shows the double-to-single ratio as obtained with $R_c = 15, 20, 25$ and 30 a.u. and smooth potential truncation $R_c - a = 3, 4, 6$ and 8 a.u., respectively, see Eq. (2.19). One can clearly see larger intensities require larger R_c, which roughly correlates with the quiver radius r_q. In the intensity range 1.6 to $3 \times 10^{14}\,\mathrm{W/cm^2}$ with quiver radii $r_q = 20 - 27$ a.u. results vary by at most 25% between $R_c = 20$ and $R_c = 30$. At the intensities $I \geq 3.5 \times 10^{14}\,\mathrm{W/cm^2}$, numerical results for $R_c < 30$ strongly depart from our largest calculation with $R_c = 30$. The lower intensity limit for our calculations is $\sim 1.5 \times 10^{14}\,\mathrm{W/cm^2}$, where the overall yields are so small that numerical inaccuracies render the results useless.

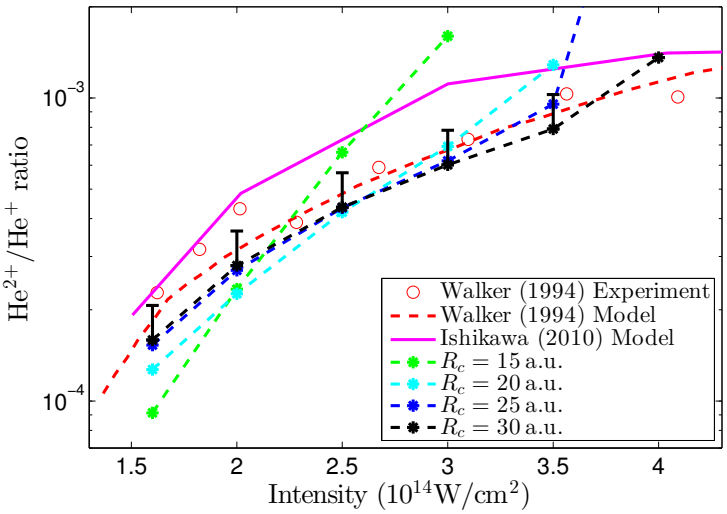

Figure 6.9: Ratio of DI yield and single ionization yield as a function of intensity. Experiment and model from Walker [47], model calculations from Ishikawa [59], and our full two-electron results for increasing R_c. Upward error bars indicate the long pulse limit.

There is some dependence of our results on the pulse duration: Using a two-cycle ramp up we found changes of less than 5% at selected intensities. More important is the dependence on pulse duration. At the intensities $\leq 2.5 \times 10^{14}\,\mathrm{W/cm^2}$ we found an increase of ratio for $n = 4, 5, \ldots$ cycles which saturates at about 30% for $n \approx 8$ with no relevant increase for durations up $n = 12$. We expect similar pulse duration dependence at higher

intensities. This increase by 30% is indicated by an (upward) error bar for our $R_c = 30$ calculation in Fig. 6.9.

Also shown are the experimental results and model predictions of Ref. [47]. There is good agreement with the experimental data, but that may well by fortuitous, as experimental intensities were subjected to errors as large as 30%. The analytical model of Ref. [47] is based on the single active electron approximation (SAE) and on the ac-tunneling (ADK) rates [36] and is, by its construction, close to the experimental data. The model in Ref. [59] implements the rescattering scenario using the SAE approximation in combination with electron-ion impact cross sections. It appears to somewhat overestimate the actual ratio, as it remains outside the estimate for pulse length error in our tSurff computations. Note that in the plot shown in Fig. 1 of Ref. [59], experimental intensities are scaled by a factor 1.15 for the purpose of the comparison.

6.4.3 Energy probability distributions

In Fig. 6.10 we present energy probability distributions $P(E_1, E_2)$ for IR double ionization at intensities $I = 1.6, 2.5, 3.5$ and 4 W/cm^2, with the pulse shape as in Fig. 6.9 for photoelectron energies $E_1, E_2 < 3\,U_p$. One sees that the 4-cycle pulses define the carrier frequency ω well enough to clearly distinguish individual DI-ATI peaks separated by the photon energy $\hbar\omega$. The lines of shared energy are positioned at $E_1 + E_2 = E_0 - 2\,U_p + N \cdot \hbar\omega$. The increase of the ionization potential by one U_p per electron represents the Stark shift of the continuum [167], which was negligible in the short wavelength regime $U_p \approx 0$, see Sec. 6.3.3. The exact positions of the DI-ATI peaks on the shared energy lines could not be explained analogously. One also observes overall changes in the DI emission pattern with increasing intensity I. In Fig. 6.10(a) and (b) conspicuous enhancement of double emission in the area $E_1 \approx E_2 \approx 1.7\,U_p$ appears. Note that at the corresponding intensities 1.6 and 2.5 W/cm^2 the maximal recollision energy remains below the second ionization potential of 2 a.u.. As recollision cannot be the sole DI mechanism, one may speculate that processes like simultaneous tunneling and doubly delayed emission (DDE) [52] where final energies E_1 and E_2 are comparable play a greater relative role. At (c) and (d) direct excitation by the recolliding electron becomes accessible and a roughly L-shape energy distribution emerges.

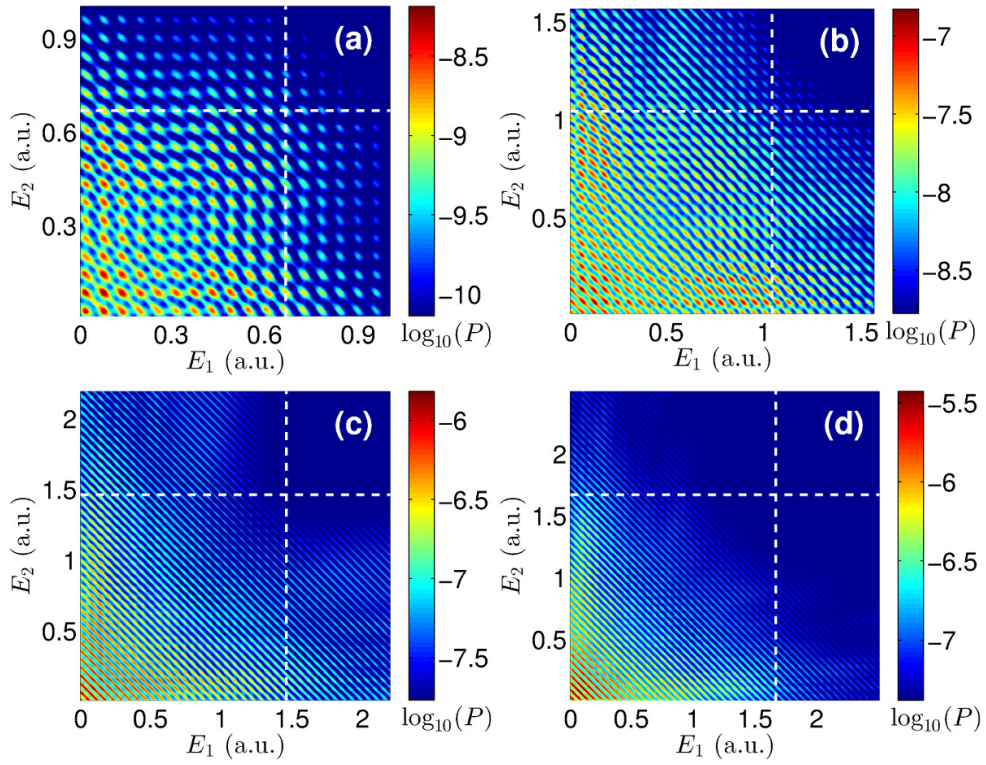

Figure 6.10: Total DI spectra $P(E_1, E_2)$, Eq. (6.5), for several of the data points with truncation interval $R_c = 30$ a.u. shown in Fig. 6.9. Intensities in units of 10^{14} W/cm^2 are (a) 1.6, (b) 2.5, (c) 3.5 and (d) 4.0. White dashed lines mark $2\,U_p$.

For estimating the R_c-induced errors of the energy distributions we define the relative difference $\mathcal{E}$ between two distribution P_a and P_b as

$$\mathcal{E}(E_1, E_2) := \frac{|P_a(E_1, E_2) - P_b(E_1, E_2)|}{\overline{P}_{\hbar\omega}(E_1, E_2)}, \tag{6.10}$$

where $\overline{P}_{\hbar\omega}(E_1, E_2) := \max_{E_1', E_2'} P(E_1', E_2')$ denotes the maximum over a $\hbar\omega$-neighborhood with $(E_1' - E_1)^2 + (E_2' - E_2)^2 < (\hbar\omega)^2$.

Two examples are shown in Fig. 6.11. At $I = 2 \times 10^{14}$ W/cm^2 with quiver radius $r_q = 22$ a.u. we compare calculations with $R_c = 25$ a.u. and $R_c = 35$ a.u., Fig. 6.11(a). Relative differences approach 60% where one electron has low energy and also near the energy diagonal. These regions can be expected to be strongly affected by Coulomb truncation. In many areas differences remain below 20%. The intensity $I = 3.5 \times 10^{14}$ W/cm^2 is near the limit of our presently accessible parameter range, Fig. 6.11(b). At this intensity the quiver radius $r_q = 29$ a.u. exceeds the truncation radius $R_c = 25$. Still, comparing to $R_c = 30$ a.u., relative differences approach 60% only at few places in the relevant region $E_1 + E_2 \leq 2\,U_p$, and are mostly below 30%. Large relative differences naturally appear where yields become small.

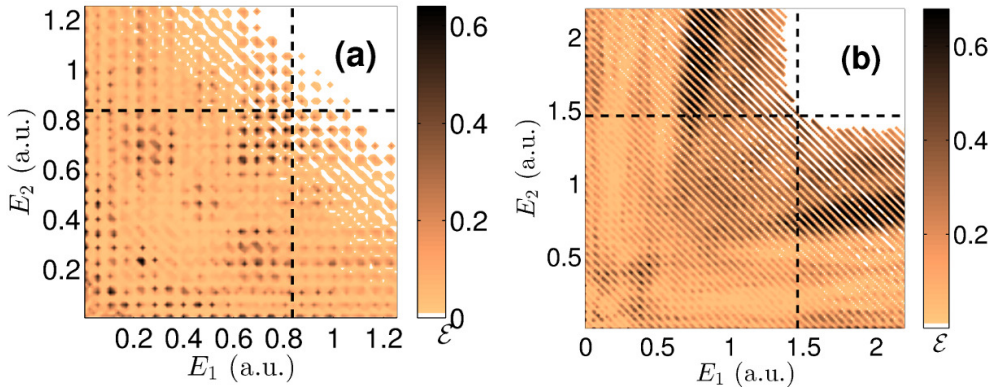

Figure 6.11: Error estimates $\mathcal{E}$ by comparing computations with (a) radii $R_c = 25\,\text{a.u.}$ vs. $R_c = 35\,\text{a.u.}$ for $I = 2 \times 10^{14}\,\text{W/cm}^2$, and (b) $R_c = 25\,\text{a.u.}$ vs. $R_c = 30\,\text{a.u.}$ for $I = 3.5 \times 10^{14}\,\text{W/cm}^2$. Errors are only plotted where $P(E_1, E_2)$ is larger than 1% of its maximum.

In Ref. [29], a sharp transition of the cutoff in the shared DI energy distribution from $5.3\,U_p$ to $>7\,U_p$ was found, when maximum recollision energies surpass $I_p^{(2)} = 2\,\text{a.u.}$ at $\lambda = 390\,\text{nm}$. A similar cutoff was reported in Ref. [168] for a one-dimensional model. We could reproduce this for 390 nm (not shown) and find the cutoff also in full three dimensions at 780 nm, see Fig. 6.12.

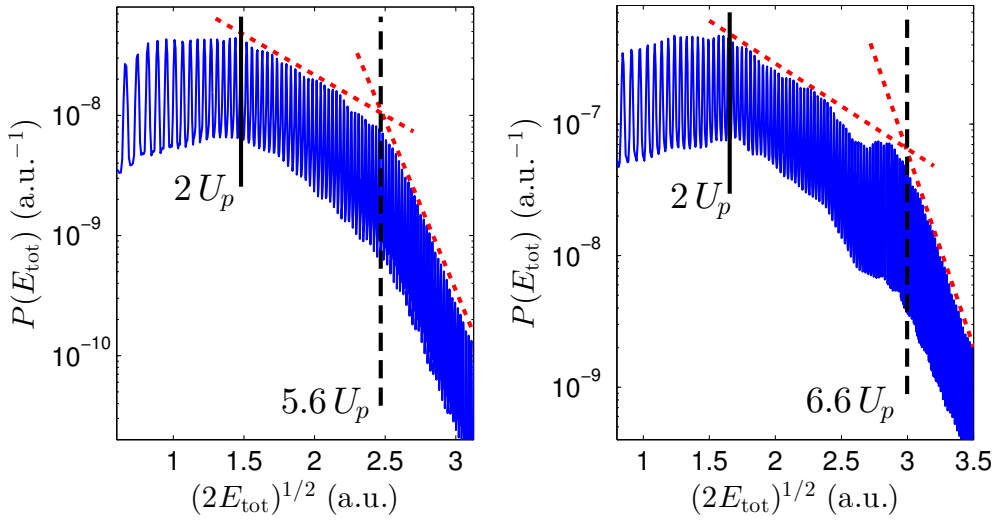

Figure 6.12: Total momentum spectrum $P(E_{\rm tot})$, Eq. (6.8), for a 780 nm $n = 4$ cycle pulse. Left: 2.6×10^{14} W/cm^2 cutoff at $5.6\,U_p$. Right: 3.25×10^{14} W/cm^2 cutoff at $6.6\,U_p$. Solid lines mark the momentum corresponding to $2\,U_p$, dashed lines mark the transition to the exponential decay at the cutoff of the spectrum, dotted lines indicate the slopes. The behavior conforms with Fig. 3 of Ref. [29] for 390 nm at the corresponding intensities 1.04×10^{15} W/cm^2 and 1.3×10^{15} W/cm^2.

The appearance of the cutoff at $5.3\,U_p$ is attributed to the maximum Coulomb repulsion energy between continuum states along the laser polarization direction in Ref. [168]. For laser intensities below the threshold of recollision induced excitation of the ion, they suggest recollision induced double excitation, i.e. a recombination process into a doubly excited state which would definitely qualify for a doubly delayed emission (DDE) process. In future works this hypothesis could in principle be tested by monitoring the population of certain doubly excited states over time.

6.4.4 Angular distribution

JADs depend most sensitively on R_c and full convergence could not be achieved with moderate computational effort. In Fig. 6.13 we show JADs for three different (E_1, E_2) at $I = 2 \times 10^{14}$ W/cm^2. In (b) it can be seen that if both electrons escape with large energies the angular emission pattern is uncorrelated and highly focused around the polarization axis. If one electron barely manages to escape, then its angular distribution is less focused and the JADs exhibit complex structures, see (c). Correspondingly, if both electrons leave with small energies we observe correlated angular emission patterns, an example of which can be seen in (a).

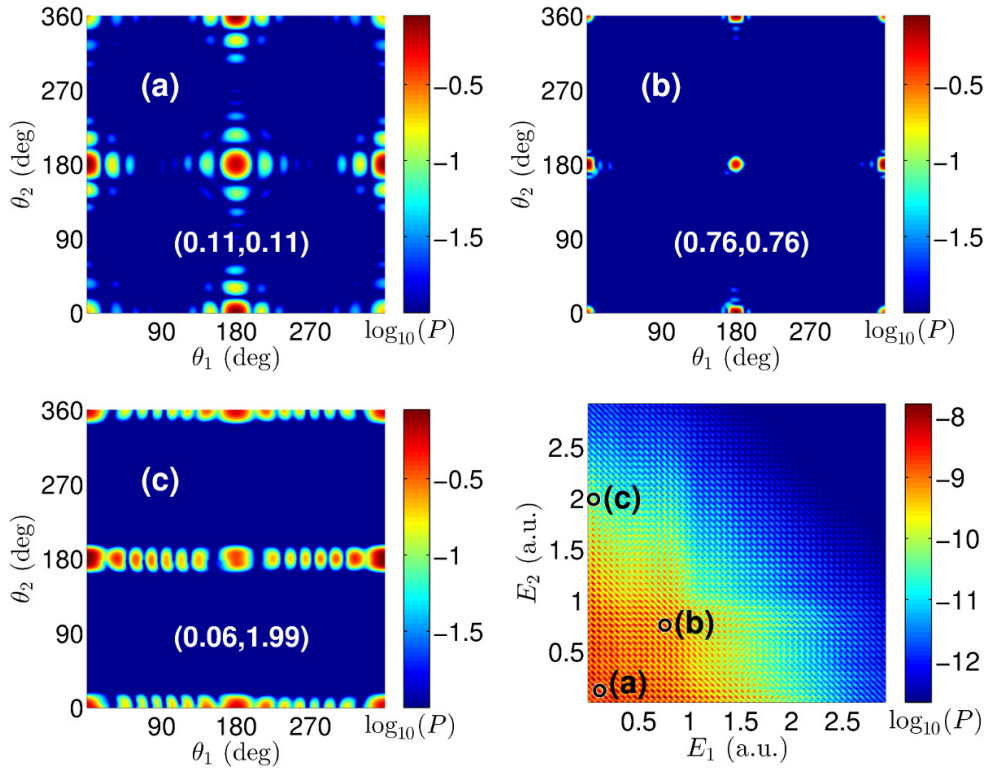

Figure 6.13: JADs for wavelength 780 nm and intensity $I = 2 \times 10^{14}\,\mathrm{W/cm^2}$. The panels (a), (b), and (c) correspond to the energies marked in the $P(E_1, E_2)$ distribution, lower right panel. Plots are normalized to $\max_{E_1,E_2}[P(E_1, E_2)] = 1$.

The JADs shown in Fig. 6.13 are accurate with respect to the angular momentum expansion to the level of $\sim 10\%$. Convergence with R_c depends on the final electron energies. In Fig. 6.14 we present cuts through JADs of Fig. 6.13 at $\theta_2 = 0$. If both energies are large, then neither the exact nuclear potential shape nor postcollision interactions are relevant, and convergence is achieved with $R_c = 30\,\mathrm{a.u.}$, Fig. 6.14(b). However, if at least one of the electrons energies is small, then electrons may interact with the nucleus over long times and convergence with R_c could only be achieved to the level of qualitative agreement. The overall distribution does not change completely but some qualitative features are still in flux. For example at the low emission energies $E_1 = E_2 = 0.11$, Fig. 6.14(a) the dominant emission direction changes from back-to-back to side-by-side when increasing $R_c = 20\,\mathrm{a.u.}$ to $R_c = 25\,\mathrm{a.u.}$. In (c) local minima appear along the polarization axis with $R_c = 30\,\mathrm{a.u.}$.

Clearly, larger R_c are required for convergence at low energies. The present implementation of the method renders such calculations impractical with reasonable computational resources. Also, while for $2 \times 10^{14}\,\mathrm{W/cm^2}$ computations with $R_c = 35\,\mathrm{a.u.}$ were still accomplishable, at higher intensities the increasing demand on angular momenta is prohibitive and only computations with up to $R_c = 30\,\mathrm{a.u.}$ were practical.

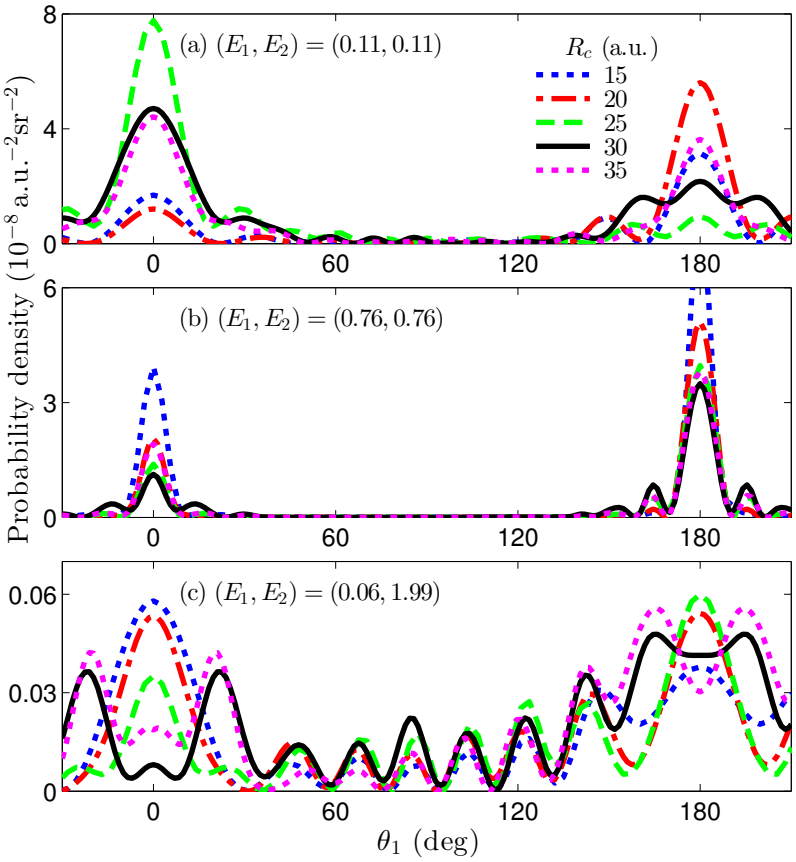

Figure 6.14: Cuts through JADs of Fig. 6.13 at $\theta_2 = 0$ for various values of R_c. At low energies convergence is only qualitative, see (a) and (c). At high energies the angular distribution stabilizes at $R_c = 30$ a.u., see (b).

Fig. 6.15 shows JAD converges with the number of partial waves at different total energies and different energy sharings. Calculations with 551, 639 and 737 partial waves are indistinguishable within the resolution of the plot almost everywhere. Convergence is only critical for side-by-side emission $\theta_1 \approx \theta_2$, where maximal differences of $\approx 20\%$ remain between the three calculations.

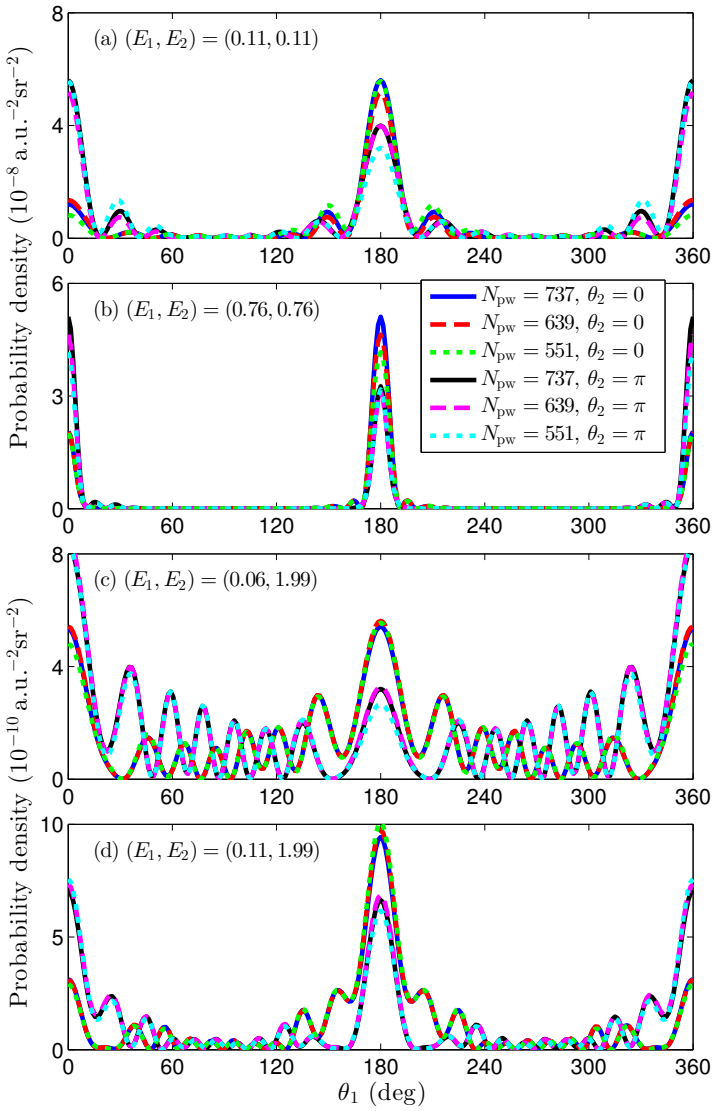

Figure 6.15: Cuts through JADs of Fig. 6.13 at $\theta_2 \in \{0, \pi\}$ for different number of partial waves $N_{\rm pw}$. The laser pulse consists of four full cycles ($n = 4$) at $\lambda = 780\,\text{nm}$ and $I = 2 \times 10^{14}\,\text{W/cm}^2$ and potentials are truncated at $R_c = 20\,\text{a.u.}$.

6.4.5 Angular correlations

As for XUV double ionization we compute the angular correlation by Eq. (6.7), and find it to follow the DI-ATI structure, although not as clearly as in Fig. 6.7). In addition, at IR wavelength we find maxima at small electron escape energies $E_{1,2} \lesssim 0.2\,\text{a.u.}$. Strong correlation at low energies is to be expected as the electrons interact over longer times before leaving the vicinity of the nucleus.

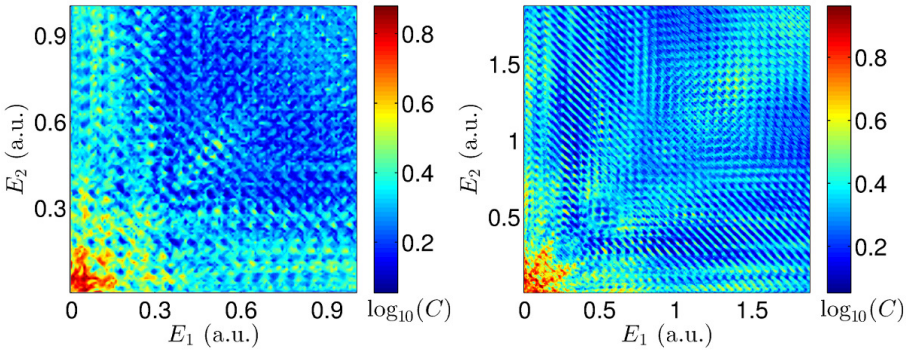

Figure 6.16: Angular correlation C as a function of photo-electron energies for intensities $1.6 \times 10^{14}\,\mathrm{W/cm^2}$ (left) and $2.0 \times 10^{14}\,\mathrm{W/cm^2}$ (right) and wavelength $\lambda = 780\,\mathrm{nm}$. Computations with $R_c = 30\,\mathrm{a.u.}$. If both photo-electrons linger close together over long times strong correlations build up.

The situation at $\lambda = 390\,\mathrm{nm}$ is similar. In Fig. 6.17 we show the energy probability distribution for intensity $5 \times 10^{14}\,\mathrm{W/cm^2}$ and the corresponding correlations.

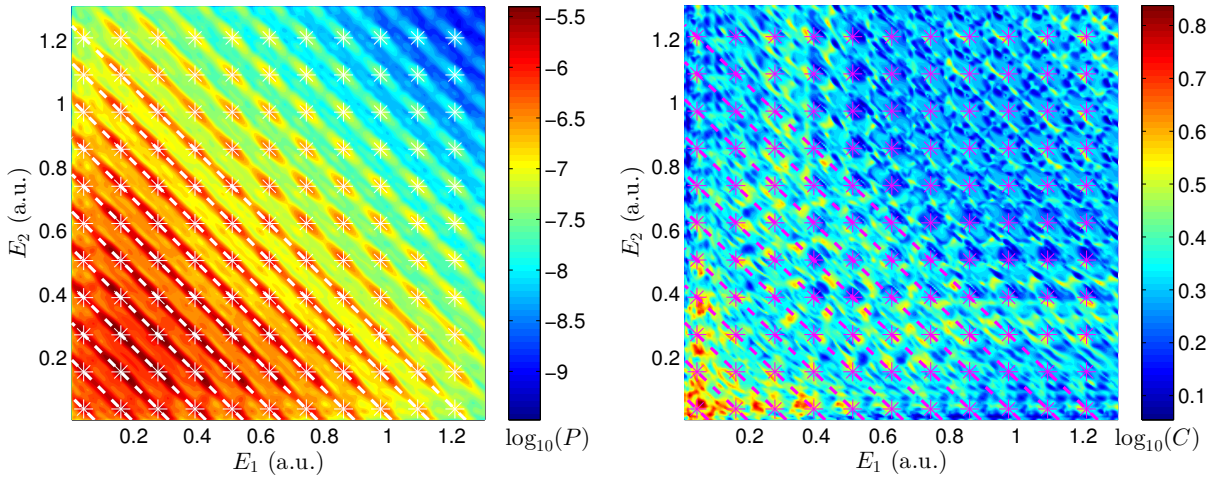

Figure 6.17: Energy probability distribution (left) and angular correlation C (right) as a function of photo-electron energies for intensity $5 \times 10^{14}\,\mathrm{W/cm^2}$ and wavelength 390 nm. Computations with $R_c = 20\,\mathrm{a.u.}$. Dashed lines indicate shared energy photon lines and stars the DI-ATI peaks. It can be seen that typically local minima in the correlation plot are found at DI-ATI peaks.

Dashed lines indicate shared energy photon lines with $E_1 + E_2 = E_0 - 2\,U_p + N \cdot \hbar\omega$. As in Sec. 6.4.3 the exact positions of the DI-ATI peaks on the shared energy lines could not be explained are only marked for better comparison of the two plots.

As in Fig. 6.7, correlation minima are achieved at maxima of the energy probability distribution, although not as clearly. This might reflect multi-photon contributions to the ionization dynamics, which are to be expected at the Keldysh parameter $\gamma \approx 1.3$ for the given parameters.

Chapter 7

Conclusion

Summary

In conclusion, we made a range of contributions to current strong field physics. This was made possible by the high numerical efficiency of the here presented methods, most importantly the time-dependent surface flux (tSurff) method for efficient computation of photo-electron spectra.

As of now, the computational effort for simulating a single particle in a strong external laser field is manageable for all but the most extreme laser parameters when employing tSurff, which allows for full parameter studies of nearly arbitrary one-electron systems. Using results of such computations as benchmark data, it was found that no tunnel delays are present in Attoclock experimental setups for the Hydrogen atom which allows for calibration of the Attoclock when studying more complicated targets. Further, adiabaticity effects on photo-electron momentum spreads were studied, but discrepancies between theory and experiment could not be explained by non-adiabatic effects.

Also the computation of single ionization spectra of two-electron systems is now possible with moderate computational resources. We showed how resonant Fano line shapes of doubly excited states in the Helium atom can be controlled by an external long wavelength streaking field. We provided a theoretical description of this two color process and determined continuum electron streaking as the main physical effect.

Finally, we are now able to compute fully differential double ionization spectra of the Helium atom and managed to reproduce for the first time the double ionization "knee" in *ab initio* computations. Full convergence with the primary control parameter, the box size, could however not be reached within reasonable computation times. Here, further improvements of the methods and the code are required.

Outlook

Algorithmic improvements

The ability to efficiently perform studies in more-electron systems is of high interest. Both the haCC approach as well as the full two-electron basis quickly reach computational limits, which can however be pushed in various ways.

As a first step there is always room for improvements in the choice of basis. In particular, fully incorporating the benefits of the FE-DVR basis [68] and thereby obviating the need of the complicated inverse overlap (Sec. 8.6) will allow for better scaling behavior in massively parallelized computations. For an efficient treatment of molecules (e.g. the H_2 molecule, Sec. 5.1.4), a multi centered basis could be used to embrace the molecular structure and thus facilitate convergence. Electron dependent radial restrictions could be employed in computations where the laser parameters enforce a large box size but only single ionization is of interest.

Several enhancements of the code may allow to further push the realm of achievable multi-electron computations. For example, the electron-electron interaction may be more efficiently implemented by exploiting its low rank structure at large distances. Concerning tSurff, the truncation (Eq. (2.19)) of the electron-electron interaction at large distances can be avoided by switching to a relative coordinate system between the two ionized electrons. It may also be possible to mitigate the effects of the core potential truncation by introducing Eikonal Volkov corrections [64] to the currently used simple plane waves.

Future applications

With increasing computational efficiency and access to ever larger computing facilities a wide range of possible applications opens up.

Attoclock experiments on Helium [34] still show discrepancies with numerical computations. Applying the two-electron code to the Attoclock setup with full treatment of both electrons in the circular polarized laser pulse may explain those discrepancies if two-electron effects are responsible. Resolving this issue might help unravel the nature of tunnel delays.

Similarly, the efficiency of double ionization in elliptically polarized IR pulses as a function of ellipticity could be studied. In Ref. [139] it was shown that recollision induced enhancement of double ionization signal does appear in some targets, but not all. Systematic two-electron studies with various atomic potentials could shed further light into the observed behavior. Computing momentum spreads (Sec. 4.2.2) in Helium fully including two-electron effects may help further understanding non-adiabaticity effects and devising more reliable and accurate laser intensity calibration techniques.

On the quest of resolving dynamics on ever shorter time scales, laser frequencies are pushed towards the extreme ultra violet. If at the same time larger structures like molecules are to be studied, numerical computations will need to include numerically demanding effects beyond the dipole approximation.

Pulses with time-dependent wavelength (chirped pulses) often appear in experiments, where the dependence of the photo-ionization processes on the chirp can be used to extract further information on ultra short time scales [169]. Systematic numerical multi-electron studies could be used for designing optimal pulse forms for extracting attosecond dynamic signatures.

Experimental techniques like light induced electron diffraction (LIED) [15] are rarely applied to single-electron systems. If the efficiency of the two-electron code and the haCC code can be increased, diffraction patterns of simple molecules like H_2 could be computed for arbitrary angles between the laser polarization axis and the molecular axis. Understanding multi-electron effects in such systems will be essential for progress with technologically more relevant targets like bio-molecules.

In pump probe experiments double ionization is studied by combining two laser pulses. Since it is experimentally very challenging to produce two synchronized attosecond XUV pulses with large intensities, variable time delay, and different mean photon energies, experiments typically realize XUV-IR pump probe setups, like in attosecond streaking [13]. A study for such a setup was presented here in order to analyze the effects of weak IR streaking fields on doubly excited states. Similar studies involving strong IR pulses or non-parallel polarization axis of XUV and IR pulses may reveal interesting phenomena.

Structural extensions

There are also several possible extensions of the code. Maybe most interestingly would be to include nuclear core motion. This would allow to include vibrational degrees of freedom or even study molecular dissociation dynamics [126] following electronic ionization or excitation by an external laser pulse.

Combining the haCC ansatz with a full two-electron basis would open the possibility to simulate double ionization in more complicated targets and may introduce corrections in the cases where the current haCC basis comes to its limits. Progressing to true multi-electron dynamics, one may also study solid surface photo-ionization effects and see if they can be modeled by a two-electron effective potential within an haCC type ansatz.

Chapter 8

Appendix

8.1 Computation of transient absorption spectra

In Sec. 5.2.4 we present transient absorption spectra (TAS) extracted from the numerical computations. The formula used is

$$\sigma_{\mathrm{TAS}}(\omega) = 8\pi\alpha\Im\big[\hat{\dot{r}}(\omega)/\hat{\mathcal{E}}(\omega)\big] \tag{8.1}$$

where $\hat{\mathcal{E}}(\omega)$ is the Fourier transform of the electric field $\mathcal{E}(t)$ and $\hat{\dot{r}}(\omega)$ is the Fourier transform of the time-dependent dipole velocity $\dot{r}(t)$. $\Im[\dots]$ denotes the imaginary part.

This expression is obtained following the derivation in Ref. [170]:

First, compute the energy absorbed by the system described by the Hamiltonian (here in velocity gauge)

$$H(t) = -\frac{\Delta}{2} + V(r) + \mathrm{i}\nabla A(t) \tag{8.2}$$

with vector potential $A(t)$. The energy difference between the time T_0 before all laser pulses and time T_1 after all laser pulses is

$$\begin{aligned}
\delta E &= \int_{T_0}^{T_1} \mathrm{d}t\, \partial_t \langle\psi(t)|H(t)|\psi(t)\rangle = \int_{T_0}^{T_1} \mathrm{d}t\, \langle\psi(t)|\partial_t H(t)|\psi(t)\rangle \\
&= \int_{T_0}^{T_1} \mathrm{d}t\, \dot{A}(t)\langle\psi(t)|\mathrm{i}\nabla|\psi(t)\rangle = \int_{-\infty}^{\infty} \mathrm{d}t\, \mathcal{E}(t)\langle\hat{p}\rangle(t)
\end{aligned} \tag{8.3}$$

where $\langle\hat{p}\rangle \equiv \dot{r}(t)$ can be extracted from numerical TDSE solutions. This can be rewritten

as

$$\begin{aligned}
\int_{T_0}^{T_1} \mathrm{d}t\, \vec{\mathcal{E}}(t)\dot{\vec{r}}(t) &= \int_{-\infty}^{\infty} \mathrm{d}t\, \vec{\mathcal{E}}(t)\dot{\vec{r}}(t) \\
&= \int_{-\infty}^{\infty} \mathrm{d}t\, \vec{\mathcal{E}}(t) \int_{-\infty}^{\infty} \mathrm{d}t'\, \dot{\vec{r}}(t')\, \frac{1}{2\pi} \int_{-\infty}^{\infty} \mathrm{d}\omega\, \mathrm{e}^{\pm \mathrm{i}\omega(t-t')} \\
&\quad \text{using } \delta(t-t') = \frac{1}{2\pi} \int_{-\infty}^{\infty} \mathrm{d}\omega\, \mathrm{e}^{\pm \mathrm{i}\omega(t-t')} \text{ (both signs work)} \\
&= \int_{-\infty}^{\infty} \mathrm{d}\omega\, \hat{\vec{\mathcal{E}}}(\pm\omega)\hat{\dot{\vec{r}}}(\mp\omega) \\
&= \int_{0}^{\infty} \mathrm{d}\omega\, \hat{\vec{\mathcal{E}}}(\pm\omega)\hat{\dot{\vec{r}}}^{*}(\pm\omega) - \int_{\infty}^{0} (-\mathrm{d}\omega)\, \hat{\vec{\mathcal{E}}}_X(\mp\omega)\hat{\dot{\vec{r}}}^{*}(\mp\omega) \\
&\quad \text{using } \hat{\dot{\vec{r}}}^{*}(\omega) = \hat{\dot{\vec{r}}}(-\omega) \text{because } \dot{\vec{r}} \text{is real} \\
&= \int_{0}^{\infty} \mathrm{d}\omega \left(\hat{\vec{\mathcal{E}}}(\pm\omega)\hat{\dot{\vec{r}}}^{*}(\pm\omega) + \hat{\vec{\mathcal{E}}}^{*}(\pm\omega)\hat{\dot{\vec{r}}}(\pm\omega) \right) \\
&= \int_{0}^{\infty} \mathrm{d}\omega\, 2\Re(\hat{\vec{\mathcal{E}}}(\pm\omega)\hat{\dot{\vec{r}}}^{*}(\pm\omega)) \qquad (8.4)
\end{aligned}$$

And second, postulate the following linear energy relation:

$$\delta E \stackrel{!}{=} \int_{0}^{\infty} \mathrm{d}\omega\, \omega \sigma_{\mathrm{TAS}}(\omega) J(\omega) \qquad (8.5)$$

i.e. the energy absorbed by the system is a sum over all laser frequencies ($\mathrm{d}\omega\, \omega$) times the efficiency at which the system absorbs at this frequency ($\sigma_{\mathrm{TAS}}(\omega)$) times the flux coming from the laser at this frequency ($J(\omega)$). The correctness of this relation is verified for perturbative XUV laser pulses $\dot{A}(t) = -\mathcal{E}(t)$ by comparing TAS with photo-electron spectra σ_{PES}, and finding excellent agreement:

$$\sigma_{\mathrm{PES}}(\omega) \propto \sigma_{\mathrm{TAS}}(\omega) J(\omega). \qquad (8.6)$$

In the presence of a non-perturbative IR however, no correspondence could be established. As stated in Ref. [170], the IR needs to be weak, such that it does not significantly contribute to ionization on its own. Additionally, for a cross section to be meaningful the XUV pulse must be short compared to the IR modulations, otherwise ionization from different cycles in the XUV pulse would see different IR field strengths and "average" over the instantaneous cross section. To which extend the linear relation holds, is unclear, but assuming equation (8.5) holds for the considered laser parameters, we may set equal:

$$\omega \sigma_{\mathrm{TAS}}(\omega) J(\omega) = 2\Re(\hat{\vec{\mathcal{E}}}(\pm\omega)\hat{\dot{\vec{r}}}^{*}(\pm\omega)) \qquad (8.7)$$

and obtain equation (8.1) after inserting the spectral flux $J(\omega) = \frac{|\tilde{\mathcal{E}}(\omega)|^2}{4\pi\alpha\omega}$ of the field.

8.2 Diagonalization of Fano Hamiltonian

In Sec. 5.2.1 we analyze properties of the Fano Hamiltonian (5.7)

$$H = H_0 + V = \underbrace{|\varphi\rangle E_\varphi \langle\varphi| + \int \mathrm{d}E\, |E\rangle E \langle E|}_{=:H_0,\text{ interaction-free eigenstates}} + \underbrace{\int \mathrm{d}E \left(|E\rangle V_E \langle\varphi| + |\varphi\rangle V_E^* \langle E| \right)}_{=:V,\text{ coupling}}. \tag{8.8}$$

Here we present a modern formulation of the diagonalization procedure presented in Ref. [39]. Using Møller operators $\Omega^{(\pm)} := \mathbb{1} + \big(E - H \pm \mathrm{i}\epsilon\big)^{-1} V$ we can express the eigenfunctions of the full Hamiltonian H in terms of the scattering solutions of the free Hamiltonian H_0 as

$$|E_\pm\rangle = \Omega^{(\pm)}(E)|E\rangle = \Big[\mathbb{1} + \big(E - H \pm \mathrm{i}\epsilon\big)^{-1} V\Big]|E\rangle. \tag{8.9}$$

Due to the low rank structure of V, these can be computed explicitly. First define

$$E - H \pm \mathrm{i}\epsilon = S_\pm - |v\rangle\langle\varphi| + |\varphi\rangle\langle v| = S_\pm - W\sigma_1 W^\dagger \tag{8.10}$$

with $S_\pm := E - H_0 \pm \mathrm{i}\epsilon$, $|v\rangle := \int \mathrm{d}E\, |E\rangle V_E$, $W := \big(|\varphi\rangle, |v\rangle\big)$ and $\sigma_1 = \begin{pmatrix} & 1 \\ 1 & \end{pmatrix}$. The inverse is then given by a variation of the Woodbury matrix identity:

$$\big(E - H \pm \mathrm{i}\epsilon\big)^{-1} = S_\pm^{-1} - S_\pm^{-1} W \big(W^\dagger S_\pm^{-1} W - \sigma_1^{-1}\big)^{-1} W^\dagger S_\pm^{-1} \tag{8.11}$$

where $S_\pm$ is diagonal and therefore its inverse trivial. Using

$$W^\dagger S_\pm^{-1} W - \sigma_1^{-1} = \begin{pmatrix} \langle\varphi|S_\pm^{-1}|\varphi\rangle & -1 \\ -1 & \langle v|S_\pm^{-1}|v\rangle \end{pmatrix} \tag{8.12}$$

$$\begin{aligned} \langle v|S_\pm^{-1}|v\rangle &= \int \mathrm{d}E' \mathrm{d}E''\, V_{E'}^* \langle E'| \Big(E - H_0 \pm \mathrm{i}\epsilon\Big)^{-1} |E''\rangle V_{E''} \\ &= \int \mathrm{d}E' \mathrm{d}E''\, V_{E'}^* \langle E'| \Big(\int \mathrm{d}\tilde{E}\, |\tilde{E}\rangle \frac{1}{E - \tilde{E} \pm \mathrm{i}\epsilon} \langle\tilde{E}| \Big) |E''\rangle V_{E''} \\ &= \int \mathrm{d}E'\, V_{E'}^* \frac{1}{E - E' \pm \mathrm{i}\epsilon} V_{E'} \end{aligned} \tag{8.13}$$

the inverse correction is given by

$$\big(W^\dagger S_\pm^{-1} W - \sigma_1^{-1}\big)^{-1} = \begin{pmatrix} Q_\varphi & -1 \\ -1 & Q_E \end{pmatrix}^{-1} = \frac{1}{Q_\varphi Q_E - 1} \begin{pmatrix} Q_E & 1 \\ 1 & Q_\varphi \end{pmatrix} \tag{8.14}$$

with $Q_\varphi := \frac{1}{E-E_\varphi \pm \mathrm{i}\epsilon}$ and $Q_E := \int \mathrm{d}E' \, \frac{|V_{E'}|^2}{E-E' \pm \mathrm{i}\epsilon}$. And therefore:

$$\begin{aligned}
\big(E - H \pm \mathrm{i}\epsilon\big)^{-1} \underbrace{V|E\rangle}_{=|\varphi\rangle V_E^*} &= S_\pm^{-1}|\varphi\rangle V_E^* - S_\pm^{-1} W \frac{1}{Q_\varphi Q_E - 1} \begin{pmatrix} Q_E & 1 \\ 1 & Q_\varphi \end{pmatrix} \underbrace{W^\dagger|\varphi\rangle}_{=(1,0)^{\mathrm{T}}} Q_\varphi V_E^* \\
&= |\varphi\rangle Q_\varphi V_E^* - S_\pm^{-1} \frac{1}{Q_\varphi Q_E - 1} \big(|\varphi\rangle Q_E + |v\rangle\big) Q_\varphi V_E^* \\
&= |\varphi\rangle Q_\varphi V_E^* - \frac{Q_\varphi V_E^*}{Q_\varphi Q_E - 1} \Big(Q_\varphi |\varphi\rangle Q_E + \int \mathrm{d}E' \, |E'\rangle \frac{1}{E - E' \pm \mathrm{i}\epsilon} V_{E'} \Big) \\
&= \frac{Q_\varphi V_E^*}{1 - Q_\varphi Q_E} \Big(|\varphi\rangle + \int \mathrm{d}E' \, |E'\rangle \frac{V_{E'}}{E - E' \pm \mathrm{i}\epsilon} \Big). \qquad (8.15)
\end{aligned}$$

Using the relation

$$\lim_{\epsilon \to 0} \int \mathrm{d}x \, \frac{f(x)}{x - x_0 \pm \mathrm{i}\epsilon} = \mathcal{P} \int \mathrm{d}x \, \frac{f(x)}{x - x_0} \mp \mathrm{i}\pi f(x_0), \qquad (8.16)$$

where $\mathcal{P} \int \mathrm{d}x \ldots$ denotes the Cauchy principal value of the integral, we obtain

$$\begin{aligned}
\lim_{\epsilon \to 0} Q_E &= \mathcal{P} \int \mathrm{d}E' \, \frac{|V_{E'}|^2}{E - E'} \mp \mathrm{i}\pi |V_E|^2 =: F_E \mp \mathrm{i}\pi |V_E|^2 \qquad (8.17) \\
\lim_{\epsilon \to 0} \int \mathrm{d}E' \, |E'\rangle \frac{V_{E'}}{E - E' \pm \mathrm{i}\epsilon} &= \mathcal{P} \int \mathrm{d}E' \, |E'\rangle \frac{V_{E'}}{E - E'} \mp \mathrm{i}\pi |E\rangle V_E \qquad (8.18)
\end{aligned}$$

and

$$|E_\pm\rangle = |E\rangle + \underbrace{\frac{1}{E - E_\varphi - F_E \pm \mathrm{i}\pi |V_E|^2}}_{= \frac{(E - E_\varphi - F_E) \mp \mathrm{i}\pi |V_E|^2}{(E - E_\varphi - F_E)^2 + \pi^2 |V_E|^4}} V_E^* \Big(|\varphi\rangle + \mathcal{P} \int \mathrm{d}E' \, |E'\rangle \frac{V_{E'}}{E - E'} \mp \mathrm{i}\pi |E\rangle V_E \Big). \qquad (8.19)$$

Defining Δ as the phase of the underbraced complex number and r as its magnitude

$$\begin{aligned}
\tan \Delta &:= -\frac{\pi |V_E|^2}{E - E_\varphi - F_E} \qquad (8.20) \\
r &:= \Big((E - E_\varphi - F_E)^2 + \pi^2 |V_E|^4 \Big)^{-\frac{1}{2}} \qquad (8.21)
\end{aligned}$$

we can rewrite

$$|E_\pm\rangle = |E\rangle \Big(1 \mp r \mathrm{e}^{\pm \mathrm{i}\Delta} |V_E|^2 \mathrm{i}\pi \Big) + r \mathrm{e}^{\pm \mathrm{i}\Delta} V_E^* \Big(\underbrace{|\varphi\rangle + \mathcal{P} \int \mathrm{d}E' \, |E'\rangle \frac{V_{E'}}{E - E'}}_{=:|\Phi\rangle} \Big). \qquad (8.22)$$

The superpositions

$$|\tilde{E}\rangle := \frac{1}{2\mathrm{i}\pi r |V_E|^2} \Big(|E_+\rangle - |E_-\rangle \Big) = \frac{\sin \Delta}{\pi V_E} |\Phi\rangle - \cos \Delta |E\rangle \qquad (8.23)$$

are the solutions given in the original Fano paper [39].

8.3 Atomic units

As the name indicates, atomic units are useful when describing atomic systems. Mass is measured in multiples of the electron rest mass $m_\mathrm{e} \approx 9.1{\cdot}10^{-31}\,\mathrm{kg}$, charge in multiples of the elementary charge $e \approx 1.6 \cdot 10^{-19}\,\mathrm{C}$, action in multiples of Planck's constant $\hbar \approx 10^{-34}\,\mathrm{J\,s}$, and the strength of electric interaction in multiples of $1/4\pi\epsilon_0 \approx 9 \cdot 10^9\,\mathrm{kg\,m^3\,s^{-2}\,C^{-2}}$. All other quantities, like length (measured in Bohr $a_0 = 4\pi\epsilon_0/m_\mathrm{e}e^2$), energy (measured in Hartree $E_\mathrm{h} = m_\mathrm{e}e^4/(4\pi\epsilon_0/\hbar)^2$), time (measured in units of $\hbar/E_\mathrm{h}$), velocity (in units of $a_0 E_\mathrm{h}/\hbar$), or electric field strength (in units of E_h/ea_0) are expressed in terms of these.

The common use of atomic units is to omit the true unit, i.e. instead of writing that the ground state energy of the Hydrogen atom is $E_0^{(\mathrm{Hy})} = -0.5\,E_\mathrm{h}$, one writes $E_0^{(\mathrm{Hy})} = -0.5\,\mathrm{a.u.}$ or even just $E_0^{(\mathrm{Hy})} = -0.5$. And instead of writing that the classical orbital radius in that ground state is $R_0^{(\mathrm{Hy})} = 1\,a_0$, one writes $R_0^{(\mathrm{Hy})} = 1\,\mathrm{a.u.}$ or just $R_0^{(\mathrm{Hy})} = 1$. This is nice for notational brevity but sometimes confusing. It is typically summarized by just stating $\hbar = e^2 = m_e = 4\pi\epsilon_0 \equiv 1$.

In the field of attosecond science units are sometimes mixed. Thereby energy is often also measured in Electronvolt $\mathrm{eV} \approx 27.2\,\mathrm{a.u.}\,(E_\mathrm{h})$. Laser pulse parameters are most often given in variations of SI units: wavelength in nanometers $\mathrm{nm} \approx 18.9\,\mathrm{a.u.}\,(a_0)$, duration in femtoseconds $\mathrm{fs} \approx 41.3\,\mathrm{a.u.}\,(\hbar/E_\mathrm{h})$, and intensity in $\mathrm{W/cm^2}$ for which there is no useful atomic unit expression. Instead, we can directly translate the intensity $I_{\mathrm{W/cm^2}}$ given in units of $\mathrm{W/cm^2}$ into electric field strength $F_{\mathrm{a.u.}}(I_{\mathrm{W/cm^2}})$ in atomic units as

$$F_{\mathrm{a.u.}}(I_{\mathrm{W/cm^2}}) = \underbrace{\sqrt{\frac{I_{\mathrm{W/cm^2}} \cdot 10^4}{\mathrm{c}\epsilon_0/2}}}_{F_\mathrm{SI}} \frac{ea_0}{E_\mathrm{h}}$$

with the field strength F_SI in SI units $(\frac{\mathrm{V}}{\mathrm{m}})$. Then, a typical laser intensity of $10^{14}\,\mathrm{W/cm^2}$ corresponds to an electric field strength in atomic units of $F_{\mathrm{a.u.}}(10^{14}\,\mathrm{W/cm^2}) \approx 0.05\,\mathrm{a.u.}\,(E_\mathrm{h}/ea_0)$.

8.4 Pulse shapes

As the spectral content of a propagating pulse should have no constant contribution (no direct current (DC) component), it is practical to define the laser pulse via its vector potential

$$\vec{A}(t) = -\int_{-\infty}^{t} \mathrm{d}\tau\, \mathcal{E}(\tau). \tag{8.24}$$

Then the constrain $0 \stackrel{!}{=} \hat{\mathcal{E}}(\omega = 0) = \int_{\mathbb{R}} \mathrm{d}\tau\, \mathcal{E}(\tau) \mathrm{e}^{\mathrm{i}\omega t}|_{\omega=0} = A(-\infty) - A(\infty)$ is automatically satisfied for pulse shapes with

$$A(-\infty) = 0 = A(\infty). \tag{8.25}$$

The most popular pulse shape for theoretical computations is

$$A(t) \propto C_n^{(m)}(t) \sin(\omega t) \tag{8.26}$$

with the pulse envelope

$$C_n^{(2)}(t) = \cos^2\left(\frac{\omega t}{2n}\right) \tag{8.27}$$

for $-\frac{n}{2}\tau \leq t \leq \frac{n}{2}\tau$ and 0 else. $\omega = \frac{2\pi}{\tau}$ is the carrier frequency and $n\tau$ is the total duration of the pulse. While this pulse is easy to work with analytically, and is also convenient for numerical computations as it does not have long tails, it does produce artifacts in some observables, see for example Fig. 6.3. A smoother pulse envelope is given by

$$C_n^{(8)}(t) = \cos^8\left(\frac{\omega t}{4n}\right) \tag{8.28}$$

for $-n\tau \leq t \leq n\tau$ and 0 else, which has the same full width at half maximum as above $C_n^{(2)}$, but a narrower spectral width. Pulses with exponential tails (for example envelopes employing Gaussians or hyperbolic secants) would be ideal, but such are not well suited for numeric time propagation as they offer no natural starting point for time propagation. $C_n^{(8)}$ approximates the Gaussian envelope well enough for all problems treated in this thesis.

Some observables require a constant intensity pulse with comparably short rampups and rampdowns. The pulse defined by

$$A(t) \propto f_{\frac{n}{2}\tau,(\frac{n}{2}+n_r)\tau}(-t) \sin(\omega t) f_{\frac{n}{2}\tau,(\frac{n}{2}+n_r)\tau}(t). \tag{8.29}$$

with $f_{a,b}$ as in Eq. (2.20) consists of n_r cycles rampup, n full cycles at maximum intensity, and n_r cycles rampdown.

Arbitrarily polarized pulses are simply built up by superposition. Here an example with $\hat{e}_3$ propagation direction ($\hat{e}_i \cdot \hat{e}_j = \delta_{ij}$):

$$\vec{A}(t) \propto \frac{1}{\sqrt{1+\epsilon^2}} \big(\hat{e}_1 \sin(\omega t) + \hat{e}_2 \epsilon \cos(\omega t)\big) C_n^{(m)}(t) \tag{8.30}$$

where $\epsilon \in [0, 1]$ defines the ellipticity. The parametrization with ϵ is chosen such that the cycle averaged intensity of the pulse is independent of ϵ.

8.5 tSurff expressions in spherical harmonics

8.5.1 Commutator expectation

The tSurff method requires evaluation of expectation values involving commutators with delta-like structure, specifically equations (2.16), (2.54) and (2.56).

For our specific representation using spherical harmonics, Eq. (3.3),

$$|\psi(\vec{r})\rangle = \sum_{lm} C_{lm}(t)|Y_l^m(\Omega_r)f_{lm}(r)\rangle \tag{8.31}$$

where $\Omega_r \equiv (\varphi_r, \eta_r)$ with $\eta = \cos\theta$, (the index r indicates that the angle Ω corresponds to the $\vec{r}$-vector, as opposed to the $\vec{k}$-vector which also appears now) we may compute explicitly:

$$\begin{aligned}
&\langle\chi_{\vec{k}}(t)|\Big[-\frac{\Delta}{2} - \mathrm{i}\vec{A}(t)\vec{\nabla}, \mathbb{1}_{r>R_c}\Big]|\psi(t)\rangle\sqrt{\frac{\pi}{2}}\mathrm{e}^{-\mathrm{i}\Phi(\vec{k},t)}\frac{1}{R_c^2}\\
=\;& \frac{1}{R_c^2}\sum_{l,m}(-\mathrm{i})^l Y_l^m(\Omega_k)\langle Y_l^m(\Omega_r)j_l(kr)|\Big[-\frac{\Delta}{2} - \mathrm{i}\vec{A}(t)\vec{\nabla}, \mathbb{1}_{r>R_c}\Big]\cdot\sum_{l',m'}C_{l',m'}(t)|Y_{l'}^{m'}(\Omega_r)f_{l',m'}(r)\rangle\\
=\;& \sum_{l,m,l',m'}(-\mathrm{i})^l Y_l^m(\Omega_k)\Bigg(\frac{1}{R_c^2}\langle Y_l^m|Y_{l'}^{m'}\rangle\int_0^\infty \mathrm{d}r\, r^2 j_l(kr)\frac{-1}{2}\Big(\frac{1}{r^2}\partial_r r^2\delta(r-R_c) + \delta(r-R_c)\partial_r\Big)f_{l',m'}(r)\\
&-\mathrm{i}A_x\langle Y_l^m|\sqrt{1-\eta^2}\cos\varphi|Y_{l'}^{m'}\rangle j_l(kR_c)f_{l',m'}(R_c) - \mathrm{i}A_z\langle Y_l^m|\eta|Y_{l'}^{m'}\rangle j_l(kR_c)f_{l',m'}(R_c)\Bigg)C_{l',m'}(t)\\
&\text{ignoring the } A_y \text{ term, i.e. assuming a laser pulse propagating in } \hat{y}-\text{direction}\\
=\;& \sum_{l,m}(-\mathrm{i})^l Y_l^m(\Omega_k)\Bigg(\frac{-1}{2}\Big(-\partial_r j_l(kr)\big|_{R_c}c_{l,m}(t) + j_l(kR_c)d_{l,m}\Big)\\
&-\mathrm{i}A_x j_l(kR_c)\langle Y_l^m|\sqrt{1-\eta^2}\cos\varphi\\
&\quad\times\Big(|Y_{l+1}^{m+1}\rangle c_{l+1,m+1}(t) + |Y_{l-1}^{m+1}\rangle c_{l-1,m+1}(t) + |Y_{l+1}^{m-1}\rangle c_{l+1,m-1}(t) + |Y_{l-1}^{m-1}\rangle c_{l-1,m-1}(t)\Big)\\
&-\mathrm{i}A_z j_l(kR_c)\langle Y_l^m|\eta\Big(|Y_{l+1}^m\rangle c_{l+1,m}(t) + |Y_{l-1}^m\rangle c_{l-1,m}(t)\Big)\Bigg)\\
&\text{introducing the surface values } c_{i,j}(t) := f_{i,j}(R_c)C_{i,j}(t) \text{ and } d_{i,j}(t) := \partial_r f_{i,j}(R_c)C_{i,j}(t)\\
=\;& \sum_l(-\mathrm{i})^l\partial_r j_l(kr)\big|_{R_c}\sum_m Y_l^m(\Omega_k)\frac{1}{2}c_{l,m}(t)\\
&-\sum_l(-\mathrm{i})^l j_l(kR_c)\sum_m Y_l^m(\Omega_k)\Big(\frac{d_{l,m}}{2} + \mathrm{i}A_x\big(\ldots+\ldots+\ldots+\ldots\big) + \mathrm{i}A_z\big(\ldots+\ldots\big)\Big)
\end{aligned} \tag{8.32}$$

We expanded the Volkov waves $\chi_{\vec{k}}(t)$ (Eq. (2.15)) in spherical harmonics and spherical Bessel functions according to Eq. (3.4).

8.5.2 Partial projection

The implied projection from a two particle wavefunction to a single particle wavefunction in Eq. (2.56) is simple with our discretization, as both single and two particle wavefunctions use the same bases. Defining

$$\xi_{lm}(\vec{r}) := Y_l^m(\Omega) f_{lm}(r) \tag{8.33}$$

we have

$$\Psi(\vec{r}_1, \vec{r}_2, t) = \sum_{l_1 l_2} \sum_{m_1 m_2} \xi_{l_1 m_1}(\vec{r}_1) \xi_{l_2 m_2}(\vec{r}_2) c_{l_1 l_2 m_1 m_2}(t) \tag{8.34}$$

and

$$J_{\vec{k}_1}(\vec{r}_2, t) = \sum_{l_2 m_2} \xi_{l_2 m_2}(\vec{r}_2) c_{l_2 m_2}(t) \tag{8.35}$$

with

$$c_{l_2 m_2}(t) = \sum_{l_1 m_1} \langle \chi_{\vec{k}_1}(\vec{r}_1, t) | \left[H_V(\vec{r}_1, t), \mathbb{1}_{r_1 > R_c} \right] | \xi_{l_1 m_1}(\vec{r}_1) \rangle c_{l_1 l_2 m_1 m_2}(t). \tag{8.36}$$

8.6 Finite element continuity and inverse overlap

Continuity across element boundaries for a wavefunction of the form

$$\psi(r,t) = \sum_{n=1}^{N} \sum_{k=1}^{p_n} f_k^{(n)}(r) c_k^{(n)}(t) \tag{8.37}$$

is assured by demanding $c_{p_{n-1}}^{(n-1)} = c_1^{(n)}$ for $n \geq 2$ [77]. The application of an operator matrix thus amounts to the blockwise application to each finite element and then enforcing continuity, which is done by averaging the corresponding coefficients

$$\left(c_{p_{n-1}}^{(n-1)}, c_1^{(n)}\right) \mapsto \left(\frac{c_{p_{n-1}}^{(n-1)} + c_1^{(n)}}{2}, \frac{c_{p_{n-1}}^{(n-1)} + c_1^{(n)}}{2}\right). \tag{8.38}$$

This map can be implemented by a projector $\widehat{Q}$ as follows. First identify the wavefunctions with the coefficient vector $\psi \leftrightarrow \vec{c} \in \mathbb{C}^d$, where $d = \sum_{n=1}^{N} p_n$ gives the overall number of coefficients. For

$$\vec{n} = (0, \ldots, 0, -\frac{1}{\sqrt{2}}, 0, \ldots, 0, \frac{1}{\sqrt{2}}, 0, \ldots, 0)^{\mathrm{T}} \in \mathbb{R}^d \tag{8.39}$$

the map $\widehat{\mathbb{1}} - \vec{n}\vec{n}^{\mathrm{T}}$ realizes the above averaging for the element boundary at r_n if the two non-zero coefficients in $\vec{n}$ are at the positions of $c_{p_{n-1}}^{(n-1)}$ and $c_1^{(n)}$ in the overall coefficient vector $\vec{c}$. The full projector is then given by $\widehat{Q} = \widehat{\mathbb{1}} - \sum_n \vec{n}\vec{n}^{\mathrm{T}}$, which can be written as

$$\widehat{Q} = \widehat{\mathbb{1}} - \widehat{R}\widehat{R}^{\mathrm{T}} \tag{8.40}$$

with

$$\widehat{R} = \left(\vec{2}, \ldots, \vec{n}, \ldots, \vec{N}\right) \in d \times (N-1). \tag{8.41}$$

The application of an inverse operator, as required by the time propagator for the overlap matrix, requires extra attention since we need the inverse including the projector $\widehat{Q}$, which in principle does not exist. It does however exist on the continuous subspace, which means that we need the inverse in the sense $(\widehat{Q}\widehat{S}\widehat{Q})^{-1}(\widehat{Q}\widehat{S}\widehat{Q}) = (\widehat{Q}\widehat{S}\widehat{Q})(\widehat{Q}\widehat{S}\widehat{Q})^{-1} = \widehat{Q}$, where $\widehat{S}\widehat{S}^{-1} = \widehat{\mathbb{1}}$ is the blockwise inverse. The formula used is a variation of the Woodbury matrix identity. It takes the form

$$(\widehat{Q}\widehat{S}\widehat{Q})^{-1} = \left(\widehat{\mathbb{1}} - \widehat{S}^{-1}\widehat{R}\left(\widehat{R}^{\mathrm{T}}\widehat{S}^{-1}\widehat{R}\right)^{-1}\widehat{R}^{\mathrm{T}}\right)\widehat{S}^{-1}\widehat{Q}. \tag{8.42}$$

This reduces the application of the full inverse $(\widehat{Q}\widehat{S}\widehat{Q})^{-1} \in d \times d$ (with operations count $\propto N^2p^2$) to the application of the blockwise inverse $\widehat{S}^{-1}$ (operations count $\propto Np$ due to the near diagonal form of $\widehat{S}$) and a correction $\left(\widehat{R}^{\mathrm{T}}\widehat{S}^{-1}\widehat{R}\right)^{-1} \in (N-1) \times (N-1)$ on a small subspace.

Bibliography

[1] C. Hofmann, et al. Interpreting electron-momentum distributions and nonadiabaticity in strong-field ionization. *Phys. Rev. A*, 90(4):043406–, October 2014.

[2] L. Torlina, et al. Interpreting attoclock measurements of tunnelling times. *Nat Phys*, 11(6):503–508, June 2015.

[3] V. P. Majety, A. Zielinski, and A. Scrinzi. Mixed gauge in strong laser-matter interaction. *Journal of Physics B: Atomic, Molecular and Optical Physics*, 48(2):025601–, 2015.

[4] V. P. Majety, A. Zielinski, and A. Scrinzi. Photoionization of few electron systems: a hybrid coupled channels approach. *New Journal of Physics*, 17(6):063002–, 2015.

[5] A. Zielinski, et al. Anomalous Fano Profiles in External Fields. *Phys. Rev. Lett.*, 115:243001–, 2015.

[6] A. Zielinski, V. P. Majety, and A. Scrinzi. Double ionization spectra of Helium at infrared wavelength. *arXiv:1511.06655*, (accepted for publication in Phys. Rev. A) 2016.

[7] A. H. Zewail. Femtochemistry: Atomic-Scale Dynamics of the Chemical Bond. *J. Phys. Chem. A*, 104(24):5660–5694, June 2000.

[8] F. Krausz and M. Ivanov. Attosecond physics. *Rev. Mod. Phys.*, 81(1):163–234, February 2009.

[9] E. Goulielmakis, et al. Attosecond Control and Measurement: Lightwave Electronics. *Science*, 317(5839):769–775, August 2007.

[10] E. Goulielmakis, et al. Direct Measurement of Light Waves. *Science*, 305(5688):1267–1269, August 2004.

[11] M. Y. Shverdin, et al. Generation of a Single-Cycle Optical Pulse. *Phys. Rev. Lett.*, 94(3):033904–, January 2005.

[12] T. Fuji, et al. Parametric amplification of few-cycle carrier-envelope phase-stable pulses at 2.1 μm. *Opt. Lett.*, 31(8):1103–1105, 2006.

[13] M. Drescher, et al. Time-resolved atomic inner-shell spectroscopy. *Nature*, 419(6909):803–807, October 2002.

[14] D. Shafir, et al. Resolving the time when an electron exits a tunnelling barrier. *Nature*, 485(7398):343–346, May 2012.

[15] M. Meckel, et al. Laser-Induced Electron Tunneling and Diffraction. *Science*, 320(5882):1478–1482, June 2008.

[16] E. Goulielmakis, et al. Real-time observation of valence electron motion. *Nature*, 466(7307):739–743, August 2010.

[17] P. Eckle, et al. Attosecond Ionization and Tunneling Delay Time Measurements in Helium. *Science*, 322(5907):1525–1529, December 2008.

[18] R. Cireasa, et al. Probing molecular chirality on a sub-femtosecond timescale. *Nat Phys*, 11(8):654–658, August 2015.

[19] C. I. Blaga, et al. Imaging ultrafast molecular dynamics with laser-induced electron diffraction. *Nature*, 483(7388):194–197, March 2012.

[20] C. Ott, et al. Reconstruction and control of a time-dependent two-electron wave packet. *Nature*, 516(7531):374–378, December 2014.

[21] F. Calegari, et al. Ultrafast electron dynamics in phenylalanine initiated by attosecond pulses. *Science*, 346(6207):336–339, October 2014.

[22] A. N. Pfeiffer, et al. Timing the release in sequential double ionization. *Nat. Phys.*, 7(5):428–433, May 2011.

[23] R. Boge, et al. Probing Nonadiabatic Effects in Strong-Field Tunnel Ionization. *Phys. Rev. Lett.*, 111(10):103003–, September 2013.

[24] M. Spanner, et al. Reading diffraction images in strong field ionization of diatomic molecules. *Journal of Physics B*, 37:243–250, 2004.

[25] M. Lein, et al. Interference effects in high-order harmonic generation with molecules. *Phys. Rev. A*, 66(2):023805–, August 2002.

[26] V. P. Majety and A. Scrinzi. Dynamic exchange in the strong field ionization of molecules. *Phys. Rev. Lett.*, 2015.

[27] J. Feist, et al. Nonsequential two-photon double ionization of Helium. *Phys. Rev. A*, 77(4):043420–, April 2008.

[28] J. S. Parker, et al. Time delay between singly and doubly ionizing wavepackets in laser-driven Helium. *Journal of Physics B: Atomic, Molecular and Optical Physics*, 36(21):L393–, 2003.

[29] J. S. Parker, et al. High-Energy Cutoff in the Spectrum of Strong-Field Nonsequential Double Ionization. *Phys. Rev. Lett.*, 96(13):133001–, April 2006.

[30] A. Emmanouilidou, et al. Direct versus delayed pathways in strong-field non-sequential double ionization. *New Journal of Physics*, 13(4):043001, 2011.

[31] S. X. Hu. Boosting Photoabsorption by Attosecond Control of Electron Correlation. *Phys. Rev. Lett.*, 111(12):123003–, September 2013.

[32] L. Tao and A. Scrinzi. Photo-electron momentum spectra from minimal volumes: the time-dependent surface flux method. *New Journal of Physics*, 14(1):013021–, 2012.

[33] A. Scrinzi. t-SURFF: fully differential two-electron photo-emission spectra. *New Journal of Physics*, 14(8):085008, 2012.

[34] A. N. Pfeiffer, et al. Attoclock reveals natural coordinates of the laser-induced tunnelling current flow in atoms. *Nat. Phys.*, 8(1):76–80, January 2012.

[35] A. S. Landsman, et al. Ultrafast resolution of tunneling delay time. *Optica*, 1(5):343–349, 2014.

[36] M.V. Ammosov, N.B. Delone, and V.P. Krainov. Tunnel ionization of complex atoms and of atomic ions in an alternating electronmagnetic field. *Zh. Eksp. Teor. Fiz.*, 91:2008, 1986.

[37] N. B. Delone and V. P. Krainov. Energy and angular electron spectra for the tunnel ionization of atoms by strong low-frequency radiation. *J. Opt. Soc. Am. B*, 8(6):1207–1211, 1991.

[38] A. N. Pfeiffer, et al. Probing the Longitudinal Momentum Spread of the Electron Wave Packet at the Tunnel Exit. *Phys. Rev. Lett.*, 109:083002, Aug 2012.

[39] U. Fano. Effects of Configuration Interaction on Intensities and Phase Shifts. *Phys. Rev.*, 124(6):1866–1878, December 1961.

[40] A. E. Miroshnichenko, S. Flach, and Y. S. Kivshar. Fano resonances in nanoscale structures. *Rev. Mod. Phys.*, 82(3):2257–2298, August 2010.

[41] K. Kobayashi, et al. Mesoscopic Fano effect in a quantum dot embedded in an Aharonov-Bohm ring. *Phys. Rev. B*, 68(23):235304–, December 2003.

[42] G. S. Agarwal, S. L. Haan, and J. Cooper. Radiative decay of autoionizing states in laser fields. I. General theory. *Phys. Rev. A*, 29(5):2552–2564, May 1984.

[43] M. Wickenhauser, et al. Time Resolved Fano Resonances. *Phys. Rev. Lett.*, 94(2):023002–, January 2005.

[44] A. A. Clerk, X. Waintal, and P. W. Brouwer. Fano Resonances as a Probe of Phase Coherence in Quantum Dots. *Phys. Rev. Lett.*, 86(20):4636–4639, May 2001.

[45] A. Bärnthaler, et al. Probing Decoherence through Fano Resonances. *Phys. Rev. Lett.*, 105(5):056801–, July 2010.

[46] O. Schwarzkopf, et al. Energy- and angle-resolved double photoionization in Helium. *Phys. Rev. Lett.*, 70(20):3008–3011, May 1993.

[47] B. Walker, et al. Precision Measurement of Strong Field Double Ionization of Helium. *Phys. Rev. Lett.*, 73(9):1227–1230, August 1994.

[48] P. B. Corkum. Plasma perspective on strong field multiphoton ionization. *Phys. Rev. Lett.*, 71(13):1994–1997, September 1993.

[49] V. L. B. de Jesus, et al. Atomic structure dependence of nonsequential double ionization of He, Ne and Ar in strong laser pulses. *Journal of Physics B: Atomic, Molecular and Optical Physics*, 37(8):L161–, 2004.

[50] S. L. Haan, et al. Variable Time Lag and Backward Ejection in Full-Dimensional Analysis of Strong-Field Double Ionization. *Phys. Rev. Lett.*, 97(10):103008–, September 2006.

[51] T. Shaaran, M. T. Nygren, and C. Figueira de Morisson Faria. Laser-induced nonsequential double ionization at and above the recollision-excitation-tunneling threshold. *Phys. Rev. A*, 81(6):063413–, June 2010.

[52] A. Emmanouilidou. Prevalence of different double ionization pathways and traces of three-body interactions in strongly driven Helium. *Phys. Rev. A*, 83(2):023403–, February 2011.

[53] R. Nepstad, T. Birkeland, and M. Førre. Numerical study of two-photon ionization of helium using an *ab initio* numerical framework. *Phys. Rev. A*, 81(6):063402–, June 2010.

[54] L. V. Keldysh. Ionization in the field of a strong electromagnetic wave. *Sov. Phys. JETP (engl. transl.)*, 20:1307, 1965.

[55] M. Y. Ivanov, M. Spanner, and O. Smirnova. Anatomy of strong field ionization. *Journal of Modern Optics*, 52(2-3):165–184, January 2005.

[56] M. Lewenstein, et al. Theory of high-harmonic generation by low-frequency laser fields. *Phys. Rev. A*, 49(3):2117–2132, March 1994.

[57] K. Midorikawa. Ultrafast dynamic imaging. *Nat Photon*, 5(11):640–641, November 2011.

[58] Z. Chen, Y. Liang, and C. D. Lin. Quantum Theory of Recollisional (e, $2e$) Process in Strong Field Nonsequential Double Ionization of Helium. *Phys. Rev. Lett.*, 104(25):253201–, June 2010.

[59] T. Ishikawa, X. M. Tong, and N. Toshima. Double ionization of He in an intense laser field via a rescattering process. *Phys. Rev. A*, 82(3):033411–, September 2010.

[60] S. Chen, C. Ruiz, and A. Becker. Double ionization of Helium by intense near-infrared and VUV laser pulses. *Phys. Rev. A*, 82(3):033426–, September 2010.

[61] F. Mauger, C. Chandre, and T. Uzer. From Recollisions to the Knee: A Road Map for Double Ionization in Intense Laser Fields. *Phys. Rev. Lett.*, 104(4):043005–, January 2010.

[62] L. Yue and Madsen L. B. Dissociative ionization of $H_2{}^+$ using intense femtosecond XUV laser pulses. *Phys. Rev. A*, 90(6):063408–, December 2014.

[63] A. Karamatskou, et al. Calculation of photoelectron spectra within the time-dependent configuration-interaction singles scheme. *Phys. Rev. A*, 89:033415, Mar 2014.

[64] O. Smirnova, M. Spanner, and M. Ivanov. Analytical solutions for strong field-driven atomic and molecular one- and two-electron continua and applications to strong-field problems. *Phys. Rev. A*, 77(3):033407–, March 2008.

[65] L. Argenti, et al. Photoionization of helium by attosecond pulses: Extraction of spectra from correlated wave functions. *Phys. Rev. A*, 87(5):053405–, May 2013.

[66] L. Malegat, et al. Analysing a two-electron wavepacket by semiclassically propagating its Fourier components in space. *Journal of Physics B: Atomic, Molecular and Optical Physics*, 43(24):245601–, 2010.

[67] M. S. Pindzola, et al. The time-dependent close-coupling method for atomic and molecular collision processes. *Journal of Physics B: Atomic, Molecular and Optical Physics*, 40(7):R39–, 2007.

[68] C. W. McCurdy, M. Baertschy, and T. N. Rescigno. Solving the three-body Coulomb breakup problem using exterior complex scaling. *Journal of Physics B: Atomic, Molecular and Optical Physics*, 37(17):R137–, 2004.

[69] T. Schneider, P. L. Chocian, and J.-M. Rost. Separation and Identification of Dominant Mechanisms in Double Photoionization. *Phys. Rev. Lett.*, 89:073002, Jul 2002.

[70] R. Pazourek, et al. Universal features in sequential and nonsequential two-photon double ionization of Helium. *Phys. Rev. A*, 83(5):053418–, May 2011.

[71] Z. Zhang, et al. Two-photon double ionization of Helium: Evolution of the joint angular distribution with photon energy and two-electron energy sharing. *Phys. Rev. A*, 84(4):043409–, October 2011.

[72] W. Jiang, et al. Comparison study of electron correlation in one-photon and two-photon double ionization of Helium. *Phys. Rev. A*, 88(2):023410–, August 2013.

[73] A. Liu and U. Thumm. Laser-assisted XUV few-photon double ionization of Helium: Joint angular distributions. *Phys. Rev. A*, 89(6):063423–, June 2014.

[74] A. Palacios, et al. Two-photon double ionization of the Helium atom by ultrashort pulses. *Journal of Physics B: Atomic, Molecular and Optical Physics*, 43(19):194003, 2010.

[75] J. Feist, et al. Probing Electron Correlation via Attosecond xuv Pulses in the Two-Photon Double Ionization of Helium. *Phys. Rev. Lett.*, 103(6):063002, August 2009.

[76] S. Brenner and R. Scott. *The Mathematical Theory of Finite Element Methods*. Springer, 2007.

[77] A. Scrinzi. Infinite-range exterior complex scaling as a perfect absorber in time-dependent problems. *Phys. Rev. A*, 81(5):053845, May 2010.

[78] A. Scrinzi and N. Elander. A finite element implementation of exterior complex scaling for the accurate determination of resonance energies. *The Journal of Chemical Physics*, 98(5):3866–3875, 1993.

[79] L. Tao, C. W. McCurdy, and T. N. Rescigno. Grid-based methods for diatomic quantum scattering problems: A finite-element discrete-variable representation in prolate spheroidal coordinates. *Phys. Rev. A*, 79(1):012719–, January 2009.

[80] M. Weinmüller, et al. Perfect absorption in Schrödinger-like problems using non-equidistant complex grids. *arXiv:1509.04947*, 2015.

[81] E. Cormier and P. Lambropoulos. Optimal gauge and gauge invariance in non-perturbative time-dependent calculation of above-threshold ionization. *Journal of Physics B: Atomic, Molecular and Optical Physics*, 29(9):1667–, 1996.

[82] F. He, C. Ruiz, and A. Becker. Absorbing boundaries in numerical solutions of the time-dependent Schrödinger equation on a grid using exterior complex scaling. *Phys. Rev. A*, 75(5):053407–, May 2007.

[83] tRecX code: http://homepages.physik.uni-muenchen.de/~armin.scrinzi/tRecX/home.html.

[84] Eigen library: http://eigen.tuxfamily.org/.

[85] Arpack library: http://www.caam.rice.edu/software/ARPACK/.

[86] Y. Saad, et al. Solution of large eigenvalue problems in electronic structure calculations. 36(3):563–578–, 1996.

[87] Alglib library: http://www.alglib.net/.

[88] MPI library: http://www.open-mpi.org/.

[89] Boost library: http://www.boost.org/.

[90] E. Gamma, et al. *Design Patterns: Elements of Reusable Object-Oriented Software*. Addison-Wesley, 1994.

[91] E. S. Smyth, J. S. Parker, and K. T. Taylor. Numerical integration of the time-dependent Schrödinger equation for laser-driven Helium. *Computer Physics Communications*, 114:1–14, November 1998.

[92] L.A. Collins, J.D. Kress, and R.B. Walker. Excitation and ionization of molecules by a single-mode laser field using a time-dependent approach. *Computer Physics Communications*, 114(13):15–26, November 1998.

[93] W. Joppich and S. Mijalkovic. *Multigrid Methods for Process Simulation*. Springer-Verlag Wien, 1993.

[94] N. Moiseyev. Quantum theory of resonances: calculating energies, widths and cross-sections by complex scaling. *Physics Reports*, 302:212–293, 1998.

[95] W. P. Reinhardt. Complex Coordinates in the Theory of Atomic and Molecular Structure and Dynamics. *Annual Reviews: Physical Chemistry*, 33:223–255, 1982.

[96] J. Breidbach and L. S. Cederbaum. Universal Attosecond Response to the Removal of an Electron. *Phys. Rev. Lett.*, 94(3):033901–, January 2005.

[97] S. Sukiasyan, K. L. Ishikawa, and M. Ivanov. Attosecond cascades and time delays in one-electron photoionization. *Phys. Rev. A*, 86(3):033423–, September 2012.

[98] A. S. Kheifets and I. A. Ivanov. Delay in Atomic Photoionization. *Phys. Rev. Lett.*, 105(23):233002–, December 2010.

[99] L. R. Moore, et al. Time delay between photoemission from the $2p$ and $2s$ subshells of Neon. *Phys. Rev. A*, 84(6):061404–, December 2011.

[100] K. Klünder, et al. Probing Single-Photon Ionization on the Attosecond Time Scale. *Phys. Rev. Lett.*, 106(14):143002–, April 2011.

[101] M. Ivanov and O. Smirnova. How Accurate Is the Attosecond Streak Camera? *Phys. Rev. Lett.*, 107(21):213605–, November 2011.

[102] J. M. Dahlström, A. L'Huillier, and A. Maquet. Introduction to attosecond delays in photoionization. *Journal of Physics B: Atomic, Molecular and Optical Physics*, 45(18):183001–, 2012.

[103] R. Pazourek, S. Nagele, and J. Burgdörfer. Time-resolved photoemission on the attosecond scale: Opportunities and challenges. *Faraday Discuss*, 163:353376, 2013.

[104] P. Eckle, et al. Attosecond angular streaking. *Nat Phys*, 4(7):565–570, July 2008.

[105] A. N. Pfeiffer, et al. Breakdown of the independent electron approximation in sequential double ionization. *New Journal of Physics*, 13(9):093008–, 2011.

[106] H. Muller. An efficient propagation scheme for the time-dependent Schrödinger equation in the velocity gauge. *Laser Phys*, 9:138148, 1999.

[107] I. A. Ivanov and A. S. Kheifets. Strong-field ionization of He by elliptically polarized light in attoclock configuration. *Phys. Rev. A*, 89(2):021402–, February 2014.

[108] L. Torlina and O. Smirnova. Time-dependent analytical R-matrix approach for strong-field dynamics. I. One-electron systems. *Phys. Rev. A*, 86:043408, Oct 2012.

[109] L. Torlina, J. Kaushal, and O. Smirnova. Time-resolving electron-core dynamics during strong-field ionization in circularly polarized fields. *Phys. Rev. A*, 88:053403, Nov 2013.

[110] T. Nubbemeyer, et al. Strong-Field Tunneling without Ionization. *Phys. Rev. Lett.*, 101(23):233001–, December 2008.

[111] National Institute of Standards and Technology Database: http://physics.nist.gov/PhysRefData/ASD/levels_form.html.

[112] A. Scrinzi. Accurate bound-state energies of Helium in a strong magnetic field. *Phys. Rev. A*, 58(5):3879–3883, November 1998.

[113] V. D. Mur, S. V. Popruzhenko, and V. S. Popov. Energy and momentum spectra of photoelectrons under conditions of ionization by strong laser radiation (The case of elliptic polarization). *Sov. Phys. JETP*, 92(5):777–788–, 2001.

[114] C. Hofmann, et al. Comparison of different approaches to the longitudinal momentum spread after tunnel ionization. *Journal of Physics B: Atomic, Molecular and Optical Physics*, 46(12):125601–, 2013.

[115] R. Dörner, et al. Cold Target Recoil Ion Momentum Spectroscopy: a momentum microscope to view atomic collision dynamics. *Physics Reports*, 330(23):95–192, June 2000.

[116] H. R. Reiss. Effect of an intense electromagnetic field on a weakly bound system. *Phys. Rev. A*, 22:1786–1813, Nov 1980.

[117] A. M. Perelomov, V. S. Popov, and M. V. Terentev. Ionization of atoms in an alternating electric field. *Sov. Phys. JETP*, 24:207, 1967.

[118] A. S. Alnaser, et al. Laser-peak-intensity calibration using recoil-ion momentum imaging. *Phys. Rev. A*, 70:023413, Aug 2004.

[119] L. Arissian, et al. Direct Test of Laser Tunneling with Electron Momentum Imaging. *Phys. Rev. Lett.*, 105(13):133002–, September 2010.

[120] A. L'Huillier, et al. Multiply charged ions induced by multiphoton absorption processes in rare-gas atoms at 1.064μm. *Journal of Physics B: Atomic and Molecular Physics*, 16(8):1363–, 1983.

[121] C. Hofmann, et al. Non-adiabatic imprints on the electron wave packet in strong field ionization with circular polarization. *submitted to New Journal of Physics: NJP-104102*, 2015.

[122] S. Pabst and R. Santra. Strong-Field Many-Body Physics and the Giant Enhancement in the High-Harmonic Spectrum of Xenon. *Phys. Rev. Lett.*, 111(23):233005–, December 2013.

[123] M. Spanner and S. Patchkovskii. One-electron ionization of multielectron systems in strong nonresonant laser fields. *Phys. Rev. A*, 80(6):063411–, December 2009.

[124] J. Jose, R. R. Lucchese, and T. N. Rescigno. Interchannel coupling effects in the valence photoionization of SF_6. *The Journal of Chemical Physics*, 140(20):–, 2014.

[125] J. M. N. Djiokap and A. F. Starace. Resonant enhancement of the harmonic-generation spectrum of Beryllium. *Phys. Rev. A*, 88(5):053412–, November 2013.

[126] A. Palacios, H. Bachau, and F. Martin. Enhancement and Control of H_2 Dissociative Ionization by Femtosecond VUV Laser Pulses. *Phys. Rev. Lett.*, 96(14):143001–, April 2006.

[127] H. Timmers, et al. Coherent Electron Hole Dynamics Near a Conical Intersection. *Phys. Rev. Lett.*, 113(11):113003–, September 2014.

[128] L. Greenman, et al. Implementation of the time-dependent configuration-interaction singles method for atomic strong-field processes. *Phys. Rev. A*, 82(2):023406–, August 2010.

[129] D. Hochstuhl and M. Bonitz. Time-dependent restricted-active-space configuration-interaction method for the photoionization of many-electron atoms. *Phys. Rev. A*, 86(5):053424–, November 2012.

[130] M. A. Lysaght, H. W. van der Hart, and P. G. Burke. Time-dependent R-matrix theory for ultrafast atomic processes. *Phys. Rev. A*, 79(5):053411–, May 2009.

[131] I. Shavitt. The Method of Configuration Interaction. In III Schaefer, HenryF., editor, *Modern Theoretical Chemistry*, volume 3, pages 189–275–. Springer US, 1977.

[132] H. Lischka, et al. Columbus: program system for advanced multireference theory calculations. *WIREs Comput Mol Sci*, 1(2):191–199, March 2011.

[133] J. M. N. Djiokap, et al. Enhanced asymmetry in few-cycle attosecond pulse ionization of He in the vicinity of autoionizing resonances. *New Journal of Physics*, 14(9):095010–, 2012.

[134] T. Morishita and C. D. Lin. Photoelectron spectra and high Rydberg states of lithium generated by intense lasers in the over-the-barrier ionization regime. *Phys. Rev. A*, 87(6):063405–, June 2013.

[135] Y. V. Vanne and A. Saenz. Numerical treatment of diatomic two-electron molecules using a B-spline based CI method. *Journal of Physics B: Atomic, Molecular and Optical Physics*, 37(20):4101–, 2004.

[136] J. Förster, Y. V. Vanne, and A. Saenz. Ionization behavior of molecular Hydrogen in intense laser fields: Influence of molecular vibration and alignment. *Phys. Rev. A*, 90(5):053424–, November 2014.

[137] H.-W. Lee. Generic Transmission Zeros and In-Phase Resonances in Time-Reversal Symmetric Single Channel Transport. *Phys. Rev. Lett.*, 82(11):2358–2361, March 1999.

[138] C. Ott, et al. Lorentz Meets Fano in Spectral Line Shapes: A Universal Phase and Its Laser Control. *Science*, 340(6133):716–720, May 2013.

[139] F. Mauger, C. Chandre, and T. Uzer. Recollisions and Correlated Double Ionization with Circularly Polarized Light. *Phys. Rev. Lett.*, 105(8):083002–, August 2010.

[140] W. Becker and H. Rottke. Many-electron strong-field physics. *Contemporary Physics*, 49(3):199–223, May 2008.

[141] L. Nikolopoulos and P. Lambropoulos. Time-dependent theory of double ionization of Helium under XUV radiation. *Journal of Physics B: Atomic, Molecular and Optical Physics*, 40(7):1347–, 2007.

[142] J. Ullrich, et al. Recoil-ion and electron momentum spectroscopy: reaction-microscopes. *Reports on Progress in Physics*, 66(9):1463–, 2003.

[143] L. Avaldi and A. Huetz. Photodouble ionization and the dynamics of electron pairs in the continuum. *Journal of Physics B: Atomic, Molecular and Optical Physics*, 38(9):S861–, 2005.

[144] A. Staudte, et al. Binary and Recoil Collisions in Strong Field Double Ionization of Helium. *Phys. Rev. Lett.*, 99(26):263002–, December 2007.

[145] A. Rudenko, et al. Correlated Two-Electron Momentum Spectra for Strong-Field Nonsequential Double Ionization of He at 800 nm. *Phys. Rev. Lett.*, 99(26):263003–, December 2007.

[146] A. Rudenko, et al. Recoil-Ion Momentum Distributions for Two-Photon Double Ionization of He and Ne by 44eV Free-Electron Laser Radiation. *Phys. Rev. Lett.*, 101(7):073003–, August 2008.

[147] A. Fleischer, et al. Probing Angular Correlations in Sequential Double Ionization. *Phys. Rev. Lett.*, 107(11):113003–, September 2011.

[148] M. A. Stevenson and B. Lohmann. Fully differential cross-section measurements for electron-impact ionization of argon over the complete in-plane angular range. *Phys. Rev. A*, 77(3):032708–, March 2008.

[149] B. Bergues, et al. Attosecond tracing of correlated electron-emission in non-sequential double ionization. *Nat Commun*, 3:813–, May 2012.

[150] K. Henrichs, et al. Observation of Electron Energy Discretization in Strong Field Double Ionization. *Phys. Rev. Lett.*, 111(11):113003–, September 2013.

[151] Y. Liu, et al. Strong-Field Double Ionization through Sequential Release from Double Excitation with Subsequent Coulomb Scattering. *Phys. Rev. Lett.*, 112(1):013003–, January 2014.

[152] D. A. Horner, et al. Two-photon double ionization of Helium above and below the threshold for sequential ionization. *Phys. Rev. A*, 76(3):030701–, September 2007.

[153] L. Feng and H. W. van der Hart. Two-photon double ionization of He. *Journal of Physics B: Atomic, Molecular and Optical Physics*, 36(1):L1, 2003.

[154] P. G. Burke, P. Francken, and C. J. Joachain. *R*-matrix-Floquet theory of multiphoton processes. *Journal of Physics B: Atomic, Molecular and Optical Physics*, 24(4):761–, 1991.

[155] B. I. Schneider, L. A. Collins, and S. X. Hu. Parallel solver for the time-dependent linear and nonlinear Schrödinger equation. *Phys. Rev. E*, 73(3):036708–, March 2006.

[156] R. Grobe, K. Rzazewski, and J. H. Eberly. Measure of electron-electron correlation in atomic physics. *Journal of Physics B: Atomic, Molecular and Optical Physics*, 27(16):L503–, 1994.

[157] J. A. R. Samson, et al. Double photoionization of Helium. *Phys. Rev. A*, 57(3):1906–1911, March 1998.

[158] D. Hochstuhl, C. M. Hinz, and M. Bonitz. Time-dependent multiconfiguration methods for the numerical simulation of photoionization processes of many-electron atoms. *Springer*, 223(2):177–336–, 2014.

[159] L. Malegat, et al. A novel estimate of the two-photon double-ionization cross section of Helium. *Journal of Physics B: Atomic, Molecular and Optical Physics*, 45(17):175601–, 2012.

[160] I. A. Ivanov and A. S. Kheifets. Two-photon double ionization of Helium in the region of photon energies 42-50 eV. *Phys. Rev. A*, 75(3):033411–, March 2007.

[161] E. Foumouo, et al. Theory of multiphoton single and double ionization of two-electron atomic systems driven by short-wavelength electric fields: An *ab initio* treatment. *Phys. Rev. A*, 74(6):063409, December 2006.

[162] S. X. Hu, J. Colgan, and L. A. Collins. Triple-differential cross-sections for two-photon double ionization of He near threshold. *Journal of Physics B: Atomic, Molecular and Optical Physics*, 38(1):L35, 2005.

[163] B. Piraux, et al. Probing electron-electron correlation with attosecond pulses. *The European Physical Journal D - Atomic, Molecular, Optical and Plasma Physics*, 26(1):7–13, 2003.

[164] S. Laulan and H. Bachau. Correlation effects in two-photon single and double ionization of Helium. *Phys. Rev. A*, 68(1):013409, July 2003.

[165] J. S. Parker, et al. Double-electron above threshold ionization of helium. *Journal of Physics B: Atomic, Molecular and Optical Physics*, 34(3):L69–, 2001.

[166] F. Maulbetsch and J. S. Briggs. Selection rules for transitions to two-electron continuum states. *Journal of Physics B: Atomic, Molecular and Optical Physics*, 28(4):551–, 1995.

[167] M. Lein, E. K. U. Gross, and V. Engel. Discrete peaks in above-threshold double-ionization spectra. *Phys. Rev. A*, 64(2):023406–, July 2001.

[168] Q. Liao and P. Lu. Energy correlation in above-threshold nonsequential double ionization at 800 nm. *Phys. Rev. A*, 82(2):021403–, August 2010.

[169] T. Lee, M. S. Pindzola, and F. Robicheaux. Energy and angular differential probabilities for photoionization of He using chirped attosecond soft-x-ray pulses. *Phys. Rev. A*, 79(5):053420–, May 2009.

[170] M. B. Gaarde, et al. Transient absorption and reshaping of ultrafast XUV light by laser-dressed Helium. *Phys. Rev. A*, 83(1):013419, January 2011.

Acknowledgments

I would like to thank my supervisor Prof. Dr. Armin Scrinzi for his ingenious inputs and his readiness to provide help, even in details. Also thanks to (now Dr.) Vinay Majety for many fruitful discussions. And of course kisses to my wife Sophia.

Declaration

I hereby declare that this thesis is my own work, and that I have not used any sources and aids other than those stated in the thesis.

Munich, December 8, 2015

_____

Alejandro Zielinski